PHENOMENOLOGICAL MODELING OF THE MUTUAL IMPEDANCE AMONG WIRE ANTENNAS

GERALD PACABA ARADA

Ph.D

The Hong Kong Polytechnic University

2018

The Hong Kong Polytechnic University

Department of Electronic & Information Engineering

Phenomenological Modeling of the Mutual Impedance Among Wire Antennas

Gerald Pacaba ARADA

A thesis submitted in partial fulfillment of the requirements

for the degree of Doctor of Philosophy

August 2017

CERTIFICATE OF ORIGINALITY

I hereby declare that this thesis is my own work and that, to the best of my knowledge and belief, it reproduces no material previously published or written, nor material that has been accepted for the award of any other degree or diploma, except where due acknowledgment has been made in the text.

Gerald Pacaba ARADA

Abstract

This dissertation pioneers the "phenomenological" or "behavioral" approach to model the mutual-impedance matrix between two skewed crossed dipoles. This 2×2 mutual impedance matrix has the following four real-value scalars: the magnitude and the phase of the cross-impedance, the magnitude and the phase of the self-impedance. Simple expressions of the electromagnetic mutual impedance, in simple closed forms are introduced, veering away from lengthy and complicated expressions. The numerical values of the mutual and self-impedance are obtained from the computer electomagnetics simulation software, EMCoS VLab. These VLab data are then least-squares fit to various candidate functions of few degrees-of-freedom, to arrive at a good "phenomenological" model. The phenomenological models are expressed in terms of the dipoles' skew angle, separation, and common length. The three significant contributions of this dissertation are: (1) obtain the phenomenological models that best represent the VLab data, (2) interpret the models in terms of electromagnetic considerations and (3) illustrate the usefulness of the obtained phenomenological models in estimating an incident source's direction-of-arrival.

List of Publications

Journal paper:

1. "How two crossed dipoles' self/mutual impedance varies with their non-orthogonality, length & separation," submitted to *IEEE Transactions on Antennas and Propagation.*

Conference papers:

1. "Mis-modeling and mis-correction of mutual coupling in an antenna array - A case study in the context of direction finding using a linear array of identical dipoles," *IEEE International Conference on Signal and Image Processing*, 2016.

2. "Electromagnetic coupling matrix modeling and ESPRIT-based direction finding – A case study using a uniform linear array of identical dipoles," *2nd IET International Conference on Intelligent Signal Processing*, 2015.

Acknowledgments

My heartfelt gratitude to my supervisors, Dr. Kainam Thomas Wong and Dr. Wai-Yip Tam, for their guidance and support since day one of my PhD life in PolyU. Your willingness to help motivated me to continue my PhD amidst the challenges that I have encountered along the way. The significant learnings I have acquired from this journey can be attributed to their ardent desire to extend selfless assistance which led to the successful completion of this dissertation.

My sincerest thanks to Prof. Yue Ivan Wu and Prof. Caleb Fulton, for their significant contributions in the key aspects of my dissertation. Their unselfish help prompted the completion of this substantive manuscript.

I would also like to thank my lovely wife, Marian and my adorable daughter, Gerianne Mae, for their love, prayers and inspiration. Without them, life would have been meaningless.

Above all, I would like to thank and give back all the glory and honor to the Lord God Almighty, whose overflowing love and mercy transcend everything. This opportunity would not have been possible without His blessing.

Contents

List of Figures **11**

1 Introduction **16**

1.1 Motivations 16

1.2 Objectives 18

2 Theoretical Framework **19**

2.1 Phenomenological Modeling 19

2.2 Wire Antennas 20

2.2.1 Dipole Antenna 20

2.2.2 Crossed Dipoles 23

2.3 Mutual Coupling 24

2.3.1 Mutual Coupling Effect 24

2.3.2 Mutual Coupling in Antenna Arrays 24

2.4 Mutual Impedance 26

2.5 Method of Moments 28

2.6 Computer Simulation Software 29

2.7 Direction-of-Arrival Estimation 29

3 Review of Related Literature **31**

3.1 Related studies with derived expressions involving unsolved integral equations. 31

3.2 Related studies with derived expressions involving nested summations. 36

3.3 Related study with derived expressions involving unsolved integral equations and nested summations. 39

4 Research Methodology **44**

4.1 Identification of parameters for the study. 45

4.2 Obtain numerical values of the mutual impedance matrix from VLab 46

4.3 Proposed phenomenological models 51

4.4 Perform model fitting 51

4.5 Selection of the best model fit 53

4.6 Relate the phenomenological models to electromagnetic considerations 53

4.7 Estimate a source's direction-of-arrival 53

5 Data, Results and Analyses **54**

5.1 Simulation Results from VLab 54

5.2 Model Fitting of the Mutual Impedances, $Z_{1,2}$ and $Z_{2,1}$ 58

5.2.1 Magnitude of $Z_{1,2}$ and $Z_{2,1}$ 58

5.2.2 Phase of $Z_{1,2}$ and $Z_{2,1}$ 60

5.3 Model Fitting of the Self-Impedances, $Z_{1,1}$ and $Z_{2,2}$ 61

5.3.1 Magnitude of $Z_{1,1}$ and $Z_{2,2}$ 62

5.3.2 Phase of $Z_{1,1}$ and $Z_{2,2}$ 69

6 Direction-of-Arrival Estimation to Demonstrate the Usefulness of the Proposed Models **72**

6.1 The Skewed Dipole-Pair's Electromagnetic Measurement Model . . . 72

6.2 The Data's Statistical Model 75

6.3 *MUSIC*-Based Direction Finding 77

6.4 DOA Estimation Plots 78

7 Conclusions and Future Work **103**

Bibliography 104

A Candidate Models for $|Z_{1,2}| = |Z_{2,1}|$ **122**

A.1 Model 1 122

A.2 Model 2 123
A.3 Model 3 123
A.4 Model 4 124
A.5 Model 5 124
A.6 Model 6 125
A.7 Model 7 125
A.8 Model 8 126
A.9 Model 9 126
A.10 Model 10 127
A.11 Model 11 127
A.12 Model 12 128
A.13 Model 13 129
A.14 Model 14 130
A.15 Model 15 131
A.16 Model 16 132
A.17 Model 17 133
A.18 Model 18 134
A.19 Model 19 135

B Candidate Models for $\angle Z_{1,2} = \angle Z_{2,1}$ 136

B.1 Model 1 136
B.2 Model 2 137
B.3 Model 3 139
B.4 Model 4 140

C Candidate Models for $|Z_{1,1}| = |Z_{2,2}|$ 142

C.1 Model 1 142
C.2 Model 2 144
C.3 Model 3 145
C.4 Model 4 146
C.5 Model 5 147

C.6 Model 6 148
C.7 Model 7 149
C.8 Model 8 150
C.9 Model 9 151
C.10 Model 10 152
C.11 Model 11 153
C.12 Model 12 154
C.13 Model 13 155
C.14 Model 14 156
C.15 Model 15 157
C.16 Model 16 158
C.17 Model 17 159
C.18 Model 18 161
C.19 Model 19 162
C.20 Model 20 163
C.21 Model 21 165
C.22 Model 22 166

D Candidate Models for $\angle Z_{1,1} = \angle Z_{2,2}$ **168**

D.1 Model 1 168
D.2 Model 2 169
D.3 Model 3 170
D.4 Model 4 171
D.5 Model 5 172
D.6 Model 6 173
D.7 Model 7 174
D.8 Model 8 175
D.9 Model 9 176
D.10 Model 10 177
D.11 Model 11 178
D.12 Model 12 179

D.13 Model 13 180
D.14 Model 14 181
D.15 Model 15 183

List of Figures

1.1 The spatial geometry between two crossed dipoles of non-orthogonal orientation. Here, the inter-dipole separation Δ is greatly exaggerated for visual clarity. 17

2.1 The geometry of a dipole with length L. The feeding gap is at the center. 20

2.2 The "figure 8" radiation pattern of a horizontal dipole's axis. Maximum radiation is perpendicular to the dipole's axis, while "null" radiation is along its axis. 21

2.3 The voltage and current distributions along a half-wave dipole. Current is maximum at the center and minimum at both ends. 22

2.4 Crossed dipoles with common length L, elevated on the $x' - y'$ plane. . . 23

2.5 The mutual coupling in transmit mode [34]. Here, antenna n is excited and antenna m is the induced antenna. 25

2.6 The mutual coupling in the receive mode [34]. Antenna m first receives the incident wave. 25

2.7 Two-port network system. The mutual impedance between ports 1 and 2 are derived here. 27

3.1 The six independent variables $L_1, L_2, y_0, z_0, \theta$ and ϕ [5]. 32

3.2 Relationships among $\alpha, \alpha_1, \alpha_2, \rho, r, r_1, r_2$ and s [5]. 32

3.3 Cartesian components of the vector $\bar{\mathbf{s}}$ [5]. 33

3.4 Geometry of coplanar-skew dipoles [104]. The effective length vectors method is used here. 34

3.5 The geometry of coplanar-skew dipoles [7]. 36

3.6 The linear dipole in cylindrical coordinate system [7]. 36

3.7 The monopole and its coordinate system 38

3.8 The two monopoles on z and t axes, parallel to the xz plane with distance d from each other and with skew angle ψ. 38

3.9 Geometry of nonplanar slanted dipoles [113]. 40

4.1 The step-by-step research process of the dissertation. 44

4.2 The coplanar and cocentered crossed dipoles. Here, there is no mutual coupling. 45

4.3 The nonplanar and cocentered crossed dipoles. Here, still there is no mutual coupling. 45

4.4 The skewed nonplanar and cocentered crossed dipoles. Here, there is now mutual coupling. 46

4.5 The geometry of the skewed crossed dipoles under study. The independent variables are: the dipoles' common length L, the skew angle φ, and the inter-dipole separation Δ. 47

4.6 Geometry view of the skewed crossed dipoles in VLab. Here, the skewed crossed dipoles is constructed based on set variables. 48

4.7 Model view of the skewed crossed dipoles in VLab. Cables definition based on curves structure and devices modeling is set here. 48

4.8 Mesh view of the skewed crossed dipoles in VLab. Model conversion to discrete elements (i.e. wire segments) for calculation is done on mesh mode. 49

5.1 The 3D plot of $|Z_{1,2}|$ at $\frac{L}{\lambda} = 1.00, \forall\{\frac{\Delta}{\lambda}, \varphi\}$ from VLab. Here, $|Z_{1,2}|$ increases with increasing φ, and $|Z_{1,2}|$ decreases with increasing $\frac{\Delta}{\lambda}$. 55

5.2 The 3D plot of $|Z_{1,2}|$ at $\varphi = 45°, \forall\{\frac{\Delta}{\lambda}, \frac{L}{\lambda}\}$ from VLab. $|Z_{1,2}|$ also increases with increasing $\frac{L}{\lambda}$. 55

5.3 The 3D plot of the unwrapped $\angle Z_{1,2}$ at $\varphi = 45°, \forall\{\frac{\Delta}{\lambda}, \frac{L}{\lambda}\}$ from VLab. The $\angle Z_{1,2}$ is almost linear with $\frac{\Delta}{\lambda}$ and $\frac{L}{\lambda}$. $\angle Z_{1,2}$ is also independent of the skew angle φ. 56

5.4 The 3D plot of $|Z_{1,1}|$ at $\frac{L}{\lambda} = 1.00$, $\forall\{\frac{\Delta}{\lambda}, \varphi\}$ from VLab. The behavior of $|Z_{1,1}|$ with respect to $\frac{\Delta}{\lambda}$ is like a dampened sinusoid. 56

5.5 The 3D plot of $|Z_{1,1}|$ at $\varphi = 45°$, $\forall\{\frac{\Delta}{\lambda}, \frac{L}{\lambda}\}$ from VLab. The minumum value of $|Z_{1,1}|$ is near $\frac{L}{\lambda} = 0.50$. 57

5.6 The 3D plot of $\angle Z_{1,1}$ at $\varphi = 45°$, $\forall\{\frac{\Delta}{\lambda}, \frac{L}{\lambda}\}$ from VLab. The data for $\angle Z_{1,1}$ shows a sinuoidal relationship with $\frac{L}{\lambda}$. 57

5.7 How $|Z_{1,2}\csc(\varphi)| = |Z_{2,1}\csc(\varphi)|$ of (5.1) varies with $\frac{\Delta}{\lambda}$ and $\frac{L}{\lambda}$. . . . 59

5.8 How $\angle Z_{1,2} = \angle Z_{2,1}$ of (5.3) varies with $\frac{\Delta}{\lambda}$ and $\frac{L}{\lambda}$. The $\angle Z_{1,2} = \angle Z_{2,1}$ varies linearly with $\frac{\Delta}{\lambda}$ and $\frac{L}{\lambda}$. 61

5.9 How $P_1\left(\varphi, \frac{\Delta}{\lambda}\right)$ varies with φ and $\frac{\Delta}{\lambda}$ 63

5.10 How $P_3\left(\frac{L}{\lambda}\right)$ varies with $\frac{L}{\lambda}$. Observe that resonance is near $\frac{L}{\lambda} = 0.50$. This minimum value is exactly at $\frac{L}{\lambda} = 0.48$. 65

5.11 How $P_2\left(\frac{\Delta}{\lambda}\right)$ varies with $\frac{\Delta}{\lambda}$. Here, there are 4 peaks and nulls. The absolute maximum is at $\frac{\Delta}{\lambda} = 0.13$ with an amplitude of 0.96, while the absolute minimum is at $\frac{\Delta}{\lambda} = 0.38$ with an amplitude of -0.90. . 66

5.12 How $Q\left(\frac{\Delta}{\lambda}\right)$ varies with $\frac{\Delta}{\lambda}$ 70

5.13 How $\angle Z_{1,1}$ varies with $\frac{\Delta}{\lambda}$ and $\frac{L}{\lambda}$. 70

6.1 The square array of crossed dipoles separated by a distance of 14λ. The inter-pair coupling is negligible at this distance. 75

6.2 How the RMSE of (a) $\hat{\theta}$ and (b) $\hat{\phi}$ varies with the SNR. Here, $\frac{L}{\lambda} = 0.45$, $\varphi = 45°$, $\frac{\Delta}{\lambda} = 0.04$, $\theta = 26°$, $\phi = 12°$, $\gamma = 44°$, $\eta = -20°$. 79

6.3 How the RMSE of (a) $\hat{\theta}$ and (b) $\hat{\phi}$ varies with the SNR. Here, $\frac{L}{\lambda} = 0.45$, $\varphi = 45°$, $\frac{\Delta}{\lambda} = 0.04$, $\theta = 55°$, $\phi = 53°$, $\gamma = 19°$, $\eta = 32°$. 80

6.4 How the RMSE of (a) $\hat{\theta}$ and (b) $\hat{\phi}$ varies with the SNR. Here, $\frac{L}{\lambda} = 0.50$, $\varphi = 45°$, $\frac{\Delta}{\lambda} = 0.01$, $\theta = 50°$, $\phi = 36°$, $\gamma = 15°$, $\eta = 40°$. 81

6.5 How the RMSE of (a) $\hat{\theta}$ and (b) $\hat{\phi}$ varies with the SNR. Here, $\frac{L}{\lambda} = 0.50$, $\varphi = 45°$, $\frac{\Delta}{\lambda} = 0.01$, $\theta = 40°$, $\phi = 65°$, $\gamma = 33°$, $\eta = -23°$. 82

6.6 How the RMSE of (a) $\hat{\theta}$ and (b) $\hat{\phi}$ varies with the SNR. Here, $\frac{L}{\lambda} = 0.50$, $\varphi = 45°$, $\frac{\Delta}{\lambda} = 0.01$, $\theta = 32°$, $\phi = 28°$, $\gamma = 52°$, $\eta = -28°$. 83

6.7 How the RMSE of (a) $\hat{\theta}$ and (b) $\hat{\phi}$ varies with the SNR. Here, $\frac{L}{\lambda} = 0.50$, $\varphi = 45°$, $\frac{\Delta}{\lambda} = 0.01$, $\theta = 32°$, $\phi = 28°$, $\gamma = 50°$, $\eta = -32°$. 84
6.8 How the RMSE of (a) $\hat{\theta}$ and (b) $\hat{\phi}$ varies with the SNR. Here, $\frac{L}{\lambda} = 0.50$, $\varphi = 45°$, $\frac{\Delta}{\lambda} = 0.02$, $\theta = 53°$, $\phi = 30°$, $\gamma = 15°$, $\eta = 45°$. 85
6.9 How the RMSE of (a) $\hat{\theta}$ and (b) $\hat{\phi}$ varies with the SNR. Here, $\frac{L}{\lambda} = 0.50$, $\varphi = 45°$, $\frac{\Delta}{\lambda} = 0.02$, $\theta = 48°$, $\phi = 28°$, $\gamma = 16°$, $\eta = 40°$. 86
6.10 How the RMSE of (a) $\hat{\theta}$ and (b) $\hat{\phi}$ varies with the SNR. Here, $\frac{L}{\lambda} = 0.50$, $\varphi = 45°$, $\frac{\Delta}{\lambda} = 0.02$, $\theta = 10°$, $\phi = 36°$, $\gamma = 20°$, $\eta = 54°$. 87
6.11 How the RMSE of (a) $\hat{\theta}$ and (b) $\hat{\phi}$ varies with the SNR. Here, $\frac{L}{\lambda} = 0.50$, $\varphi = 45°$, $\frac{\Delta}{\lambda} = 0.02$, $\theta = 48°$, $\phi = 34°$, $\gamma = 14°$, $\eta = 22°$. 88
6.12 How the RMSE of (a) $\hat{\theta}$ and (b) $\hat{\phi}$ varies with the SNR. Here, $\frac{L}{\lambda} = 0.50$, $\varphi = 45°$, $\frac{\Delta}{\lambda} = 0.02$, $\theta = 12°$, $\phi = 48°$, $\gamma = 16°$, $\eta = 52°$. 89
6.13 How the RMSE of (a) $\hat{\theta}$ and (b) $\hat{\phi}$ varies with the SNR. Here, $\frac{L}{\lambda} = 0.50$, $\varphi = 45°$, $\frac{\Delta}{\lambda} = 0.02$, $\theta = 14°$, $\phi = 44°$, $\gamma = 14°$, $\eta = 56°$. 90
6.14 How the RMSE of (a) $\hat{\theta}$ and (b) $\hat{\phi}$ varies with the SNR. Here, $\frac{L}{\lambda} = 0.50$, $\varphi = 45°$, $\frac{\Delta}{\lambda} = 0.04$, $\theta = 22°$, $\phi = 42°$, $\gamma = 28°$, $\eta = 60°$. 91
6.15 How the RMSE of (a) $\hat{\theta}$ and (b) $\hat{\phi}$ varies with the SNR. Here, $\frac{L}{\lambda} = 0.55$, $\varphi = 45°$, $\frac{\Delta}{\lambda} = 0.02$, $\theta = 34°$, $\phi = 46°$, $\gamma = 16°$, $\eta = -8°$. 92
6.16 How the RMSE of (a) $\hat{\theta}$ and (b) $\hat{\phi}$ varies with the SNR. Here, $\frac{L}{\lambda} = 0.55$, $\varphi = 45°$, $\frac{\Delta}{\lambda} = 0.02$, $\theta = 21°$, $\phi = 46°$, $\gamma = 27°$, $\eta = -14°$. 93
6.17 How the RMSE of (a) $\hat{\theta}$ and (b) $\hat{\phi}$ varies with the SNR. Here, $\frac{L}{\lambda} = 0.60$, $\varphi = 45°$, $\frac{\Delta}{\lambda} = 0.01$, $\theta = 30°$, $\phi = 45°$, $\gamma = 24°$, $\eta = -8°$. 94
6.18 How the RMSE of (a) $\hat{\theta}$ and (b) $\hat{\phi}$ varies with the SNR. Here, $\frac{L}{\lambda} = 0.60$, $\varphi = 45°$, $\frac{\Delta}{\lambda} = 0.02$, $\theta = 19°$, $\phi = 84°$, $\gamma = 56°$, $\eta = 41°$. 95
6.19 How the RMSE of (a) $\hat{\theta}$ and (b) $\hat{\phi}$ varies with the SNR. Here, $\frac{L}{\lambda} = 0.60$, $\varphi = 45°$, $\frac{\Delta}{\lambda} = 0.02$, $\theta = 15°$, $\phi = 53°$, $\gamma = 83°$, $\eta = 45°$. 96
6.20 How the RMSE of (a) $\hat{\theta}$ and (b) $\hat{\phi}$ varies with the SNR. Here, $\frac{L}{\lambda} = 0.75$, $\varphi = 45°$, $\frac{\Delta}{\lambda} = 0.04$, $\theta = 48°$, $\phi = 56°$, $\gamma = 14°$, $\eta = -14°$. 97
6.21 How the RMSE of (a) $\hat{\theta}$ and (b) $\hat{\phi}$ varies with the SNR. Here, $\frac{L}{\lambda} = 0.75$, $\varphi = 45°$, $\frac{\Delta}{\lambda} = 0.04$, $\theta = 22°$, $\phi = 40°$, $\gamma = 24°$, $\eta = -58°$. 98

6.22 How the RMSE of (a) $\hat{\theta}$ and (b) $\hat{\phi}$ varies with the SNR. Here, $\frac{L}{\lambda} = 0.75$, $\varphi = 45°$, $\frac{\Delta}{\lambda} = 0.04$, $\theta = 36°$, $\phi = 48°$, $\gamma = 14°$, $\eta = -68°$. 99

6.23 How the RMSE of (a) $\hat{\theta}$ and (b) $\hat{\phi}$ varies with the SNR. Here, $\frac{L}{\lambda} = 0.85$, $\varphi = 45°$, $\frac{\Delta}{\lambda} = 0.01$, $\theta = 46°$, $\phi = 36°$, $\gamma = 18°$, $\eta = -24°$. 100

6.24 How the RMSE of (a) $\hat{\theta}$ and (b) $\hat{\phi}$ varies with the SNR. Here, $\frac{L}{\lambda} = 1.00$, $\varphi = 45°$, $\frac{\Delta}{\lambda} = 0.01$, $\theta = 65°$, $\phi = 38°$, $\gamma = 13°$, $\eta = -10°$. 101

7.1 The spatial geometry of cocentered non-orthogonal loop and dipole. 104

A.1 How φ affects the coefficients of the 3-DoF model in (A.13). 129

A.2 How φ affects the coefficients of the 3-DoF model in (A.14). 130

A.3 How φ affects the coefficients of the 3-DoF model in (A.15). 131

A.4 How φ affects the coefficients of the 3-DoF model in (A.16). 132

A.5 How φ affects the coefficients of the 4-DoF model in (A.17). 133

A.6 How φ affects the coefficients of the 3-DoF model in (A.18). 134

A.7 How φ affects the coefficients of the 5-DoF model in (A.19). 135

C.1 How $\frac{L}{\lambda}$ affects the coefficients of the 8-DoF model in (C.17). 159

C.2 How $\frac{L}{\lambda}$ affects the coefficients of the 8-DoF model in (C.18). 161

C.3 How φ affects the coefficients of the 8-DoF model in (C.19). 162

C.4 How $\frac{L}{\lambda}$ affects the coefficients of the 8-DoF model in (C.20). 163

C.5 How φ affects the coefficients of the 5-DoF model in (C.21). 165

C.6 How φ affects the coefficients of the 5-DoF model in (C.22). 166

D.1 How φ affects the coefficients of the 8-DoF model in (D.12). 179

D.2 How $\frac{L}{\lambda}$ affects the coefficients of the 8-DoF model in (D.13). 181

D.3 How $\frac{L}{\lambda}$ affects the coefficients of the 8-DoF model in (D.14). 182

D.4 How $\frac{L}{\lambda}$ affects the coefficients of the 9-DoF model in (D.15). 183

Chapter 1

Introduction

Introduction

This chapter introduces the motivations and the objectives of the research. While mutual coupling among antennas within an array is oftentimes overlooked, an attempt is made here to model this phenomenon for the special case of a pair of skewed crossed dipoles, in simple tractable closed forms.

1.1 Motivations

Cross dipoles have been popularly used in many applications such as in beamforming [81, 99], direction-of-arrival and polarization estimation [28, 86, 115, 118, 123, 126]. The crossed dipoles' differently polarized elements can discriminate incident sources based on their different polarizations, aside from their different frequency spectra and their different directions-of-arrival. When two dipoles are mounted at right angles with each other, electromagnetic coupling would not exist between them.

One unique Cartesian element of the incident electric-field vector is measured by each dipole. The determination of the polarization and azimuth direction-of-arrival of the electromagnetic wavefront can be achieved by only one pair of crossed dipoles. For the relevant literature, please refer to [103].

In a real-world scenario, the orthogonality of crossed dipoles may not always be actualized or maintained, so that mutual coupling results between the two dipoles.

Please refer to Figure 1.1, which defines the skew angle φ (i.e. the angular deviation from perpendicularity) between two identical dipoles - one on the z-axis and the other on the y'-z' plane.

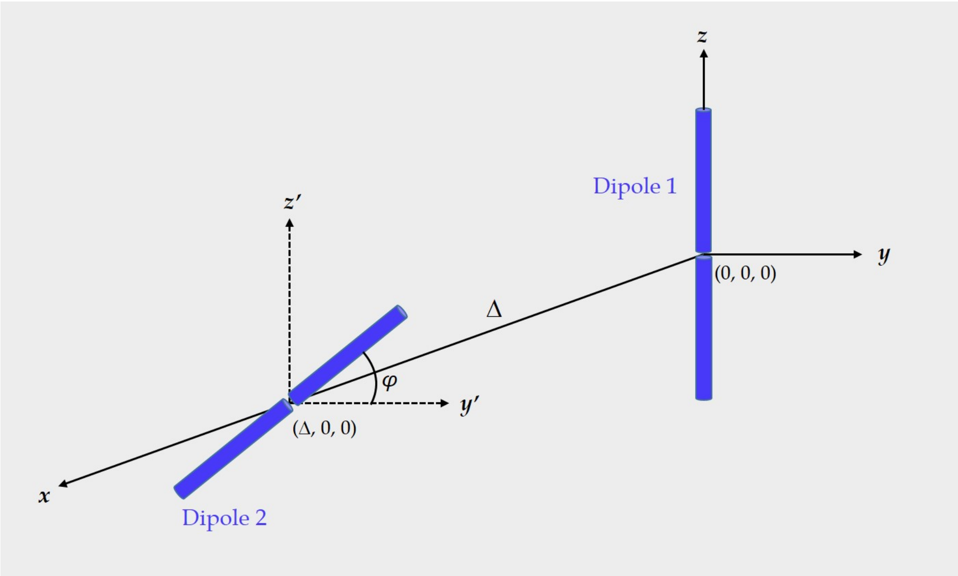

Figure 1.1: The spatial geometry between two crossed dipoles of non-orthogonal orientation. Here, the inter-dipole separation Δ is greatly exaggerated for visual clarity.

For a pair of skewed dipoles, there had been various studies on the mutual impedance, but they all introduced very highly complicated mathematical expressions for the mutual impedance. Some of them introduced very long and complicated equations as in [4], complex unsolved exponential integral equations [1, 5, 8, 12, 104, 113], and nested summations [7, 32, 105, 113]. While [5, 7, 8, 11, 47, 51, 95, 104, 105] opted to only plotting the mutual impedance.

This dissertation introduces a new and different approach – "phenomenological" or "behavioral" modeling in mutual coupling. Phenomenological modeling, being new on mutual coupling, has been used in wireless propagation fading and in nonlinear amplifier's input/output relationship. These phenomenological models on mutual impedance would feature simple and tractable expressions as a result of least squares data fitting. These expressions involve three independent variables: the dipoles' skew angle (φ), the wavelength-normalized inter-dipole separation ($\frac{\Delta}{\lambda}$), and the wavelength-normalized dipole length ($\frac{L}{\lambda}$).

1.2 Objectives

The main objective of this dissertation is to obtain phenomenological models of mutual impedance for skewed crossed dipoles.

The investigation's specific steps are:

1. to use computer electromagnetics simulation software (i.e. EMCoS VLab) to calculate the mutual impedance between skewed crossed dipoles.

2. to propose models with unknown coefficients to model the VLab simulation data of the mutual impedance matrix.

3. to least-squares fit the VLab simulation data to the above simple phenomenological models with the goal of obtaining the optimized value of the unknown coefficients.

4. to select the best model fit among the proposed functions using coefficient of determination, R^2, as goodness-of-fit criterion.

5. to interpret the obtained phenomenological models through electromagnetic considerations.

6. to use the phenomenological models in estimating an incident emitter's direction-of-arrival

Summary

The adoption of phenomenological modeling to model the mutual coupling or any other phenomena have not been explored in the field of antenna array signal processing. Hence, this concept is unprecedented and adds to the body of knowledge in the field of antenna array signal processing. As the motivations and the objectives of this dissertation have been clearly established, it is time to discuss the key concepts and main theories that will aid in satisfying the research objectives. This will be done in the next chapter.

Chapter 2

Theoretical Framework

Introduction

This chapter discusses the concept of "phenomenological modeling" and basic theories of a dipole antenna and crossed dipoles. The concepts of mutual coupling and the "method of moments" are also briefly discussed. The last section of the chapter discusses direction-of-arrival estimation, a critical component of this dissertation as it validates if the modeling has been successful.

2.1 Phenomenological Modeling

Scientific modeling like "phenomenological" or "behavioral" approach involves empirical relationship among phenomena. Phenomenological modeling merely describes the occurrence which is consistent with fundamental theories but not really derived from first principles. Some phenomenological models even goes beyond and contradict fundamental theories. The mathematical tractability of phenomenological models is its advantage over theories.

Phenomenological modeling has found applications in the wireless communication, fiber optics, and amplifiers. In the area of wireless communication, [130] used phenomenological modeling to model the *in vivo* wireless channel. The data were obtained using the ANSYS High Frequency Electromagnetic Solvers (HFSS) simulation software. In fiber optics, [36] carried out phenomenological modeling of the output characteristics of the integrated multifrequency laser (MFL), in which resulting model has found usage in performance monitoring, device evaluation and improved transmitter design.

2.2 Wire Antennas

Wire antennas (like dipoles and loops) are simple to construct, hence widely used. In this research, it is assumed that the cross-sectional radius of the wire is much smaller than the wavelength of the antenna. The reason for this assumption is to have only one component for the current. The assumed wire's current distribution is the major parameter to facilitate computation of the electric and magnetic fields along the antenna.

The most popular type of wire antennas, which is the dipole antenna, is discussed in detail on the succeeding subsections below.

2.2.1 Dipole Antenna

A dipole (a.k.a. doublet) is a conductive rod, split into two equal halves by a "feeding gap" where electric current enters the rod. Figure 2.1 illustrates the geometry of a center-fed dipole with length L.

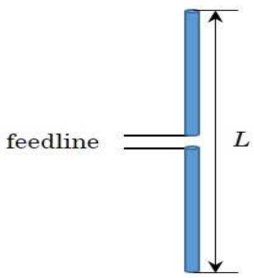

Figure 2.1: The geometry of a dipole with length L. The feeding gap is at the center.

One of the applications of dipole antenna is in radio direction finding which takes advantage of its "figure 8" radiation pattern that introduces maximum gain perpendicular to the dipole and zero gain along its axis (see Figure 2.2).

The electric and magnetic far-field radiation of a dipole with finite length, L, is

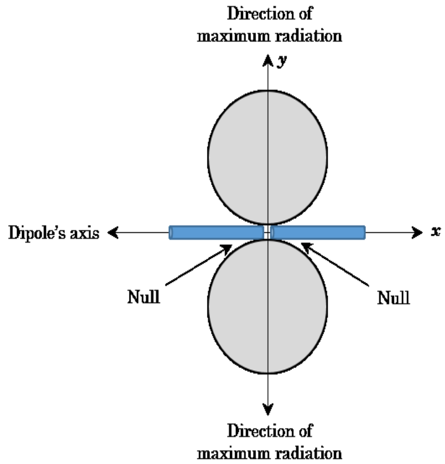

Figure 2.2: The "figure 8" radiation pattern of a horizontal dipole's axis. Maximum radiation is perpendicular to the dipole's axis, while "null" radiation is along its axis.

given by the following equations: [34]

$$E_\theta \simeq j\eta \frac{I_0 e^{-j\beta r}}{2\pi r}\left[\frac{\cos\left(\frac{\beta L}{2}\cos\theta\right)-\cos\left(\frac{\beta L}{2}\right)}{\sin\theta}\right] \tag{2.1}$$

$$H_\phi = \frac{E_\theta}{\eta} \simeq j\frac{I_0 e^{-j\beta r}}{2\pi r}\left[\frac{\cos\left(\frac{\beta L}{2}\cos\theta\right)-\cos\left(\frac{\beta L}{2}\right)}{\sin\theta}\right], \tag{2.2}$$

where η denotes the intrinsic impedance (120π or 377 ohms in free-space), I_0 denotes the maximum current flowing into the antenna, r is the far-field distance, $\beta\left(=\frac{2\pi}{\lambda}\right)$ denotes the wave number, and θ denotes the inclination angle.

A "short dipole" has length that is less than half-wavelength. This minimum length makes the dipole resonant at the operating frequency. The "short dipole" is used in cases where the full half-wave dipole would require considerable length and becomes unwieldy.

Half-wave dipole (i.e. dipole with $L = \lambda/2$) is widely used in many applications, such as receiving antenna in TV and FM broadcasting and base station antenna in cellular telephony, because of its omnidirectional radiation pattern in the H-plane.

At $L = \frac{\lambda}{2}$, Equations 2.1 and 2.2 become

$$E_\theta \simeq j\eta \frac{I_0 e^{-j\beta r}}{2\pi r}\left[\frac{\cos\left(\frac{\pi}{2}\cos\theta\right)}{\sin\theta}\right] \quad (2.3)$$

$$H_\phi = \frac{E_\theta}{\eta} \simeq j\frac{I_0 e^{-j\beta r}}{2\pi r}\left[\frac{\cos\left(\frac{\pi}{2}\cos\theta\right)}{\sin\theta}\right]. \quad (2.4)$$

Figure 2.3 shows the current and voltage distributions of a center-fed half-wave dipole. The current vanishes at the end points (i.e. maximum at the center and minimum at both ends), while the voltage vanishes at the center and maximum at both ends.

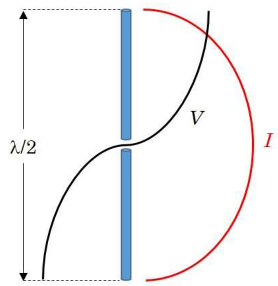

Figure 2.3: The voltage and current distributions along a half-wave dipole. Current is maximum at the center and minimum at both ends.

Common applications of a dipole as a single antenna are: television indoor antenna (i.e. "rabbit ears" antenna) , FM broadcast receiving antennas, HF shortwave communications (i.e. in the form of a horizontal dipole), and a mast radiator for medium-frequency and low-frequency transmissions.

Multiple dipoles can form different types of antenna array. The collinear antenna array [3] which is composed of stack vertical dipoles end-to-end that is fed in phase to form an omnidirectional pattern used in very high frequency (VHF) and ultra high frequency (UHF) bands. Broadside array, end-fire array and parasitic array [73] are other remarkable dipole antenna arrays used as radiating systems.

2.2.2 Crossed Dipoles

Known at first to be a “turnstile” antenna, invented by Brown [2] in the early 1930s, crossed dipoles are composed of two dipoles orthogonally aligned to each other (See Fig. 2.4).

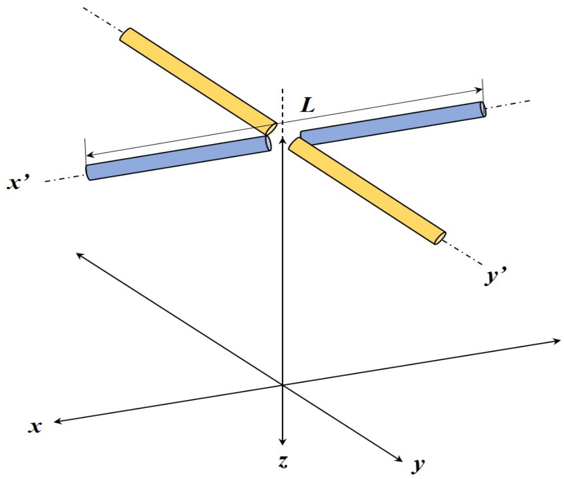

Figure 2.4: Crossed dipoles with common length L, elevated on the $x' - y'$ plane.

A crossed-dipole antenna can be configured to provide omnidirectional [89, 139] or isotropic radiation with dual [85] or circular polarization [117, 124], by varying its feeding structure. It can also be used for single-band, multiband [128] and broadband operations [91] when combined with additional antenna elements.

The crossed dipoles, which are orthogonal and co-centered, introduce zero mutual coupling as there is no radial component of the near electric field from the dipole in the normal plane through the dipole center [92].

Crossed dipoles are nowadays a popular choice for applications such as TV and FM broadcasting, mobile and satellite communications, RFID, and wireless LANs [127].

Crossed dipoles will be investigated in this dissertation at various values of the skew angles, of the separation between the two dipoles, and of the lengths of the dipoles.

2.3 Mutual Coupling

Given the many advantages of using antenna arrays, one drawback is the presence of mutual coupling. Mutual coupling is the electromagnetic interaction among antenna elements in an antenna array.

The current flowing into one antenna element creates an electromagnetic field (EM) field. If nearby antenna element/s is/are exposed to EM field from the excited antenna element, then current is induced to the exposed elements thereby causing mutual coupling.

2.3.1 Mutual Coupling Effect

According to IEEE Standard Definitions and Terms for Antennas, mutual coupling effect is defined as follows: "2.244. mutual coupling effect (A) (on the radiation pattern of an array antenna) change in antenna pattern from the case when a particular feeding structure is attached to the array and mutual impedances among elements are ignored in deducing the excitation to the case when the same feeding structure is attached to the array and mutual impedances among elements are included in deducing the excitation. (B) (on input impedance of an array element). For array antennas, the change in input impedance of an array element from the case when all other elements are present but open-circuited to the case when all other elements are present and excited." [24]

2.3.2 Mutual Coupling in Antenna Arrays

The explanation for the transmit and receive modes of the antennas arrays are taken from [34].

Transmit Mode

Antenna n is excited, generates energy traveling toward the antenna (0) and radiates the EM field (1) into space. Antenna m is exposed to the radiated field (2) and reradiates the intercepted field (3) while allowing some of the energy towards the source (4) and the remaining energy sent toward antenna n (5). This continues indefinitely. The same action applies if antenna m is powered while antenna n is the parasitic element. If antennas m and n are both excited at the same time, the total field is the vector sum of the radiated and reradiated fields by and from each antenna.

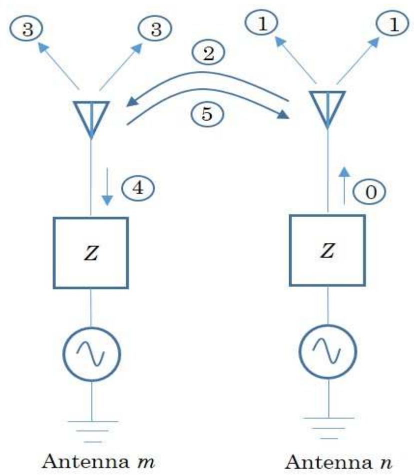

Figure 2.5: The mutual coupling in transmit mode [34]. Here, antenna n is excited and antenna m is the induced antenna.

Receive Mode

The incident wave (0) first directly arrives at antenna m where current is induced. There will be reradiation into space (2), and part will be intercepted by antenna n (3) where it will be vectorially summed together with the incident wave (0), and part also travels toward the feed point (1). A reflected wave (4) can also occur.

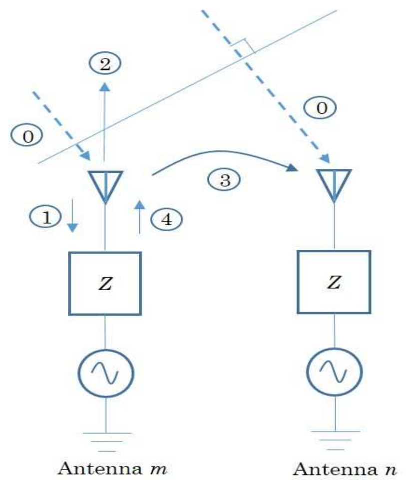

Figure 2.6: The mutual coupling in the receive mode [34]. Antenna m first receives the incident wave.

2.4 Mutual Impedance

In this dissertation, we characterize mutual coupling through mutual impedance. Mutual impedance, according to IEEE Standard Definitions and Terms for Antennas is, "any two terminal pairs in a multielement array antenna is equal to the open-circuit voltage produced at the first terminal pair divided by the current supplied to the second when all other terminal pairs are open-circuited [24]."

Consider an K-element array represented as K-port network. The voltage across each element is given by, [74]

$$\left.\begin{aligned} V_1 &= Z_{1,1}I_1 + Z_{1,2}I_2 + \ldots + Z_{1,K}I_K \\ V_2 &= Z_{2,1}I_1 + Z_{2,2}I_2 + \ldots + Z_{2,K}I_K \\ &\vdots \\ V_K &= Z_{K,1}I_1 + Z_{K,2}I_2 + \ldots + Z_{K,K}I_K \end{aligned}\right\}. \tag{2.5}$$

I_n denotes the current the kth element, $k = 1, 2, ..., K$.

$$Z_{k,k} = \frac{V_k}{I_k}, \tag{2.6}$$

denotes the kth element's self-impedance when the rest of the elements are in open-circuit.

$$Z_{k,p} = \frac{V_p}{I_k}, \tag{2.7}$$

denotes mutual impedance between two elements p and k. [74]

The new input impedance or the driving point impedance (a.k.a. active impedance) of each element in the array caused by mutual coupling is [74]

$$Z_{kd} = \frac{V_k}{I_k} = Z_{1,1}\frac{I_1}{I_k} + Z_{1,2}\frac{I_2}{I_k} + \ldots + Z_{1,K}\frac{I_K}{I_k}. \tag{2.8}$$

Consider K=2 and a two-port network system in Figure 2.7. The voltages across the two elements are: [34]

$$\left.\begin{aligned} V_1 &= Z_{1,1}I_1 + Z_{1,2}I_2 \\ V_2 &= Z_{2,1}I_1 + Z_{2,2}I_2 \end{aligned}\right\}, \tag{2.9}$$

where

$$Z_{1,1} = \left.\frac{V_1}{I_1}\right|_{I_2=0}. \tag{2.10}$$

$Z_{1,1}$ denotes the input impedance at port 1(port 2, open circuit). When I_1 is set to

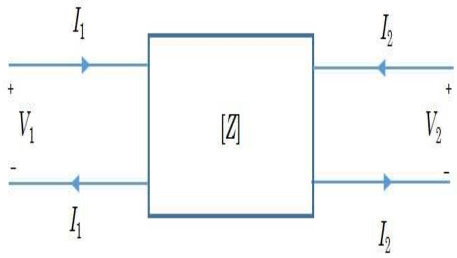

Figure 2.7: Two-port network system. The mutual impedance between ports 1 and 2 are derived here.

zero, $Z_{1,2}$, is

$$Z_{1,2} = \left.\frac{V_1}{I_2}\right|_{I_1=0}. \tag{2.11}$$

$Z_{1,2}$ is the mutual impedance at port 1 when it is open-circuited and port 2 is excited. Likewise, when I_2 is set to zero, $Z_{2,1}$, is

$$Z_{2,1} = \left.\frac{V_2}{I_1}\right|_{I_2=0}. \tag{2.12}$$

$Z_{2,1}$ is the mutual impedance at port 2 when it is open-circuited and port 1 is excited. And,

$$Z_{2,2} = \left.\frac{V_2}{I_2}\right|_{I_1=0}. \tag{2.13}$$

$Z_{2,2}$ denotes the input impedance at port 2 (port 1, open-circuit). Note that for a network that is reciprocal, $Z_{1,2} = Z_{2,1}$. When each of the antennas 1 and 2 is radiating in an unbounded medium, the input impedances are $Z_{1,1}$ and $Z_{2,2}$, respectively. But, the presence of an obstacle or another element in close proximity with the other would alter the input impedance. This alteration would depend on the type of antenna, the relative positioning of the elements and the feed type to excite the elements. With this consideration, (2.9) can be rewritten as, [34]

$$\left.\begin{array}{l} Z_{1d} = \frac{V_1}{I_1} = Z_{1,1} + Z_{1,2}\left(\frac{I_2}{I_1}\right) \\ Z_{2d} = \frac{V_2}{I_2} = Z_{2,2} + Z_{2,1}\left(\frac{I_1}{I_2}\right) \end{array}\right\}. \tag{2.14}$$

Z_{1d} and Z_{2d} denote the driving point impedances of antennas 1 and 2, respectively. Therefore, in matching antennas, it is the driving point impedance that should be matched.

Dealing with the effect of mutual coupling would improve the performance of an antenna. However, we would also have to deal with the complexity of the underlying computational analysis associated with it.

2.5 Method of Moments

The "Method of Moments" (MoM), for the last 50 years, has been providing solutions to large number of electromagnetic problems. Harrington's book [6] is the first to explore MoM as numerical solution to electromagnetic field problems. Since then, MoM has evolved to be the most popular computational technique in many researches on antennas and electromagnetics. [9, 10, 35, 40, 42, 50, 55, 132] are some MoM based studies particularly on dipoles and loops .

As part of the field of "computational electromagnetics" (CEM), which involves the digital computer in solving electromagnetic problems, MoM is most applicable in solving integral-equation-based frequency-domain problems [93].

There are two most popular techniques used in the computation of self and mutual impedances, which are integral form based induced currents and voltages at the antenna terminals, namely, the induced electromotive (EMF) method and integral equation-method of method (IE-MoM) . The IE-MoM is preferred over induced EMF because induced EMF does not accurately take into consideration the wire's radius and the feeding gap. Moreover, IE-MoM is the more appropriate solution to dipoles with larger radii and complex antenna arrays including arrays with skewed arrangements [111]. Hence, the MoM is the right computational technique to be used in obtaining the numerical values of the mutual impedance on the antenna array investigated on this dissertation.

2.6 Computer Simulation Software

Computer simulation tools are needed in dealing with very long mathematical formulations and complex programming. Modeling, such as phenomenological modeling, has been a very successful area in research because of the advent of supercomputers which can provide good numerical data suitable for regression analysis.

The EMCoS "VLab" is an antenna simulation software for antenna parameter calculations. For the calculation of mutual impedance values, the "VLab" uses the MOM technique through their program core module called "TriD". "TriD" is capable of solving electromagnetic problems for the complicated metal and dielectric structures either in free space or over infinite ground plane. It is based on Method of Moments scheme by Poggio-Miller-Chang-Harrington-Wu (PMCHW) coupled with Rao-Wilton-Glisson's (RWG) triangle and improved wire and wire to surface basis functions.

Unlike any other simulation tools, "VLab" features full-functional MOM based 3D EM solver with CAD interface. You can control and set your parameters through its graphical user interface (GUI) in the Geometry, Model and Mesh modes.

2.7 Direction-of-Arrival Estimation

Direction-of-arrival (DOA) estimation has been a popular and extensively studied area in array signal processing. Many algorithms have been developed in order to accurately localize the sources of incident signals. Subspace-based algorithms such as MUltiple SIgnal Classification (MUSIC) [16] is often an appropriate methods if the estimation requires high-resolution multiple uncorrelated narrowband signal sources.

The performance of the estimation is usually gauged by the root-mean-square error (RMSE) versus the signal-to-noise ratio (SNR). Obviously, the RMSE should be decreasing with increasing SNR.

Summary

The significant necessary concepts and essential components of this dissertation have already been discussed veering away from presenting too much mathematical equations.

The mutual impedance has been chosen to characterize mutual coupling due to the availability of the computer electromagnetics simulation software, EMCoS VLab, in which its core calculation program is based on method of moments.

Chapter 3

Review of Related Literature

Introduction

As mentioned in Section 1, one of the objectives of this dissertation is to obtain simple and low-dimensional phenomenological models unlike previous papers which presented very complicated equations for the mutual impedance of different configurations for the pair of dipoles. The purpose of this chapter is to show the complexity of the derived mathematical equations from different journals and conference papers already published.

3.1 Related studies with derived expressions involving unsolved integral equations.

Baker and Lagrone [5] introduced equations for the computation of complex mutual impedance between thin linear antennas shown in Figure 3.1. The primary antenna with length L_1 is drawn along the z-axis, while the secondary antenna with length L_2 is drawn on the $y' - z'$ and displaced in the y and z directions by distances of y_0 and z_0 wavelengths, respectively. The polar angle θ and azimuthal angle ϕ of the secondary antenna correspond to the spherical coordinate system.

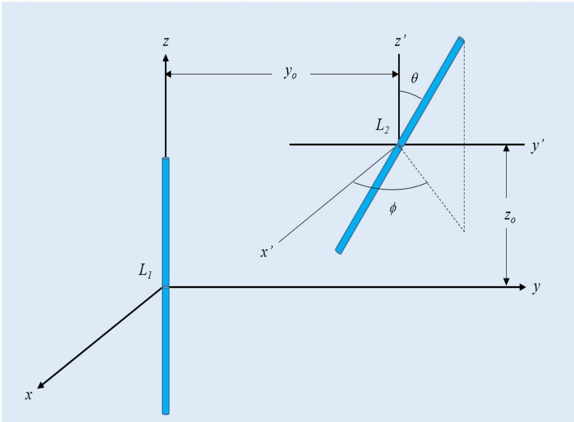

Figure 3.1: The six independent variables $L_1, L_2, y_0, z_0, \theta$ and ϕ [5].

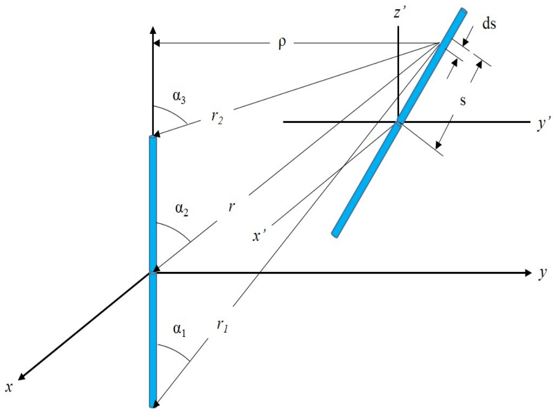

Figure 3.2: Relationships among $\alpha, \alpha_1, \alpha_2, \rho, r, r_1, r_2$ and s [5].

Given values of $L_1, L_2, y_0, z_0, \theta, \phi$ and s, the following trigonometric relations exist:

$$
\begin{aligned}
s_z &= s(\cos\theta) \\
s_y &= s(\sin\theta)(\sin\phi) \\
s_x &= s(\sin\theta)(\cos\phi) \\
\rho &= \sqrt{s_x^2 + (y_0 + s_y)^2} \\
r &= \sqrt{\rho^2 + (z_0 + s_z)^2} \\
r_1 &= \sqrt{\rho^2 + \left(z_0 + s_z + \frac{L_1}{2}\right)^2} \\
r_2 &= \sqrt{\rho^2 + \left(z_0 + s_z - \frac{L_1}{2}\right)^2}
\end{aligned}
$$

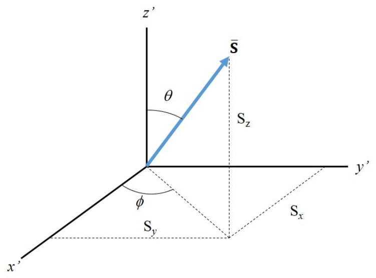

Figure 3.3: Cartesian components of the vector $\bar{\mathbf{s}}$ [5].

For the sake of brevity, the derived mathematical expression for the real (i.e. R_{21}) and imaginary (i.e. X_{21}) parts of the mutual impedance are presented in Equations (3.1) and (3.2).

$$
\begin{aligned}
R_{21} \;=\; & -30\int_{s=\frac{-L_2}{2}}^{s=\frac{L_2}{2}} \Bigg\{ \Bigg[\frac{1}{\rho^2} \Bigg([\sin(2\pi r_1)] \left[\frac{s_z + z_0 + \frac{L_1}{2}}{r_1} \right] + [\sin(2\pi r_2)] \left[\frac{s_z + z_0 - \frac{L_1}{2}}{r_2} \right] \\
& - 2[\cos(\pi L_1)][\sin(2\pi r)] \left[\frac{s_z + z_0}{r_1} \right] \Bigg) (s_x^2 + y_0 s_y^2 + s_y^2) \Bigg] \\
& + \left[\left(2\frac{(\sin(2\pi r))(\cos(2\pi L_1))}{r} - \frac{\sin(2\pi r_1)}{r_1} - \frac{\sin(2\pi r_2)}{r_2} \right) s_z \right] \Bigg\} \left\{ \frac{\sin\left[2\pi\left(\frac{L_2}{2} - |s|\right)\right]}{s} \right\} ds,
\end{aligned}
\tag{3.1}
$$

$$
\begin{aligned}
X_{21} \;=\; & -30\int_{s=\frac{-L_2}{2}}^{s=\frac{L_2}{2}} \Bigg\{ \Bigg[\frac{1}{\rho^2} \Bigg([\cos(2\pi r_1)] \left[\frac{s_z + z_0 + \frac{L_1}{2}}{r_1} \right] + [\cos(2\pi r_2)] \left[\frac{s_z + z_0 - \frac{L_1}{2}}{r_2} \right] \\
& - 2[\cos(\pi L_1)][\cos(2\pi r)] \left[\frac{s_z + z_0}{r_1} \right] \Bigg) (s_x^2 + y_0 s_y^2 + s_y^2) \Bigg] \\
& + \left[\left(2\frac{(\cos(2\pi r))(\cos(2\pi L_1))}{r} - \frac{\cos(2\pi r_1)}{r_1} - \frac{\cos(2\pi r_2)}{r_2} \right) s_z \right] \Bigg\} \left\{ \frac{\sin\left[2\pi\left(\frac{L_2}{2} - |s|\right)\right]}{s} \right\} ds.
\end{aligned}
\tag{3.2}
$$

Equations (3.1) and (3.2) contain unsolved integrals. Due to the complex nature of these two equations which are very difficult to solve analytically, the authors resorted to using digital computer to solve the equations involving integrals. The written code involves over 1000 two-address instructions which was very tedious.

Han and Myung [104] studied coplanar-skew dipoles using effective length vectors. The analysis of the mutual impedance involves getting the product of the radiated E-fields from the transmitting dipole and the receiving dipole's current distribution. The mutual impedance is then computed by taking the sum of two integrals, one along the z'-axis and another along the y'-axis. From Figure 3.4,

$$\begin{aligned} l_{2ez} &= l_2 cos(\alpha) \\ l_{2ey} &= -l_2 cos(\alpha) \end{aligned} \tag{3.3}$$

where α denotes the slant angle and l_2 denotes receiving dipole's length.

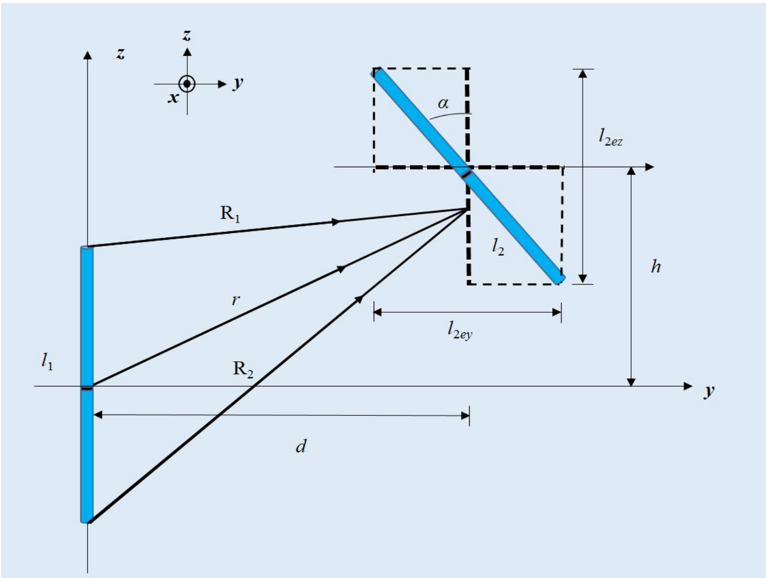

Figure 3.4: Geometry of coplanar-skew dipoles [104]. The effective length vectors method is used here.

For the sake of succintness, the derived formula for the mutual impedance is,

$$
\begin{aligned}
Z_{21} = {} & \frac{-30}{\sin\left(\frac{kl_1}{2}\right)\sin\left(\frac{kl_{2ez}}{2}\right)} \\
& \int_{h-\frac{l_{2ez}}{2}}^{h+\frac{l_{2ez}}{2}} \sin\left[k\left(-|z-h|+\frac{l_{2ez}}{2}\right)\right]\left\{\frac{-je^{-jkR_{1z}}}{R_{1z}}+\frac{-je^{-jkR_{2z}}}{R_{2z}}+j2\cos\left(\frac{kl_{2ez}}{2}\right)\frac{e^{-jkr_z}}{r_z}\right\}dz \\
& +\frac{-30}{\sin\left(\frac{kl_1}{2}\right)\sin\left(\frac{kl_{2ey}}{2}\right)} \\
& \int_{d-\frac{l_{2ey}}{2}}^{d+\frac{l_{2ey}}{2}} \sin\left[k\left(-|y-d|+\frac{l_{2ey}}{2}\right)\right]\left\{\frac{-je^{-jkR_{1y}}}{R_{1y}}+\frac{-je^{-jkR_{2y}}}{R_{2y}}-j2h\cos\left(\frac{kl_{2ey}}{2}\right)\frac{e^{-jkr_y}}{r_y}\right\}dy
\end{aligned}
\tag{3.4}
$$

where k denotes the wave number, and

$$
\begin{aligned}
r_z &= \sqrt{d^2+z^2} \\
R_{1z} &= \sqrt{d^2+\left(z-\frac{l_1}{2}\right)^2} \\
R_{2z} &= \sqrt{d^2+\left(z+\frac{l_1}{2}\right)^2}
\end{aligned}
\tag{3.5}
$$

for z-axis.

$$
\begin{aligned}
r_y &= \sqrt{h^2+y^2} \\
R_{1y} &= \sqrt{h^2+\left(y-\frac{l_1}{2}\right)^2} \\
R_{2y} &= \sqrt{h^2+\left(y+\frac{l_1}{2}\right)^2}
\end{aligned}
\tag{3.6}
$$

for y-axis.

The formulas obtained were verified to be in agreement with the simulations results from high frequency structural simulator (HFSS), which is finite element method solver for electromagnetic structures. However, this paper contains complex unsolved trigonometric and exponential integral functions which is still difficult to decipher.

3.2 Related studies with derived expressions involving nested summations.

Richmond and Geary [7] studied coplanar-skew dipoles (see Figure 3.5) using induced EMF method as a solution to obtain the mutual impedance. The goal of this paper was to derive a closed-form expression for the mutual impedance between coplanar-skew dipoles.

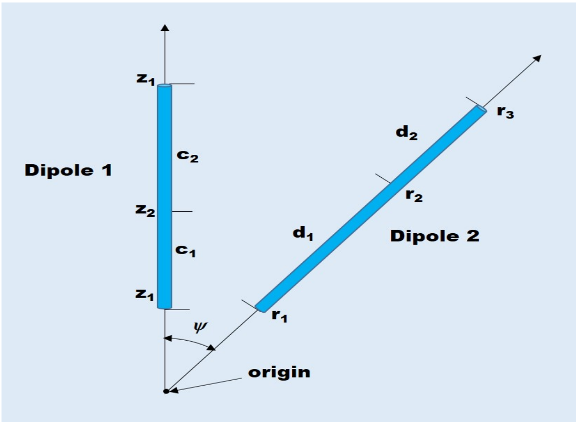

Figure 3.5: The geometry of coplanar-skew dipoles [7].

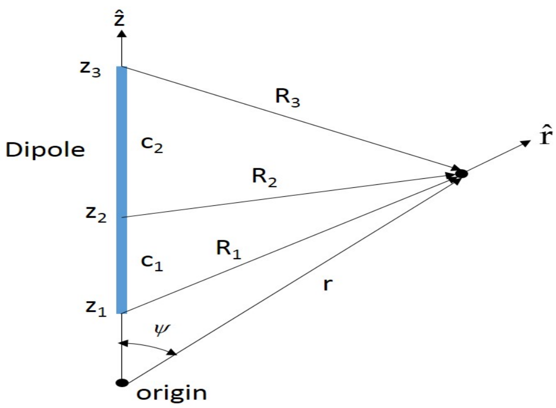

Figure 3.6: The linear dipole in cylindrical coordinate system [7].

Avoiding the rigorous derivation part, the derived closed-form formula for the mutual impedance in Figure 3.5 is

$$Z_{1,2} = -15 \sum_{m=1}^{3} \sum_{n=1}^{3} C_m D_n \sum_{p=-1}^{1} \sum_{q=-1}^{1} pq \ \exp[jk(pz_m + qr_n)] \ E(kR_{mn} + kpz_m + kqr_n) \tag{3.7}$$

where

$k = \frac{2\pi}{\lambda}$,

$p, q = -1, 1$,

R_{mn} denotes the distance from point z_m on dipole 1 to point r_m on dipole 2,

$R_{mn} = (z_m^2 + r_n^2 - 2z_m r_n \ \cos\psi)^{\frac{1}{2}}$,

$E(x) = Ci(|x|) - jSi(x)$, where

$Ci(|x|) = -\int_x^\infty \cos(x)dx/x, \qquad Si(|x|) = \int_x^\infty \sin(x)dx/x,$

$C_1 = \frac{1}{\sin(kc_1)}$

$C_2 = \frac{-\sin(kc)}{\sin(kc_1)\sin(kc_2)}$

$C_3 = \frac{1}{\sin(kd_1)}$

$D_1 = \frac{1}{\sin(kd_1)}$

$D_2 = \frac{-\sin(kd)}{\sin(kd_1)\sin(kd_2)}$

$D_3 = \frac{1}{\sin(kd_1)}$.

Other variables are also defined as follows:

ψ denotes the skew angle between the dipoles,

c, c_1 and c_2 are lengths referring to Dipole 1,

d, d_1 and d_2 are lengths referring to Dipole 2,

R_1, R_2 and R_3 are the distances defined in Figure 3.6,

z_1 and z_3 denote Dipole 1's endpoints, and z_2, the terminals shown in Figure 3.5,

r_1 and r_3 denote Dipole 2's endpoints, and r_2, the terminals shown in Figure 3.5.

The calculation of mutual impedance lies along the r-direction from the origin. The derivation process involved integration that needs an additional axis for the radial distances from the transmitting dipole and variable tranformations are also required. The derived closed-form expression in (3.7) involved complicated equations involving nested summations and exponential integration. It is only applicable to closedly spaced dipoles.

Schmidt [32] introduced an expression for mutual impedance for nonplanar skew dipoles. The type of configuration investigated is shown in Figure 3.8.

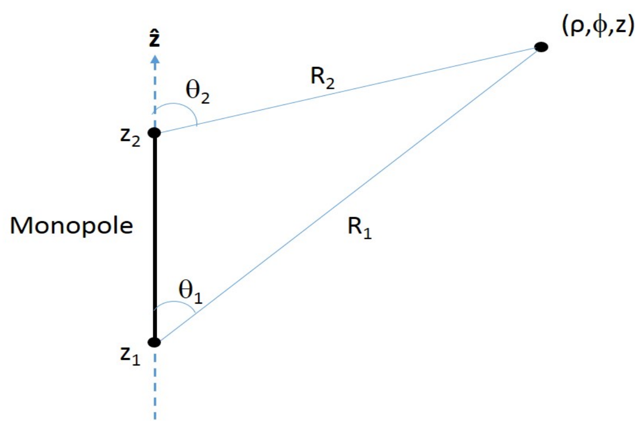

Figure 3.7: The monopole and its coordinate system .

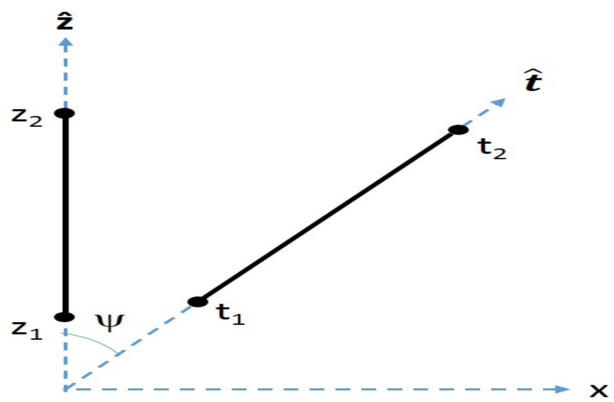

Figure 3.8: The two monopoles on z and t axes, parallel to the xz plane with distance d from each other and with skew angle ψ.

The derived mutual impedance is,

$$Z = \frac{\sqrt{\mu\epsilon}}{4\pi\epsilon}\left\{\frac{\exp(-\gamma R_{22})}{\gamma R_{22}} + \frac{1}{4\sinh(\gamma d_1)\sinh(\gamma d_2)}\sum_{s_t,s_z,s_b=\pm 1} s_t s_z \exp[\gamma(s_t t_1 + s_z z_1)]\right.$$
$$\left.\sum_{i=1,2}(-1)^i E[\gamma(R_i + s_t t + s_z z_i + j s_b \beta)]\right\} \tag{3.8}$$

where

$$\begin{aligned}
\beta &= d\,\frac{\cos(\psi) + s_z s_t}{\sin(\psi)}, \\
\gamma &= j\omega\sqrt{\mu\epsilon}, \\
d_1 &= z_2 - z_1, \\
d_2 &= t_2 - t_1,
\end{aligned}$$

Here, $s_t, s_z, s_b = \pm 1$, μ and ϵ denote permeability and permittivity, respectively. R_{22} was not defined in the article.

The derived expression involves exponential integral, $E(.)$ and nested summations which make it more complicated.

3.3 Related study with derived expressions involving unsolved integral equations and nested summations.

Han, Song, Oh and Myung [113] studied nonplanar slanted dipoles using the effective length vector. The final derived equation in (3.9) contains the characteristics for two slanted dipoles that are arbitrarily located along the $y - z$ and $y' - z'$ planes.

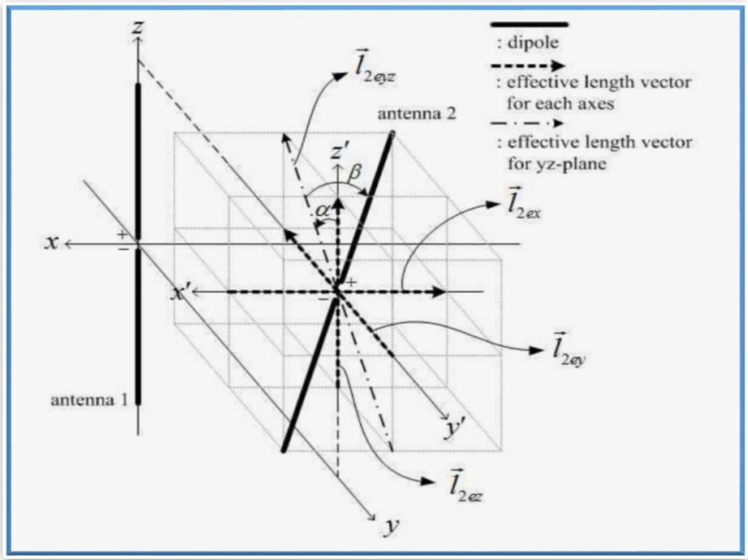

Figure 3.9: Geometry of nonplanar slanted dipoles [113].

Without the lengthy derivations,

$$
\begin{aligned}
Z_{21} &= Z_{21z} + Z_{21y} \\
&= \frac{-30}{\sin\left(\frac{kl_1}{2}\right)\sin\left(\frac{kl_{2ez}}{2}\right)} \int_{h+\frac{l_{2ez}}{2}}^{h-\frac{l_{2ez}}{2}} \sin\left[k\left(\frac{l_{2ez}}{2} - |z-h|\right)\right] \\
&\quad \left\{\frac{-je^{-jkR_1(z)}}{R_1(z)} + \frac{-je^{-jkR_2(z)}}{R_2(z)} + j2\cos\left(\frac{kl_1}{2}\right)\frac{-je^{-jkr(z)}}{r(z)}\right\} dz \\
&\quad + \frac{-30}{\sin\left(\frac{kl_1}{2}\right)\sin\left(\frac{kl_{2ey}}{2}\right)} \int_{d+\frac{l_{2ey}}{2}}^{d-\frac{l_{2ey}}{2}} \sin\left[k\left(\frac{l_{2ey}}{2} - |y-d|\right)\right] \\
&\quad \left\{\left(h-\frac{l_1}{2}\right)\frac{je^{-jkR_1(y)}}{R_1(y)} + \left(h+\frac{l_1}{2}\right)\frac{-je^{-jkR_2(y)}}{R_2(y)} + j2h\cos\left(\frac{kl_1}{2}\right)\frac{-je^{-jkr(y)}}{r(y)}\right\} \frac{dy}{y}
\end{aligned}
\tag{3.9}
$$

where

$$
\begin{aligned}
r(z) &= \sqrt{d^2+z^2}, & r(y) &= \sqrt{h^2+y^2} \\
R_1(z) &= \sqrt{d^2+(z-l_1/2)^2}, & R_1(z) &= \sqrt{(h-l_1/2)^2+y^2} \\
R_2(z) &= \sqrt{d^2+(z+l_1/2)^2}, & R_2(y) &= \sqrt{(h+l_1/2)^2+y^2}.
\end{aligned}
$$

In order to facilitate mathematical integration, the Z_{21z} and Z_{21y} terms in (3.9) which involve integration can be transformed into nested summations resulting to Equations (3.10) and (3.11), respectively. Although, the sine and cosine integrals are still inside the summation symbols.

$$
\begin{aligned}
&Z_{21z} = \frac{-30}{\sin\left(\frac{kl_1}{2}\right)\sin\left(\frac{kl_{2ez}}{2}\right)} \\
&\left[\left\{1+2\cos\left(\frac{kl_1}{2}\right)\right\}\delta_t - 1\right] \cdot \\
&\frac{1}{2}\sum_{t=-1}^{1}\sum_{n=-1}^{1}\sum_{s=0}^{1}\left[\cos(kq_{n,t})\left\{ci\left(k\sqrt{d^2+q_{n,t}^2}+(-1)^s kq_{n,t}\right) - ci\left(k\sqrt{d^2+q_{0,t}^2}+(-1)^s kq_{0,t}\right)\right\}\right. \\
&\left.+(-1)^s\sin(kq_{n,t})\left\{si\left(k\sqrt{d^2+q_{n,t}^2}+(-1)^s kq_{n,t}\right) - si\left(k\sqrt{d^2+q_{0,t}^2}+(-1)^s kq_{0,t}\right)\right\}\right] \\
&\left[\left\{1+2\cos\left(\frac{kl_1}{2}\right)\right\}\delta_t - 1\right] \cdot \\
&-j\frac{1}{2}\sum_{t=-1}^{1}\sum_{n=-1}^{1}\sum_{s=0}^{1}\left[\cos(kq_{n,t})\left\{si\left(k\sqrt{d^2+q_{n,t}^2}+(-1)^s kq_{n,t}\right) - si\left(k\sqrt{d^2+q_{0,t}^2}+(-1)^s kq_{0,t}\right)\right\}\right. \\
&\left.-(-1)^s\sin(kq_{n,t})\left\{ci\left(k\sqrt{d^2+q_{n,t}^2}+(-1)^s kq_{n,t}\right) - ci\left(k\sqrt{d^2+q_{0,t}^2}+(-1)^s kq_{0,t}\right)\right\}\right]
\end{aligned}
\tag{3.10}
$$

where δ_t denotes the Kronecker's delta function, and $q_{n,t} = h + n\frac{l_{2ez}}{2} + t\frac{l_1}{2}$.

$$
\begin{aligned}
Z_{21y} = {} & \frac{-30}{\sin\left(\frac{kl_1}{2}\right)\sin\left(\frac{kl_{2ey}}{2}\right)} \\
& \left\{-1+\left[1+2\cos\left(\frac{kl_1}{2}\right)\right]\delta_t\right\}\times \\
& \frac{1}{2}\sum_{t=-1}^{1}\sum_{m=-1}^{1}\sum_{u=0}^{1}\sum_{s=0}^{1}\Bigg\{(-1)^u(-1)^s\cos\left(kp_{m,0}+(-1)^u(-1)^s kq_{0,t}\right) \\
& \left[ci\left(k\sqrt{q_{0,t}^2+p_{m,0}^2}+(-1)^u kp_{m,0}+(-1)^s kq_{0,t}\right)-ci\left(k\sqrt{q_{0,t}^2+p_{0,0}^2}+(-1)^u kp_{0,0}+(-1)^s kq_{0,t}\right)\right] \\
& +(-1)^s\sin\left(kp_{m,0}+(-1)^u(-1)^s kq_{0,t}\right)\Bigg[si\left(k\sqrt{q_{0,t}^2+p_{m,0}^2}+(-1)^u kp_{m,0}+(-1)^s kq_{0,t}\right) \\
& -si\left(k\sqrt{q_{0,t}^2+p_{0,0}^2}+(-1)^u kp_{0,0}+(-1)^s kq_{0,t}\right)\Bigg]\Bigg\} \\
& \left\{-1+\left[1+2\cos\left(\frac{kl_1}{2}\right)\right]\delta_t\right\}\times \\
& +j\sum_{t=-1}^{1}\sum_{m=-1}^{1}\sum_{u=0}^{1}\sum_{s=0}^{1}\Bigg\{(-1)^u(-1)^s\cos\left(kp_{m,0}+(-1)^u(-1)^s kq_{0,t}\right) \\
& \left[si\left(k\sqrt{q_{0,t}^2+p_{m,0}^2}+(-1)^u kp_{m,0}+(-1)^s kq_{0,t}\right)-si\left(k\sqrt{q_{0,t}^2+p_{0,0}^2}+(-1)^u kp_{0,0}+(-1)^s kq_{0,t}\right)\right] \\
& +(-1)^s\sin\left(kp_{m,0}+(-1)^u(-1)^s kq_{0,t}\right)\Bigg[ci\left(k\sqrt{q_{0,t}^2+p_{m,0}^2}+(-1)^u kp_{m,0}+(-1)^s kq_{0,t}\right) \\
& -ci\left(k\sqrt{q_{0,t}^2+p_{0,0}^2}+(-1)^u kp_{0,0}+(-1)^s kq_{0,t}\right)\Bigg]\Bigg\}
\end{aligned} \tag{3.11}
$$

where $p_{m,t} = d + m\frac{l_{2ey}}{2} + t\frac{l_1}{2}$.

The obtained equations here are all complicated involving unsolved integration in Equation (3.9) and nested summations in Equations (3.10) and (3.11).

Summary

This chapter presented related studies which clearly established the very reason why this dissertation is quite significant. The analyses introduced very intricate and intractable expressions and difficult to understand derivations. Some of the papers derived equations using analytical methods first and then verified their results through computer electromagnetics simulation software. Conversely, this dissertation will first use method of moments based antenna simulation software to obtain the numerical values of the mutual impedance, then obtain phenomenologically the expressions which model the obtained mutual impedance from VLab.

Chapter 4

Research Methodology

Introduction

For the investigation on the skewed crossed dipoles, the research process in Figure 4.1 will be carried out. Each of the flow chart's block is discussed in the succeeding subsections.

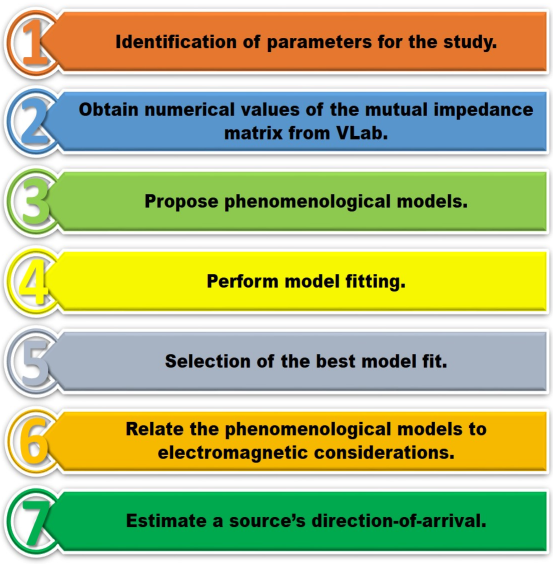

Figure 4.1: The step-by-step research process of the dissertation.

4.1 Identification of parameters for the study.

The crossed dipoles configuration in Figure 4.2 is the basis of this dissertation.

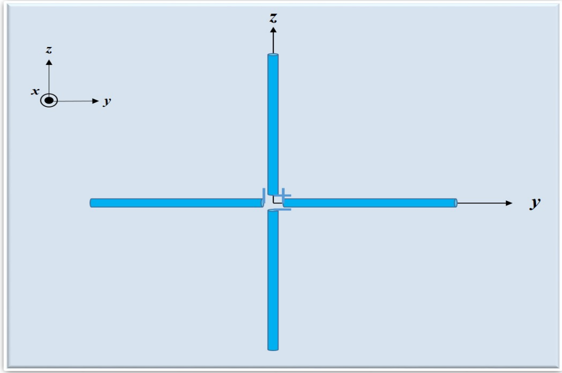

Figure 4.2: The coplanar and cocentered crossed dipoles. Here, there is no mutual coupling.

If the horizontal dipole is moved at a perpendicular distance as in Figure 4.3, as long as the orthogonality between the dipoles is maintained, then there will be no mutual coupling.

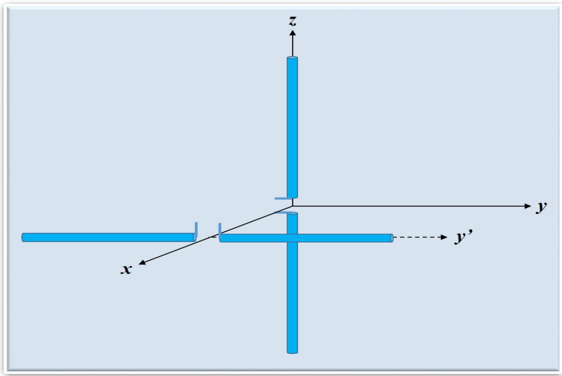

Figure 4.3: The nonplanar and cocentered crossed dipoles. Here, still there is no mutual coupling.

Now, given the scenario in Figure 4.4, the horizontal dipole will now be skewed, then there will be mutual coupling.

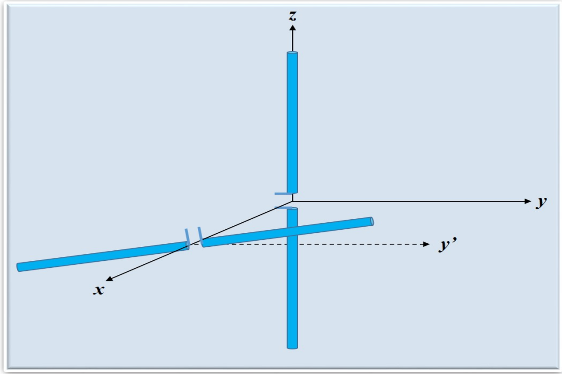

Figure 4.4: The skewed nonplanar and cocentered crossed dipoles. Here, there is now mutual coupling.

Consider a center-fed dipole with length L, named as Dipole 1, located along the z-axis and its feedpoint centered at the origin (See Figure 4.5). Another center-fed dipole with length L, named as Dipole 2, with its feedpoint centered along the x-axis, is located in the $y' - z'$ plane and skewed at an angle φ.

In order to make the results independent of frequency, L and Δ will be in terms of wavelengths. The three independent variables, namely, the dipoles' length L, the skew angle φ, and the inter-dipole separation, Δ will be varied in the simulation. The phenomenological models, therefore, are expected to be functions of the trivariate $\left(\frac{L}{\lambda}, \varphi, \frac{\Delta}{\lambda}\right)$.

4.2 Obtain numerical values of the mutual impedance matrix from VLab

VLab has "Pre-processing" and "Post-processing" stages. In the pre-processing stage, there are three modes to undergo before computing the mutual impedance. These modes are the "Geometry Mode", "Model Mode" and "Mesh Mode".

In the "Geometry Mode" the skewed crossed dipoles are constructed. The screen-shot of the geometry view in VLab is shown in Figure 4.6.

Assigning physical parameters is done in the "Model Mode". In model mode, cables based on curves structure are created and feed segment is defined. Here, the operating frequency of the antenna array and the calculation parameters (i.e.

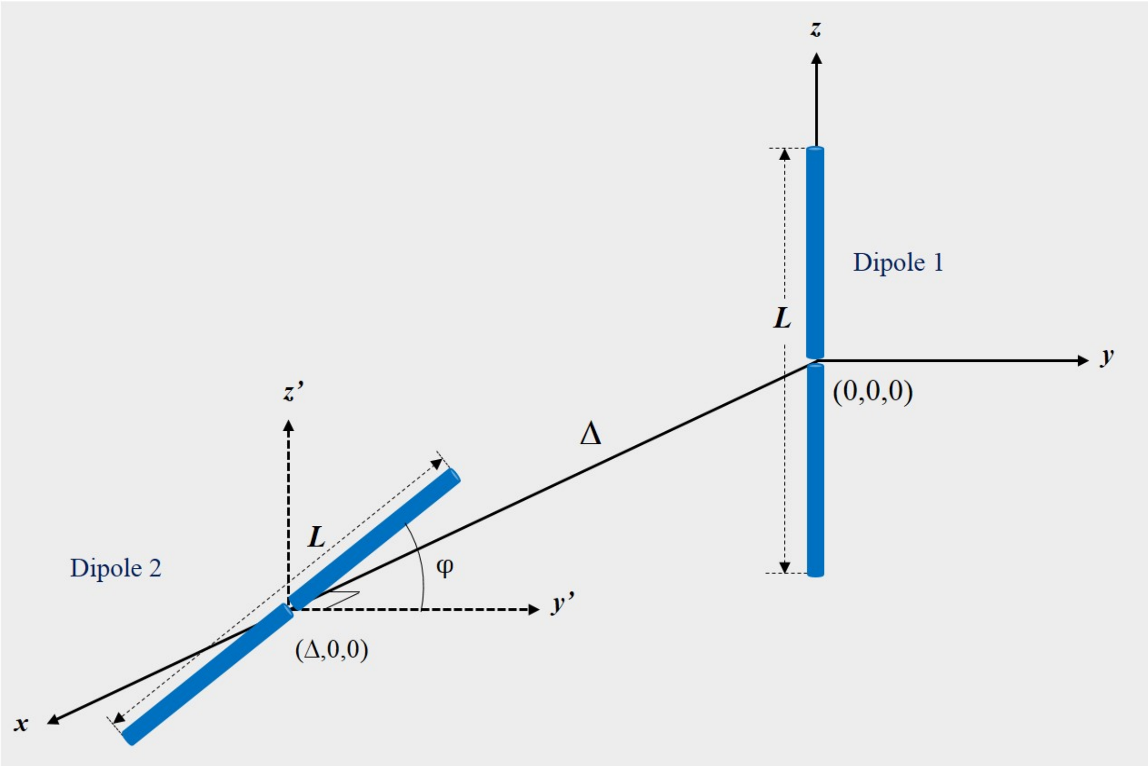

Figure 4.5: The geometry of the skewed crossed dipoles under study. The independent variables are: the dipoles' common length L, the skew angle φ, and the inter-dipole separation Δ.

Impedance, Z) are set, and the size of segmentation can be manually indicated. Dipole feed segment's termination device is also created in the model mode. The model view is shown in Figure 4.7.

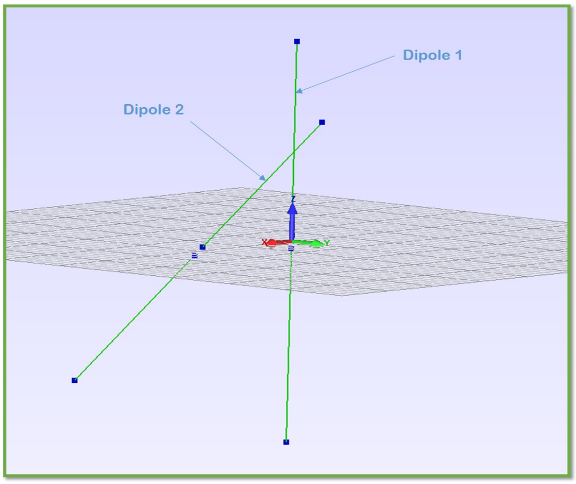

Figure 4.6: Geometry view of the skewed crossed dipoles in VLab. Here, the skewed crossed dipoles is constructed based on set variables.

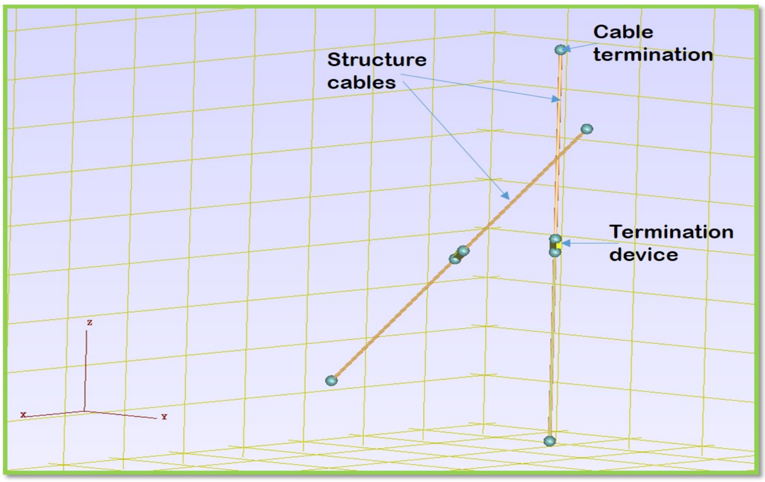

Figure 4.7: Model view of the skewed crossed dipoles in VLab. Cables definition based on curves structure and devices modeling is set here.

Discretization of obtained model (i.e. from the Model mode not the phenomenological model) for calculation is done in the "Mesh Mode". The wire segments and their segmentation size that were defined in model mode will be generated in the mesh mode. Ports for measurement must be created in order to generate an output.

The result of the calculation or output is part of the post-processing stage. Viewing and extraction of data for analyzing the results is done on this stage. The mesh view is shown in Figure 4.8.

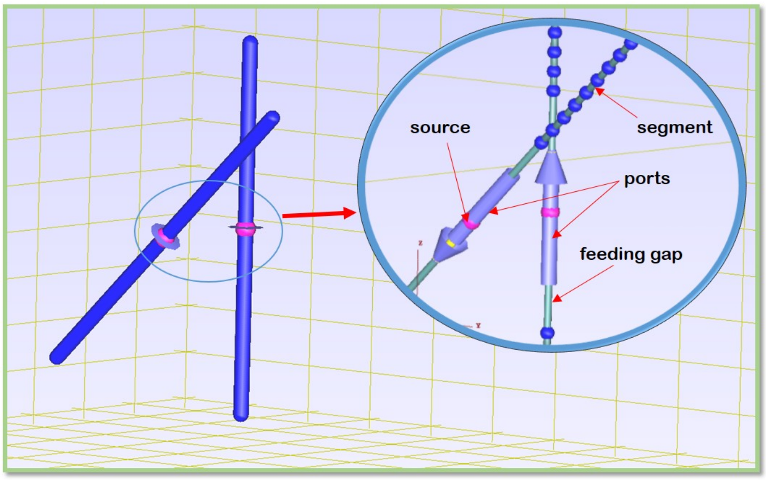

Figure 4.8: Mesh view of the skewed crossed dipoles in VLab. Model conversion to discrete elements (i.e. wire segments) for calculation is done on mesh mode.

All throughout the simulations: each dipole's diameter is maintained at 0.02λ millimeters; each dipole's feeding gap equals $\frac{\lambda}{50}$; and the voltage source's internal impedance is always matched to a half-wavelength dipole, regardless of the actual value of $\frac{L}{\lambda}$. The dipoles, placed in free-space, will be center-fed with a 1-V source and a 50-ohm load impedance.

The skewed dipole-pair were simulated at these values:

1) a skewed angle $\varphi \in \{1°, 45°\}$,

2) each dipole's electric length $\frac{L}{\lambda} \in \{0.1, 1.0\}$,

3) spatial separation between the two dipoles' feeding center $\frac{\Delta}{\lambda} \in \{0.01, 2.0\}$.

For each combination of $(\frac{L}{\lambda}, \varphi, \frac{\Delta}{\lambda})$, the mutual impedance value will be computed.

The mutual impedance matrix to be used in the DOA estimation will be of the form,

$$\mathbf{Z} = \begin{bmatrix} Z_{1,1} & Z_{1,2} \\ Z_{2,1} & Z_{2,2} \end{bmatrix}$$

.

For a skewed crossed dipoles configuration, $Z_{1,2} = Z_{2,1}$ and $Z_{1,1} = Z_{2,2}$, which follows a bisymmetric matrix.

Choice of Real-Value Entities to be Model-Fit

To be model-fit are the real-value entities: $|Z_{1,2}|$, $\angle Z_{1,2}$, $|Z_{2,1}|$, $\angle Z_{2,1}$, $|Z_{1,1}|$, $\angle Z_{1,1}$, $|Z_{2,2}|$, $\angle Z_{2,2}$. $|\cdot|$ and $\angle\cdot$ denote the magnitude and phase of the complex-value entity, respectively.

4.3 Proposed phenomenological models

At this stage, the functions that model the mutual impedance from the VLab data will be proposed. Various candidate models will be model-fit. All possible perspectives of the trivariate function (i.e. $f\left\{\frac{L}{\lambda}, \varphi, \frac{\Delta}{\lambda}\right\}$) for each real value entity will be plotted and carefully observed.

4.4 Perform model fitting

The model fitting can be summarized into three major steps.

1. **Form the objective function.**

   In general,

$$SSE = \sum_{n=1}^{N} \left| Z_n - \hat{Z}_n \right|^2, \tag{4.1}$$

   where SSE denotes the "sum-of-squares error", which measures how far the data are from the model's predicted values. Z denotes the impedance value from VLab, $\hat{Z}$ denotes the estimated impedance predicted by the model and N denotes the number of observations.

   The sum-of-squares error (SSE) will be the error function to be minimized.

2. **Find the unknown parameters to be optimized.**

   Symbolically,

$$\{c_1, c_2, ..., c_q\} = \arg\min_{c} \sum_{n=1}^{N} \left| Z_n - \hat{Z}_n \right|^2, \tag{4.2}$$

   where $c_1, c_2, ..., c_q$ are the unknown parameters, and q denotes the number of parameters to be optimized.

3. **Test the goodness-of-fit.**

To determine if the model fitting is good, the "coefficient of determination", R^2, will be used. R^2 can be computed as,

$$R^2 = 1 - \frac{SSE}{SST}, \tag{4.3}$$

where SST denotes the sum-of-squares-total, which measures how far the data are from the mean. Symbolically,

$$SST = \sum_{n=1}^{N} \left| Z_n - \bar{Z} \right|^2, \tag{4.4}$$

where

$$\bar{Z} = \sum_{n=1}^{N} Z_n, \tag{4.5}$$

and $\bar{Z}$ denotes the mean of the VLab data.

R^2, which is a value between 0 and 1, measures how successful the fit is in explaining the variation between the VLab's data and the proposed model's data. An R^2 value of 0 means that the proposed model explains none of the variability. While, R^2 value of 1 means the model is a perfect fit or the model explains all variability in the VLab's data. The higher the R^2, the better is the model fitting.

A MATLAB code will be written for this purpose. The code will perform four-dimensional model fitting, e.g. $|Z_{1,2}|$, $\frac{L}{\lambda}$, φ, and $\frac{\Delta}{\lambda}$, to generate the optimized parameters and the corresponding R^2.

4.5 Selection of the best model fit

The criteria for choosing the best model will be: (1) whichever model that gives the highest value of R^2, and (2) whichever model that has fewer number of the degrees of freedom in the model. The selected model must return the estimated data sets as close as those from VLab. Just as important as the two criteria, the models should also conform with the existing electromagnetic theories and principles.

4.6 Relate the phenomenological models to electromagnetic considerations

Having chosen the best model for each real value entity, the results should conform to existing electromagnetic concepts. Not only that the resulting phenomenological models relate to existing electromagnetic principles. Since this dissertation pioneers phenomenological modeling of the mutual impedance of the mutual coupling, it is also aimed that new insights be introduced. At this stage, results are backed-up with pertinent graphs and illustrations in order to give clearer understanding of the concepts being discussed.

4.7 Estimate a source's direction-of-arrival

To show the usefulness of the proposed phenomenological models, direction-of-arrival estimation will be performed. On this stage, the validation whether the modeling is successful or not will be determined.

Summary

The research process that this dissertation will carry out has been established. This phenomenological method considers getting first the numerical values of mutual impedance and then model fit these VLab data to simple expressions. The criteria for selecting the best model fit have also been set. The results and analysis will be presented in the next chapter.

Chapter 5

Data, Results and Analyses

Introduction

At this point, the simulations' results from VLab and the proposed phenomenological models for the cross-impedance and self-impedance are now presented. The analysis part is based on existing electromagnetic principles and considerations.

5.1 Simulation Results from VLab

Since we are dealing with four variables and showing 4D plots will be difficult, the phenomenological expressions are proposed based on the following three perspectives: (1) $|Z|$ or $\angle Z$ vs. $\{\frac{\Delta}{\lambda}, \varphi\}$ for a given $\frac{L}{\lambda}$, (2) $|Z|$ or $\angle Z$ vs. $\{\frac{\Delta}{\lambda}, \frac{L}{\lambda}\}$ for a given φ, and (3) $|Z|$ or $\angle Z$ vs. $\{\varphi, \frac{L}{\lambda}\}$ for a given $\frac{\Delta}{\lambda}$. Figures 5.1 - 5.6 are sample plots from VLab. By carefully observing the behavior of the plots in three perspectives, several models for each of the dependent variables (i.e. $|Z_{1,2}| = |Z_{2,1}|$, $\angle Z_{1,2} = \angle Z_{2,1}$ $|Z_{1,1}| = |Z_{2,2}|$ and $\angle Z_{1,1} = \angle Z_{2,2}$) are proposed.

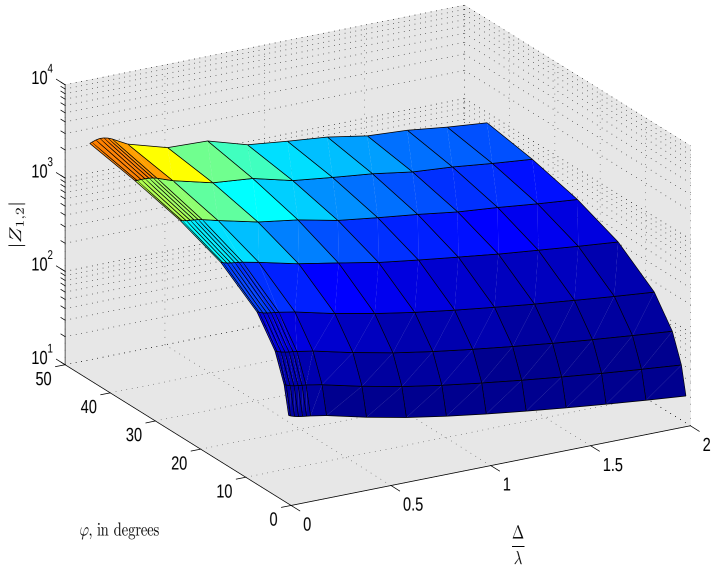

Figure 5.1: The 3D plot of $|Z_{1,2}|$ at $\frac{L}{\lambda} = 1.00$, $\forall\{\frac{\Delta}{\lambda}, \varphi\}$ from VLab. Here, $|Z_{1,2}|$ increases with increasing φ, and $|Z_{1,2}|$ decreases with increasing $\frac{\Delta}{\lambda}$.

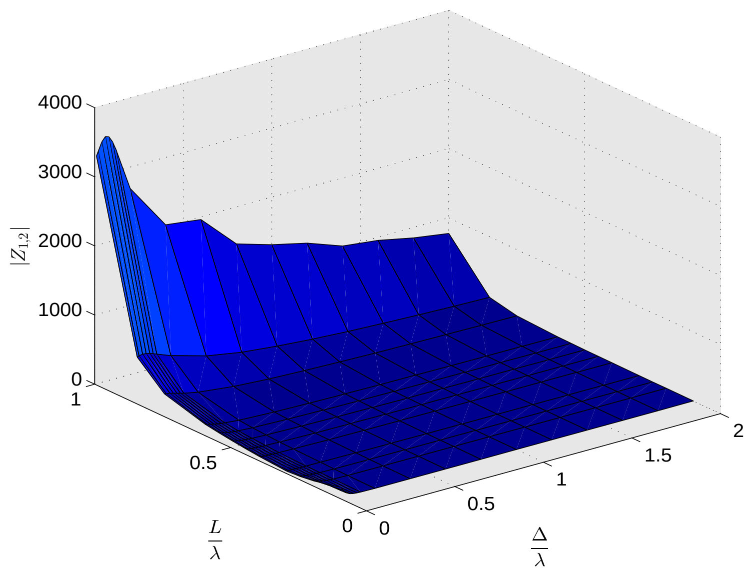

Figure 5.2: The 3D plot of $|Z_{1,2}|$ at $\varphi = 45°$, $\forall\{\frac{\Delta}{\lambda}, \frac{L}{\lambda}\}$ from VLab. $|Z_{1,2}|$ also increases with increasing $\frac{L}{\lambda}$.

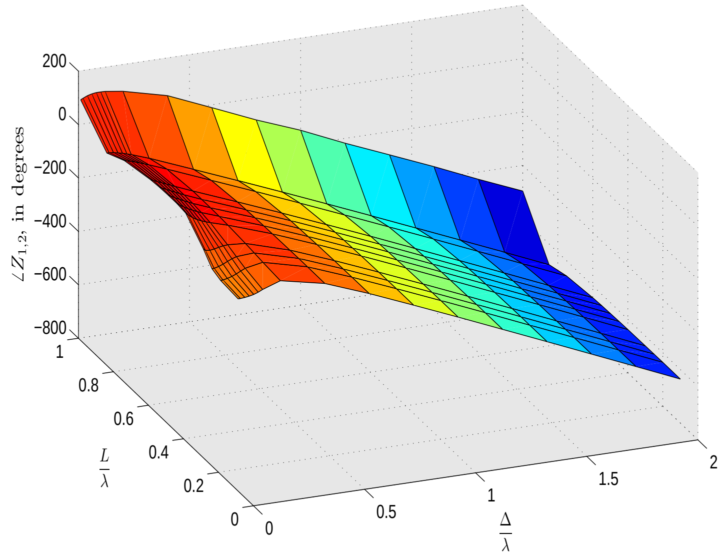

Figure 5.3: The 3D plot of the unwrapped $\angle Z_{1,2}$ at $\varphi = 45°$, $\forall\{\frac{\Delta}{\lambda}, \frac{L}{\lambda}\}$ from VLab. The $\angle Z_{1,2}$ is almost linear with $\frac{\Delta}{\lambda}$ and $\frac{L}{\lambda}$. $\angle Z_{1,2}$ is also independent of the skew angle φ.

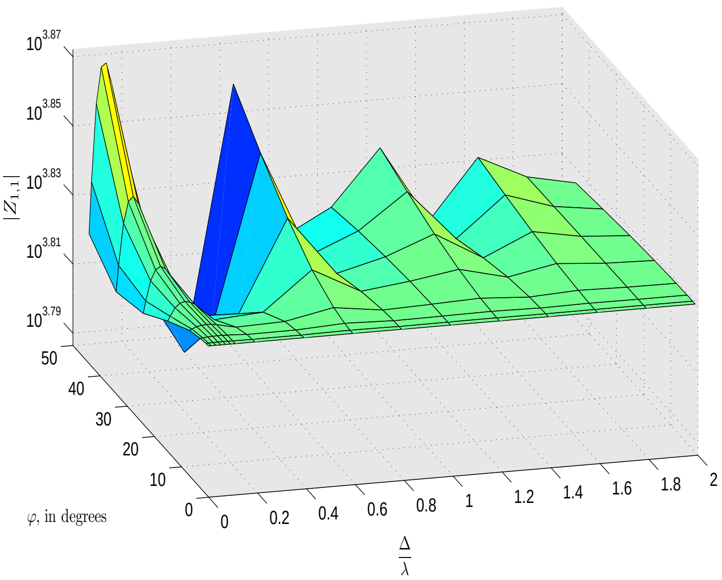

Figure 5.4: The 3D plot of $|Z_{1,1}|$ at $\frac{L}{\lambda} = 1.00$, $\forall\{\frac{\Delta}{\lambda}, \varphi\}$ from VLab. The behavior of $|Z_{1,1}|$ with respect to $\frac{\Delta}{\lambda}$ is like a dampened sinusoid.

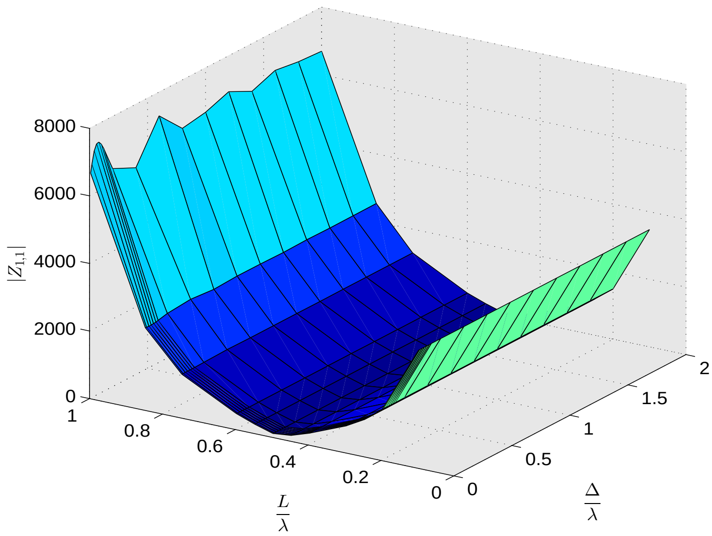

Figure 5.5: The 3D plot of $|Z_{1,1}|$ at $\varphi = 45°$, $\forall\{\frac{\Delta}{\lambda}, \frac{L}{\lambda}\}$ from VLab. The minumum value of $|Z_{1,1}|$ is near $\frac{L}{\lambda} = 0.50$.

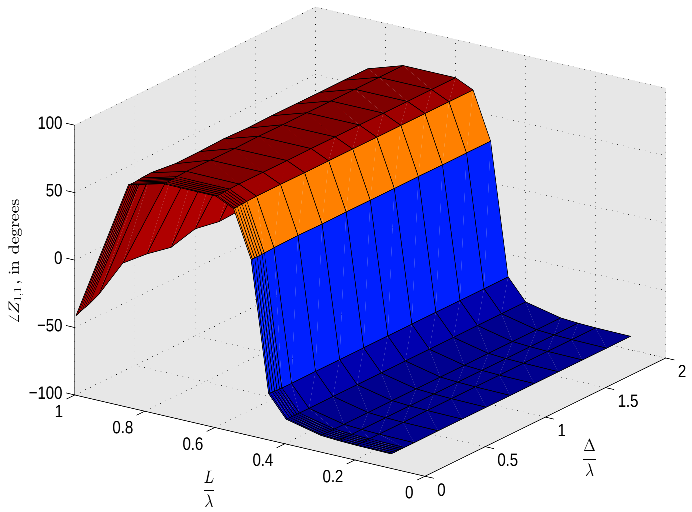

Figure 5.6: The 3D plot of $\angle Z_{1,1}$ at $\varphi = 45°$, $\forall\{\frac{\Delta}{\lambda}, \frac{L}{\lambda}\}$ from VLab. The data for $\angle Z_{1,1}$ shows a sinuoidal relationship with $\frac{L}{\lambda}$.

5.2 Model Fitting of the Mutual Impedances, $Z_{1,2}$ and $Z_{2,1}$

This section shows how the phenomenological models for $Z_{1,2}$ and $Z_{2,1}$ are obtained. These phenomenological models will then be related to electromagnetic considerations at the end part of each subsection.

In all the VLab simulations, $Z_{1,2} = Z_{2,1}$, $\forall\{\frac{\Delta}{\lambda}, \frac{L}{\lambda}, \varphi\}$. Consequently, $|Z_{1,2}| = |Z_{2,1}|$ and $\angle Z_{1,2} = \angle Z_{2,1}$.

5.2.1 Magnitude of $Z_{1,2}$ and $Z_{2,1}$

Note that all candidate models are presented in Appendix A. The best model is

$$|Z_{1,2}| \;=\; |Z_{2,1}| \;\approx\; 10^{a_1} \left(\frac{\Delta}{\lambda}\right)^{-a_2} \left(\frac{L}{\lambda}\right)^{a_3} |\sin(\varphi)|\,, \tag{5.1}$$

where

$$a_1 := 2.3018,$$
$$a_2 := 0.5564,$$
$$a_3 := 2.6230.$$

The goodness-of-fit R^2 equals 0.86 for (5.1), i.e. only 14% of the VLab numerical data cannot be explained by the above model.

The R^2 is evaluated on

$$\begin{aligned} \log_{10}|Z_{1,2}| &= \log_{10}|Z_{2,1}| \\ &\approx a_1 - a_2 \log_{10}\left|\frac{\Delta}{\lambda}\right| + a_3 \log_{10}\left|\frac{L}{\lambda}\right| + \log_{10}|\sin(\varphi)| \end{aligned} \tag{5.2}$$

instead of (5.1). This is because $|Z_{1,2}| = |Z_{2,1}|$ has values over several orders of magnitude. Hence, the latter would overweight those support regions of $\left\{\varphi, \frac{L}{\lambda}, \frac{\Delta}{\lambda}\right\}$ where $|Z_{1,2}| = |Z_{2,1}|$ is very large, thereby poorly fitting other regions of $\left\{\varphi, \frac{L}{\lambda}, \frac{\Delta}{\lambda}\right\}$ where $|Z_{1,2}| = |Z_{2,1}|$ is small. Specifically, the would-be-underweighted support region is where $\frac{L}{\lambda}$ increases toward unity and where $\frac{\Delta}{\lambda}$ decreases toward zero.

$|Z_{1,2}|$ relies on length of the dipoles, on the separation between the dipoles and on the skew angle.

The negative power of $\frac{\Delta}{\lambda}$ in the above phenomenological model suggests that $|Z_{1,2}| = |Z_{2,1}|$ decreases monotonically with an increasing inter-dipole separation $\frac{\Delta}{\lambda}$. Indeed, as As $\frac{\Delta}{\lambda} \to \infty$, the model gives $|Z_{1,2}| = |Z_{2,1}| \to 0$. These trends are reasonable in terms of electromagnetics, because $Z_{1,2} = Z_{2,1}$ is proportional to the induced electric field, whose magnitude is inversely related to the distance between the driving dipole and the induced dipole.

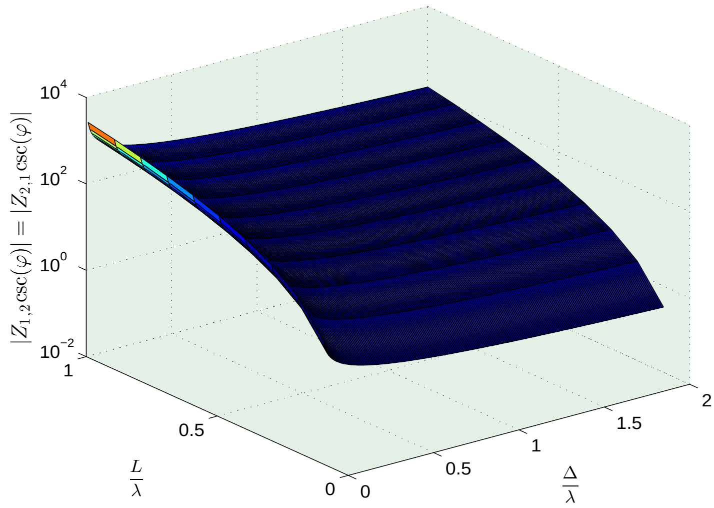

Figure 5.7: How $|Z_{1,2}\csc(\varphi)| = |Z_{2,1}\csc(\varphi)|$ of (5.1) varies with $\frac{\Delta}{\lambda}$ and $\frac{L}{\lambda}$.

The non-negative factor, $|\sin\varphi|$, in the model of (5.1) suggests that $|Z_{1,2}| = |Z_{2,1}|$ would increase monotonically, as the two dipoles become less perpendicular. This is reasonable in terms of electromagnetics, because as the skew angle $|\varphi|$ increases from 0 toward 90°, the two dipoles would become more parallel, hence more mutual coupling between these two skewed dipoles. This $|\sin\varphi|$ factor arises from the projection of the driving dipole's electric field on the induced dipole, which is skewed from the former dipole by a rotational angle of φ. Under the special case where the two dipoles are perfectly orthogonal (i.e. $\varphi = 0$), $|Z_{1,2}| = |Z_{2,1}| = 0$ in (5.1), as expected.

As the dipole gets longer, the electromagnetic field along each dipole gets larger. This will in turn produce more current and therefore the dipoles would radiate greater amount of power. Consequently, as clearly indicated in (5.1) , $|Z_{1,2}|$ exponentially increases with $\frac{L}{\lambda}$. Figure 5.7 agrees with the above claim.

5.2.2 Phase of $Z_{1,2}$ and $Z_{2,1}$

The candidate models for $\angle Z_{1,2} = \angle Z_{2,1}$ are presented in Appendix B. The best phenomenological model fit for the $\angle Z_{1,2}$ and $\angle Z_{2,1}$ is

$$\begin{aligned} \angle Z_{1,2} &= \angle Z_{2,1} \\ &\approx b_1 \frac{\Delta}{\lambda} + b_2 \frac{L}{\lambda} + b_3, \end{aligned} \tag{5.3}$$

where

$$\begin{aligned} b_1 &:= -5.5920 = -1.78\pi, \\ b_2 &:= 0.5048\pi, \\ b_3 &:= -0.2952 = -0.0940\pi. \end{aligned}$$

The goodness-of-fit R^2 equals 0.96, i.e. only 4% of the VLab numerical data cannot be explained by the above model.

This model of $\angle Z_{1,2} = \angle Z_{2,1}$ is independent of the inter-dipole skew angle φ. This is reasonable in terms of electromagnetics: The phase $\angle Z_{1,2} = \angle Z_{2,1}$ depends on the electric field at the induced dipole. If the induced dipole is rotated with respect to its feed center, that electric field's phase would remain the same. Hence, the inter-dipole skew angle φ has no effect on $\angle Z_{1,2}$.

This model of $\angle Z_{1,2} = \angle Z_{2,1}$ varies linearly with the inter-dipole separation $\frac{\Delta}{\lambda}$. This is reasonable in terms of electromagnetics: As the radiation propagates outward from the driving dipole, its phase would change linearly with the distance traversed. This model of $\angle Z_{1,2} = \angle Z_{2,1}$ increases linearly with the dipoles' electric length $\frac{L}{\lambda}$. This is reasonable in terms of electromagnetics: The radiation is emitted from driving dipole along that dipole's entire length, and is received by the induced dipole along the induced dipole's entire length. The average of such distances increases linearly with the two dipoles' length. Hence, the phase would change also linearly with $\frac{L}{\lambda}$. Figure 5.8 shows the 3D plot of the model in (5.3).

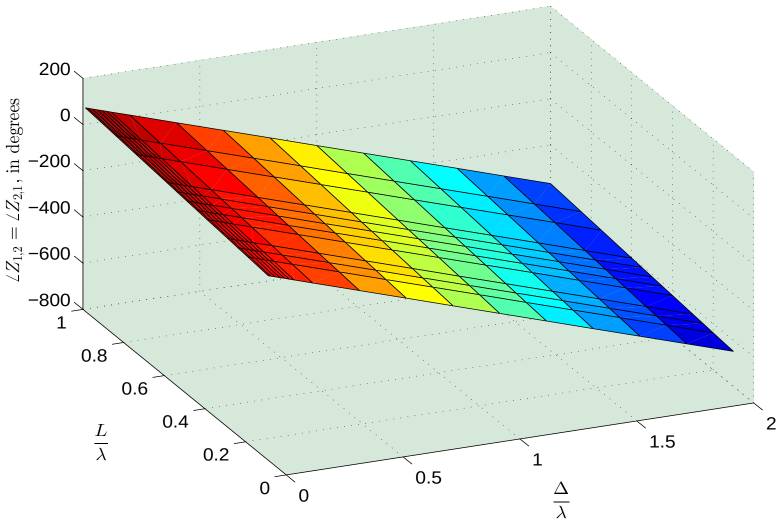

Figure 5.8: How $\angle Z_{1,2} = \angle Z_{2,1}$ of (5.3) varies with $\frac{\Delta}{\lambda}$ and $\frac{L}{\lambda}$. The $\angle Z_{1,2} = \angle Z_{2,1}$ varies linearly with $\frac{\Delta}{\lambda}$ and $\frac{L}{\lambda}$.

5.3 Model Fitting of the Self-Impedances, $Z_{1,1}$ and $Z_{2,2}$

This section shows how the phenomenological models for $Z_{1,1}$ and $Z_{2,2}$ are obtained. The analysis of the obtained phenomenological models will be based on existing theories and principles of antenna electromagnetics at the end part of each subsection.

In all the VLab simulations, $Z_{1,1} = Z_{2,2}$, $\forall\{\frac{\Delta}{\lambda}, \frac{L}{\lambda}, \varphi\}$. Hence, $|Z_{1,1}| = |Z_{2,2}|$ and $\angle Z_{1,1} = \angle Z_{2,2}$.

5.3.1 Magnitude of $Z_{1,1}$ and $Z_{2,2}$

All candidate models are shown in Appendix C. The best-fitting phenomenological model is

$$\begin{aligned}
|Z_{1,1}| &= |Z_{2,2}| \\
&\approx \overbrace{\left| p_1 + p_2 \overbrace{\cos\left(p_3 \frac{\Delta}{\lambda} + p_4\right) e^{-p_5 \frac{\Delta}{\lambda}}}^{P_2\left(\frac{\Delta}{\lambda}\right) :=} \sin^2(\varphi) \right|}^{P_1\left(\frac{\Delta}{\lambda}, \varphi\right) :=} \\
&\quad \overbrace{\left[\left(\frac{L}{\lambda} - p_6\right)^2 + p_7\right]}^{P_3\left(\frac{L}{\lambda}\right) :=}. \qquad (5.4)
\end{aligned}$$

where

$$\begin{aligned}
p_1 &:= 20415.4041, \\
p_2 &:= 98.3895, \\
p_3 &:= 4.0412\pi, \\
p_4 &:= 3.4539\pi, \\
p_5 &:= 0.2782, \\
p_6 &:= 0.4838, \\
p_7 &:= 0.0057.
\end{aligned}$$

The goodness-of-fit R^2 equals 0.98, i.e. only 2% of the VLab's numerical data cannot be explained by the above model.

The R^2 is evaluated on

$$\begin{aligned}\log_{10}|Z_{1,1}| &= \log_{10}|Z_{2,2}| \\ &\approx \log_{10}\left|p_1 + p_2\cos\left(p_3\frac{\Delta}{\lambda} + p_4\right)\ e^{-p_5\frac{\Delta}{\lambda}}\ \sin^2(\varphi)\right| \\ &\quad + \log_{10}\left|\left(\frac{L}{\lambda} - p_6\right)^2 + p_7\right|. \end{aligned} \tag{5.5}$$

instead of (5.4). This is because $|Z_{1,1}| = |Z_{2,2}|$ takes on values over several orders of magnitude. Hence, any R^2 computation based on (5.4) would overweight those support subregions of $\left\{\varphi, \frac{L}{\lambda}, \frac{\Delta}{\lambda}\right\}$ where $|Z_{1,1}| = |Z_{2,2}|$ is very large, thereby poorly fitting other regions of $\left\{\varphi, \frac{L}{\lambda}, \frac{\Delta}{\lambda}\right\}$ where $|Z_{1,1}| = |Z_{2,2}|$ is small. More explicitly, the would-be-overweighted region is where $\frac{L}{\lambda}$ increases toward unity and where $\frac{\Delta}{\lambda}$ decreases toward zero.

The two dipoles' separation $\frac{\Delta}{\lambda}$ affects $|Z_{1,1}| = |Z_{2,2}|$ only through $P_1\left(\frac{\Delta}{\lambda}, \varphi\right)$. If and only if the two dipoles are very far apart (i.e. as $\frac{\Delta}{\lambda} \to \infty$): $P_1\left(\frac{\Delta}{\lambda}, \varphi\right) \to p_1$; and the second term inside $|\cdot|$ approaches zero.

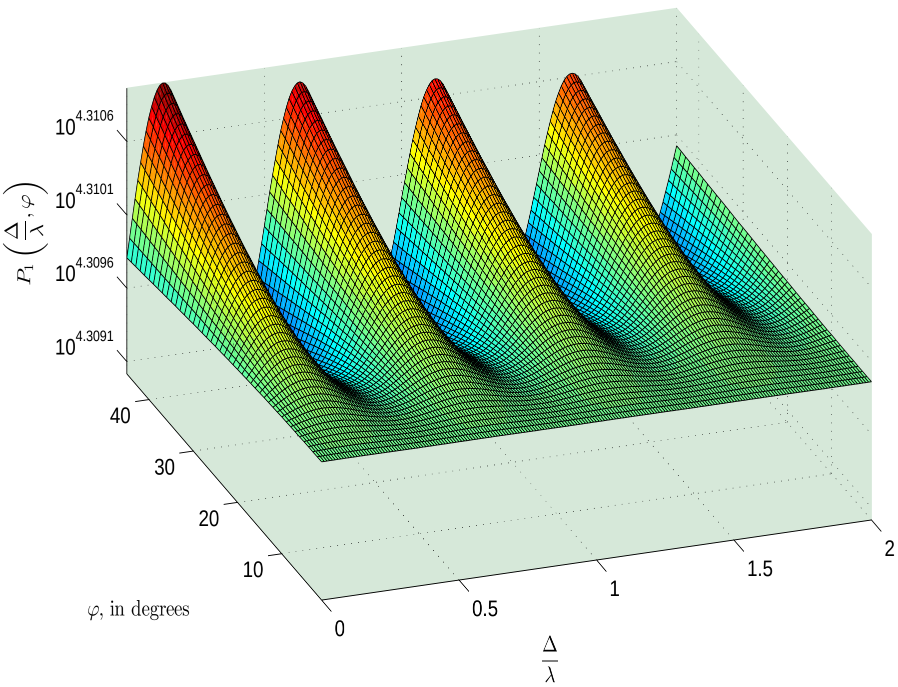

Figure 5.9: How $P_1\left(\varphi, \frac{\Delta}{\lambda}\right)$ varies with φ and $\frac{\Delta}{\lambda}$.

The two dipoles' skew angle φ affects $|Z_{1,1}| = |Z_{2,2}|$ only through $\sin^2(\varphi)$. This $\sin^2(\varphi)$ multiplicative factor may be interpreted to arise from the round-trip propagation of the radiated electric field, from the excited dipole, to the induced dipole, then back to the excited dipole. Recalling that these two dipoles are skewed with respect to each other by φ, this induced electric field (as mentioned in Section 5.2.1) is proportional to $|\sin(\varphi)|$ for each one-way propagation. When the two dipoles are orthogonal (i.e. $\varphi = 0$), the second term inside $|\cdot|$ equals zero. The variation of $P_1\left(\varphi, \frac{\Delta}{\lambda}\right)$ with φ and $\frac{\Delta}{\lambda}$ is illustrated in Figure 5.9.

The two preceding paragraphs point out that the second term inside $|\cdot|$ approaches zero, if and only if either the two dipoles are orthogonal (i.e. $\varphi = 0$) or very far apart ($\frac{\Delta}{\lambda} \to \infty$), when the driving dipole would become effectively isolated from the induced dipole. Hence, that second term could be interpreted to correspond to re-radiation from the induced dipoles. In other words, the driving dipole's self-impedance $Z_{1,1}$ is partly due to the dipole's isolated self-impedance and partly due to the electric field induced back to it by the induced dipole. The former effect, however, is at least $\frac{p_1}{p_2} \approx 207$ times more significant than the latter effect. This is reasonable in terms of antenna electromagnetics: The inter-dipole coupling's aforementioned round-trip effect (i.e. round trip from the driving dipole to the induced dipole, then back to the driving dipole) is small relative to the driving dipole's own isolated self-impedance.

When either the two dipoles are very widely separated or are orthogonally oriented, the model in (5.4) degenerates to the mathematical form of $p_1 P_3\left(\frac{L}{\lambda}\right)$, which is a reasonable representation of an isolated dipole's self-impedance. The dipoles' length $\frac{L}{\lambda}$ affects $|Z_{1,1}| = |Z_{2,2}|$ only through the multiplicative factor $P_3\left(\frac{L}{\lambda}\right)$. Figure 5.10 plots $P_3\left(\frac{L}{\lambda}\right)$ alongside $\frac{L}{\lambda}$. This term is the dominating factor in (5.4).

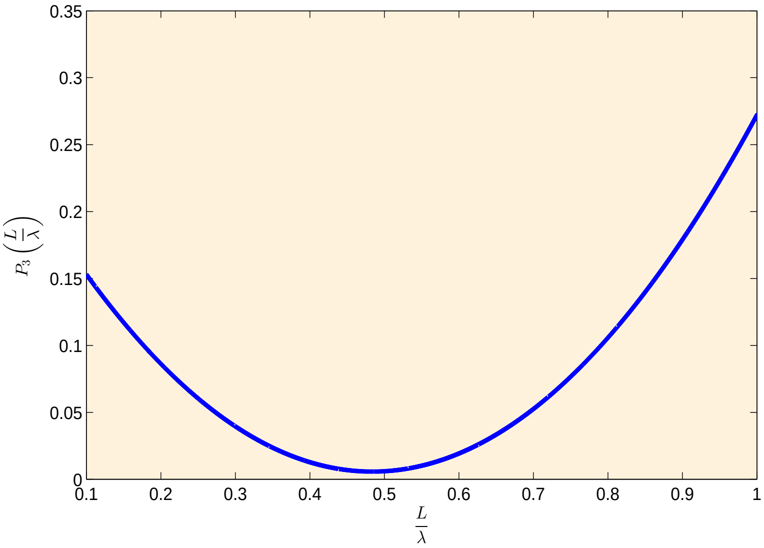

Figure 5.10: How $P_3\left(\frac{L}{\lambda}\right)$ varies with $\frac{L}{\lambda}$. Observe that resonance is near $\frac{L}{\lambda} = 0.50$. This minimum value is exactly at $\frac{L}{\lambda} = 0.48$.

Analysis of $P_2\left(\frac{\Delta}{\lambda}\right)$

The model in (5.4) varies with $\frac{\Delta}{\lambda}$ as a dampened sinusoid, with an inter-peak gap and an inter-null gap of roughly $\frac{\Delta}{\lambda} \approx \frac{1}{2}$. Figure 5.11 shows how $P_2\left(\frac{\Delta}{\lambda}\right)$ varies with $\frac{\Delta}{\lambda}$. As $\frac{\Delta}{\lambda} \to \infty$, the factor $P_2\left(\frac{\Delta}{\lambda}\right) \to 0$. This is also reasonable in terms of electromagnetics, because the two skewed dipoles (being very far apart) would become electromagnetically isolated from each other. $|Z_{1,1}| = |Z_{2,2}|$ is a damped sinusoid of the inter-dipole separation $\frac{\Delta}{\lambda}$. This is reasonable in terms of antenna electromagnetics: As $\frac{\Delta}{\lambda}$ widens, the induced electric field decreases in magnitude, hence the exponentially decaying factor of $e^{-p_5 \frac{\Delta}{\lambda}}$.

The $\cos(\cdot)$ arises due to the summation (at the driving dipole) between the driving electric field and the scattered electric field. This summation could be constructive or destructive or in between, depending on the two electric fields' phases. The summation would be perfectly constructive if the two dipoles are separated by an integer number of $\frac{\lambda}{2}$, which would correspond to an inter-dipole round-trip distance 2Δ of an integer multiple of λ.

Note that $p_3 \approx 4\pi$, that would give a period of $\Delta = \frac{\lambda}{2}$ in the $\cos(\cdot)$ factor. That period corresponds to a round-trip of $2\Delta = \lambda$ between the 2 dipoles. However, p_3 is

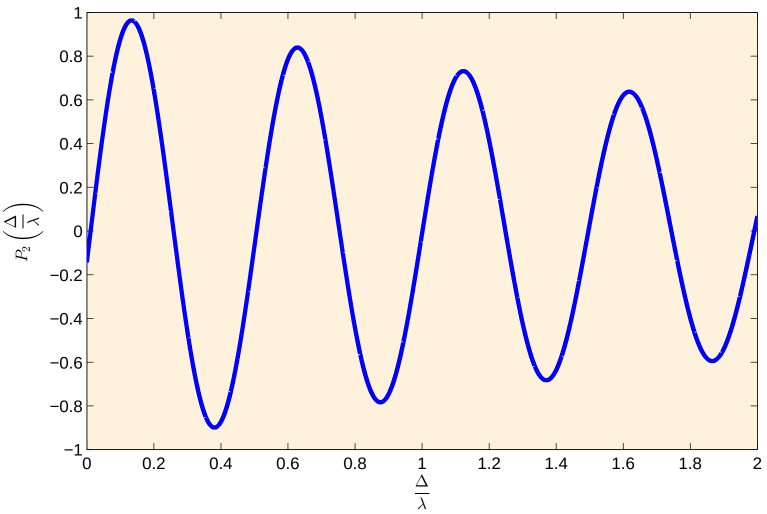

Figure 5.11: How $P_2\left(\frac{\Delta}{\lambda}\right)$ varies with $\frac{\Delta}{\lambda}$. Here, there are 4 peaks and nulls. The absolute maximum is at $\frac{\Delta}{\lambda} = 0.13$ with an amplitude of 0.96, while the absolute minimum is at $\frac{\Delta}{\lambda} = 0.38$ with an amplitude of -0.90.

not exactly 4π, because the aforementioned induced field effects involve the entire length of each dipole; hence, the above-mentioned inter-dipole separation considerations involve not just the separation between the two dipoles' feeding points.

To locate peaks and nulls of $P_2\left(\frac{\Delta}{\lambda}\right)$ in (5.4) within $\frac{\Delta}{\lambda} = [0, 2]$, get the first derivative of $P_2\left(\frac{\Delta}{\lambda}\right)$.

$$P_2'\left(\frac{\Delta}{\lambda}\right) = e^{-p_5\frac{\Delta}{\lambda}}\left\{-p_5\cos\left(p_3\frac{\Delta}{\lambda}+p_4\right) - p_3\sin\left(p_3\frac{\Delta}{\lambda}+p_4\right)\right\} \tag{5.6}$$

To obtain the critical points of P_2, set (5.6) to zero.

$$0 = e^{-p_5\frac{\Delta}{\lambda}}\left\{-p_5\cos\left(p_3\frac{\Delta}{\lambda}+p_4\right) - p_3\sin\left(p_3\frac{\Delta}{\lambda}+p_4\right)\right\}.$$

Within the interval $[0, 2]$, the zeros of $P_2'(\cdot)$ are

$$\frac{\Delta}{\lambda} = \frac{\tan^{-1}\left(\frac{-p_5}{p_3}\right) + n\pi - p_4}{p_3}. \tag{5.7}$$

The tangent function has a period of π, hence $n\pi$ is added in equation (5.7). At $n = 4, 5, 6, 7, 8, 9, 10, 11$, (5.7) respectively gives the local maxima or minima of $\frac{\Delta}{\lambda} = 0.1334, 0.3809, 0.6283, 0.8758, 1.1232, 1.3707, 1.6181, 1.8656$, with these corresponding peak/null values from (5.4)

$$\begin{aligned}
P_1(0.1334) &:= 0.9633, \\
P_1(0.3809) &:= -0.8992, \\
P_1(0.6283) &:= 0.8394, \\
P_1(0.8758) &:= -0.7836, \\
P_1(1.1232) &:= 0.7314, \\
P_1(1.3707) &:= -0.6828, \\
P_1(1.6181) &:= 0.6374, \\
P_1(1.8656) &:= -0.5950.
\end{aligned}$$

As $P_2(0.1334) := 0.9633$ is the maximum value for $\frac{\Delta}{\lambda} = [0, 2]$, the absolute maximum point is at $\frac{\Delta}{\lambda} = 0.1334$. While the absolute minimum is at $\frac{\Delta}{\lambda} = 0.3809$. The four peaks occur at $\frac{\Delta}{\lambda} = 0.1334, 0.6283, 1.1232, 1.6181$, whereas the four nulls occur at $\frac{\Delta}{\lambda} = 0.3809, 0.8758, 1.3707, 1.8656$.

$|Z_{1,1}| = |Z_{2,2}|$ at "resonance" near $\frac{L}{\lambda} = 0.5$.

According to electromagnetics, the $|Z_{1,1}|$ and $|Z_{2,2}|$ should go through a minimum at near $\frac{L}{\lambda} = 0.5$. This is half-wave dipole's first resonance.

Substituting the values of $p_1, p_2, ..., p_7$ into (5.4),

$$\begin{aligned}
|Z_{1,1}| &= \left\{20415.4041 + 98.3895\cos\left(4.0412\pi\frac{\Delta}{\lambda} + 3.4539\pi\right) e^{-0.2782\frac{\Delta}{\lambda}}\sin^2(\varphi)\right\} \\
&\quad \left\{\left(\frac{L}{\lambda} - 0.4838\right)^2 + 0.0057\right\} \qquad (5.8)
\end{aligned}$$

The use of built-in function ‘fminsearch” from MATLAB for $\frac{\Delta}{\lambda} = [0.01, 2.0]$, and $\varphi = [1^\circ, 45^\circ]$ in (5.8) results to $\frac{L}{\lambda} = 0.4838$.

Another way is to use Calculus.

Finding the partial derivative of $|Z_{1,1}|$ with respect to $\frac{L}{\lambda}$,

$$\begin{aligned} \frac{\partial(|Z_{1,1}|)}{\partial \frac{L}{\lambda}} &= \left\{20415.4041 + 98.3895 \cos\left(4.0412\pi\frac{\Delta}{\lambda} + 3.4539\pi\right) e^{-0.2782\frac{\Delta}{\lambda}} \sin^2(\varphi)\right\} \\ &\quad \left\{2\left(\frac{L}{\lambda} - 0.4838\right)\right\} \qquad (5.9) \end{aligned}$$

Setting (5.9) to zero and solving for $\frac{L}{\lambda}$, for $\frac{\Delta}{\lambda} = [0.01, 2.0]$, $\varphi = [1^\circ, 45^\circ]$ results to $\frac{L}{\lambda} = 0.4838$.

Now, to determine if the $\frac{L}{\lambda} = 0.4838$ is indeed minimum, we now get the second derivative.

$$\begin{aligned} \frac{\partial^2(|Z_{1,1}|)}{\partial \frac{L}{\lambda}^2} &= \left\{20415.4041 + 98.3895 \cos\left(4.0412\pi\frac{\Delta}{\lambda} + 3.4539\pi\right) e^{-0.2782\frac{\Delta}{\lambda}} \sin^2(\varphi)\right\} \\ &\quad \{2\} \qquad (5.10) \end{aligned}$$

For $\frac{\Delta}{\lambda} = [0.01, 2.0]$ and $\varphi = [1^\circ, 45^\circ]$, $\frac{\partial^2(|Z_{1,1}|)}{\partial \frac{L}{\lambda}^2} > 0.$.

Since, the values of the second derivative are all greater than zero for all $\frac{\Delta}{\lambda}$’s and φ’s , therefore $\frac{L}{\lambda} = 0.4838$, through the second derivative test, is indeed a minimum. Hence, we can conclude that at $L \approx 0.48\lambda$, the first resonance of the half-wave dipole according to electromagnetics has been achieved.

5.3.2 Phase of $Z_{1,1}$ and $Z_{2,2}$

All candidate models are presented in Appendix D. The best-fitting model is

$$\begin{aligned} \angle Z_{1,1} &= \angle Z_{2,2} \\ &\approx \left\{ q_1 + \overbrace{q_2 \sin\left(q_3 \frac{\Delta}{\lambda}\right) \; e^{-q_4 \frac{\Delta}{\lambda}}}^{Q\left(\frac{\Delta}{\lambda}\right) :=} \right\} \sin\left(q_5 \frac{L}{\lambda}\right), \end{aligned} \tag{5.11}$$

where

$$\begin{aligned} q_1 &:= 1.7648, \\ q_2 &:= 0.0103, \\ q_3 &:= 0.7091\pi, \\ q_4 &:= 5.0565, \\ q_5 &:= -2.0758\pi. \end{aligned}$$

The goodness-of-fit R^2 equals 0.90; hence, only 10% of the VLab's numerical data cannot be explained by the above model.

Like $|Z_{1,1}| = |Z_{2,2}|$ in Section 5.3.1, the phenomenological model here for $\angle Z_{1,1} = \angle Z_{2,2}$ has two terms inside the curly brackets. The first term corresponds to each dipole's isolated self-impedance, whereas the second term, $Q\left(\frac{\Delta}{\lambda}\right)$, arises due to the re-radiation from the induced dipole back to the driving dipole. The first term dominates the second term (by a ratio of $\frac{q_1}{q_2} \approx 171$ multiples), as would be expected and as explained in Section 5.3.1. Figure 5.12 shows how $Q\left(\frac{\Delta}{\lambda}\right)$ varies with $\frac{\Delta}{\lambda}$.

Like $\angle Z_{1,2} = \angle Z_{2,1}$ in Section 5.2.2, the phenomenological model here for $\angle Z_{1,1} = \angle Z_{2,2}$ is independent of φ, for reasons already explained in Section 5.2.2. The plot of the phenomenological model for $\angle Z_{1,1}$ against $\frac{L}{\lambda}$ and $\frac{\Delta}{\lambda}$ is shown in Figure 5.13.

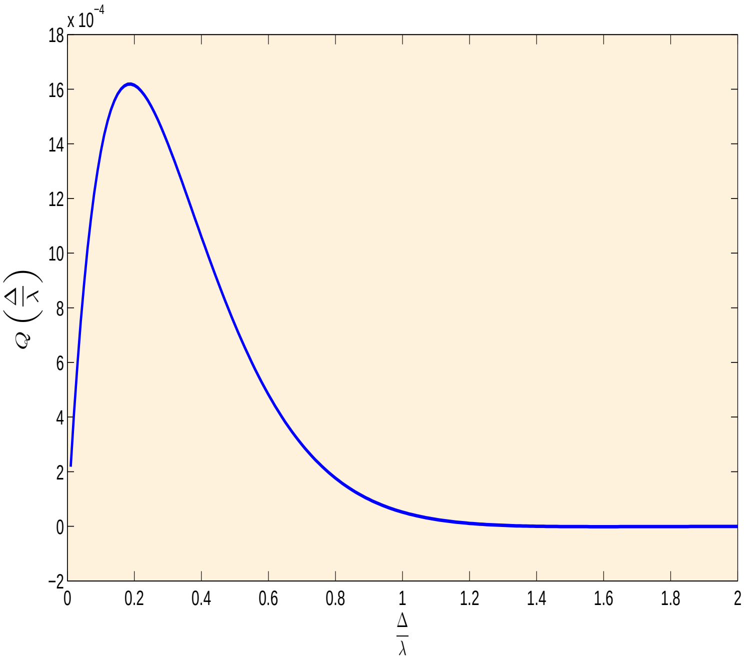

Figure 5.12: How $Q\left(\frac{\Delta}{\lambda}\right)$ varies with $\frac{\Delta}{\lambda}$

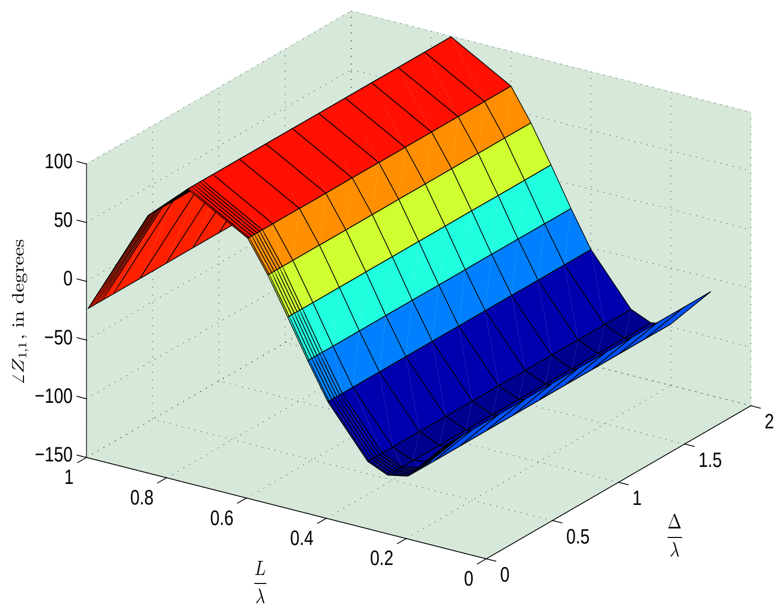

Figure 5.13: How $\angle Z_{1,1}$ varies with $\frac{\Delta}{\lambda}$ and $\frac{L}{\lambda}$.

Summary

As earlier promised, the obtained phenomenological models with simple and tractable expressions of the mutual and self-impedance, in simple closed forms, are now obtained and introduced.

Table 5.1 summarizes the phenomenological models and the optimized parameters for $|Z_{1,2}| = |Z_{2,1}|$, $\angle Z_{1,2} = \angle Z_{2,1}$, $|Z_{1,1}| = |Z_{2,2}|$, $\angle Z_{1,1} = \angle Z_{2,2}$.

Table 5.1: Summary of the Obtained Phenomenological Models for Skewed Cross Dipoles

Entity	Phenomenological Model
$\lvert Z_{1,2}\rvert = \lvert Z_{2,1}\rvert$	$10^{a_1} \left(\frac{\Delta}{\lambda}\right)^{-a_2} \left(\frac{L}{\lambda}\right)^{a_3} (\sin(\varphi))$ where $a_1 = 2.3018,\ a_2 = 0.5564,\ a_3 = 2.6230.$
$\angle Z_{1,2} = \angle Z_{2,1}$	$b_1\frac{\Delta}{\lambda} + b_2\frac{L}{\lambda} + b_3$ where $b_1 = -5.5920,\ b_2 = 1.5858,\ b_3 = -0.2952.$
$\lvert Z_{1,1}\rvert = \lvert Z_{2,2}\rvert$	$\left\lvert p_1 + p_2 \cos\left(p_3\frac{\Delta}{\lambda} + p_4\right) e^{-p_5\frac{\Delta}{\lambda}} \sin^2(\varphi)\right\rvert \left\{\left(\frac{L}{\lambda} - p_6\right)^2 + p_7\right\}$ where $p_1 = 20415.4041,\ p_2 = 98.3895,\ p_3 = 4.0412\pi,\ p_4 = 3.4539\pi,$ $p_5 = 0.2782,\ p_6 = 0.4838,\ p_7 = 0.0057.$
$\angle Z_{1,1} = \angle Z_{2,2}$	$\left\{q_1 + q_2 \sin\left(q_3\frac{\Delta}{\lambda}\right) e^{-q_4\frac{\Delta}{\lambda}}\right\} \sin\left(q_5\frac{L}{\lambda}\right)$ where $q_1 = 1.7648,\ q_2 = 0.0103,\ q_3 = 0.7091\pi,$ $q_4 = 5.0565,\ q_5 = -2.0758\pi.$

Chapter 6

Direction-of-Arrival Estimation to Demonstrate the Usefulness of the Proposed Models

Introduction

To demonstrate the usefulness of the phenomenological models in (5.1), (5.3), (5.4), (5.11) — these new models are utilized below in the estimation of an incident source's azimuth-elevation direction-of-arrival (DOA).

6.1 The Skewed Dipole-Pair's Electromagnetic Measurement Model

The first dipole is aligned along the z-axis and is centered at the Cartesian origin. The second dipole lies on the x-y plane and is centered at the Cartesian point of $(\Delta, 0, 0)$, as shown in Figure 4.5. The second dipole's location incurs a spatial phase factor of $e^{j2\pi\frac{\Delta}{\lambda}\sin(\theta)\cos(\phi)}$, where $\theta \in [0°, 180°]$ symbolizes the incident source's polar angle of arrival, and $\phi \in [0°, 360°)$ denotes the azimuth angle of arrival measured from the positive x-axis. The second dipole's skewed orientation on the y'-z' plane implies that its voltage is affected by the incident electromagnetic wave's y-component and z-component.

If these dipoles are of wavelength-normalized lengths greater than 0.10 (i.e. with $\frac{L}{\lambda} > \frac{1}{10}$), the skewed-dipoles would have this 2×1 array manifold [103,141]:

$$
\begin{aligned}
&\mathbf{a}_{\text{pair}}(\theta, \phi, \gamma, \eta) \\
&= \mathbf{C} \begin{bmatrix} 1 & 0 \\ 0 & e^{j2\pi \frac{\Delta}{\lambda} \sin(\theta)\cos(\phi)} \end{bmatrix} \begin{bmatrix} 0 & 1 \\ \cos(\varphi) & \sin(\varphi) \end{bmatrix} \begin{bmatrix} -\sin(\theta) & 0 \\ \cos(\theta)\sin(\phi) & \cos(\phi) \end{bmatrix} \\
&\quad \begin{bmatrix} e^{j\eta}\sin\gamma \\ \cos\gamma \end{bmatrix} \circ \begin{bmatrix} \ell_\theta^{(L)} \\ \ell_\psi^{(L)} \end{bmatrix} \circ \begin{bmatrix} \csc(\theta) \\ \csc(\psi) \end{bmatrix}.
\end{aligned} \tag{6.1}
$$

where

$$
\begin{aligned}
\ell_\theta^{(L)} &= -\frac{\lambda}{\pi} \frac{1}{\sin\left(\pi \frac{L}{\lambda}\right)} \frac{\cos\left(\pi \frac{L}{\lambda} \cos(\theta)\right) - \cos\left(\pi \frac{L}{\lambda}\right)}{\sin(\theta)}, \\
\ell_\psi^{(L)} &= -\frac{\lambda}{\pi} \frac{1}{\sin\left(\pi \frac{L}{\lambda}\right)} \frac{\cos\left(\pi \frac{L}{\lambda} \cos(\psi)\right) - \cos\left(\pi \frac{L}{\lambda}\right)}{\sin(\psi)}, \\
\cos(\psi) &= \sin(\theta)\sin(\phi)\cos(\varphi) + \cos(\theta)\sin(\varphi), \\
\sin(\psi) &= \sqrt{\sin^2(\theta)\sin^2(\varphi) + \cos^2(\theta)\cos^2(\varphi) + \sin^2(\theta)\cos^2(\phi)\cos^2(\varphi) - 2\sin(2\theta)\sin(2\varphi)\sin(\phi)}
\end{aligned}
$$

In the above, $\gamma \in [0, \frac{\pi}{2}]$ denotes the auxiliary polarization angle, $\eta \in [-\pi, \pi]$ refers to the polarization phase difference, $\ell_\theta^{(L)}$ and $\ell_\psi^{(L)}$ denote the effective lengths of dipoles, ψ refers to the angle made between the slanted dipole and the unit vector along the direction of propagation and $\mathbf{C}$ symbolizes the skewed-dipoles' 2×2 electromagnetic coupling matrix. $\circ$ denotes element-wise multiplication.

This coupling matrix is related to the impedance matrix $\mathbf{Z}$ as follows: [14, 26, 38, 41, 58, 59, 66, 109, 116]

$$\mathbf{C} \;=\; \left(\frac{\mathbf{Z}}{Z_0} + \mathbf{I}\right)^{-1}, \tag{6.2}$$

where $Z_0 = 50\ \Omega$ and $\mathbf{I}$ is an identity matrix.

The subsequent direction-finding study would consider three cases:

(A) The actual impedance matrix is exactly known to the direction-of-arrival estimation algorithm. Here, $\mathbf{Z}$ would equal the VLab output values. This case corresponds to the dotted black curve on the subsequent graphs.

(B) The actual impedance matrix is *un*known to the direction-of-arrival estimation algorithm. Instead, the phenomenological models of (5.1), (5.3), (5.4), (5.11) are used to form $\mathbf{Z}$ for use in the estimation algorithm. This case corresponds to the solid red curve on the subsequent graphs.

(C) Mutual coupling is presumed erroneously by the direction-of-arrival estimation algorithm to be nonexistent. Here, $\mathbf{Z}$ equals a 2×2 matrix of all zeros. This case corresponds to the dash-dot blue curve on the subsequent graphs.

6.2 The Data's Statistical Model

Let the receiver be equipped with a square array of four identical pairs of skewed-dipoles, each of which is as described above in Section 6.1(see Figure 6.1).

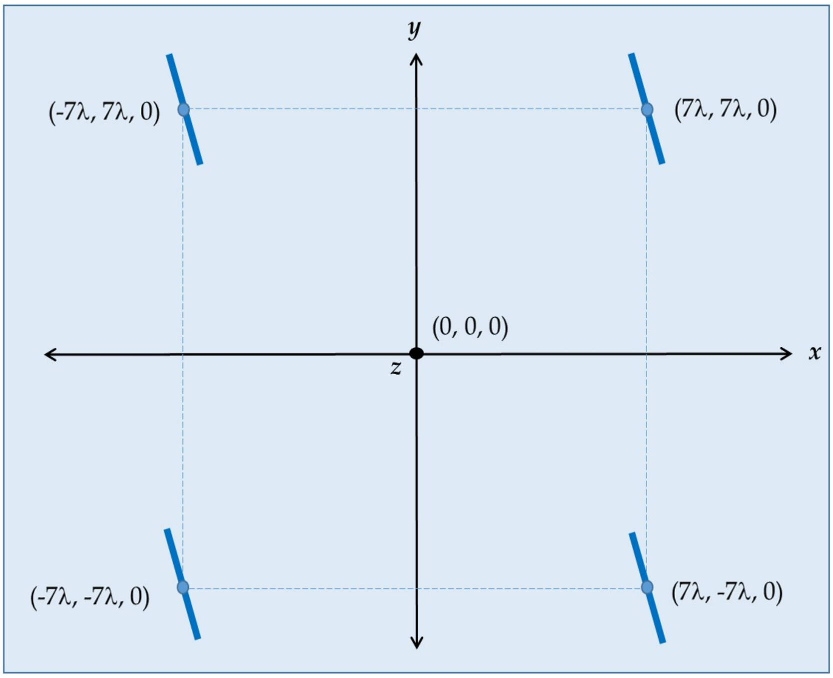

Figure 6.1: The square array of crossed dipoles separated by a distance of 14λ. The inter-pair coupling is negligible at this distance.

This square array's each side is 14λ in length – a separation long enough to render any inter-pair coupling to be negligible. This array's 8×1 array manifold may be represented as

$$\mathbf{a}_{\text{array}} = \mathbf{a}_{\text{pair}} \otimes \begin{bmatrix} \exp\{j7\pi\sin(\theta)[+\sin(\phi)+\cos(\phi)]\} \\ \exp\{j7\pi\sin(\theta)[+\sin(\phi)-\cos(\phi)]\} \\ \exp\{j7\pi\sin(\theta)[-\sin(\phi)+\cos(\phi)]\} \\ \exp\{j7\pi\sin(\theta)[-\sin(\phi)-\cos(\phi)]\} \end{bmatrix}, \tag{6.3}$$

where $\otimes$ symbolizes the Kronecker product.

To focus on the electromagnetic coupling among the dipoles and on the proposed phenomenological models, an admittedly simple statistical model will be used below for the incident signal and the noise. Suppose a pure tone signal $s(t) = \exp[j(\omega t + \varphi)]$ impinges on aforementioned receiver. At the mth time-instant, the collected data may be modeled as an 8×1 vector of

$$\mathbf{x}(m) \quad = \quad \mathbf{a}(\theta, \phi, \gamma, \eta, \mathbf{C})\ s(m) + \mathbf{n}(m). \tag{6.4}$$

In the above, $\mathbf{n}(m)$ denotes an 8×1 vector of additive noise, modeled here as Gaussian, zero in mean, statistically uncorrelated over the time-instants and uncorrelated across all eight dipoles.

With M number of time samples, form an $8 \times M$ data matrix of

$$\mathbf{X} \quad := \quad [\mathbf{x}(1), \mathbf{x}(2), \ldots, \mathbf{x}(M)], \tag{6.5}$$

Each subsequent Monte Carlo simulation has $M = 50$ number of time-samples.

6.3 *MUSIC*-Based Direction Finding

The direction finding problem is to estimate the incident source's incident direction-of-arrival (θ, ϕ), based on the observations of $\mathbf{X}$.

The estimation algorithm has prior knowledge of the numerical values of $\frac{L}{\lambda}$, $\frac{\Delta}{\lambda}$, φ.

MUSIC [32] is a popular parameter estimator, based on a eigen-decomposition of the data correlation matrix, $\mathbf{R} := \mathbf{X}^H\mathbf{X}$. Eigen-decompose this 8×8 matrix to obtain its null space, $\mathbf{U}_{\text{null}}$.

$$\mathbf{R} \quad = \quad [\mathbf{U}_s, \mathbf{U}_n]^H \, \mathbf{\Lambda} \, [\mathbf{U}_s, \mathbf{U}_n] \,. \tag{6.6}$$

Then, the direction-of-arrival estimates and the polarization estimates are given by

$$(\hat{\theta}, \hat{\phi}, \hat{\gamma}, \hat{\eta}) \quad := \quad \underset{(\theta,\phi,\gamma,\eta)}{\arg \max} \, \frac{1}{\|\mathbf{U}_n^H \mathbf{a}(\theta, \phi, \gamma, \eta, \mathbf{C})\|^2}, \tag{6.7}$$

where $\| \cdot \|$ represents the Frobenius norm of the entity inside.

For a fair comparison across the three impedance cases (A)-(C) in Section 6.1, the signal-to-noise power ratio (SNR) plotted in the simulation figures: The coupling matrix's norm, $\|\mathbf{C}\|_2$, affects the "effective" signal-to-noise power ratio in (6.4). Hence, to fairly compare across the three settings above, the array manifold in (6.1) is normalized by $\|\mathbf{C}\|_2$.

6.4 DOA Estimation Plots

Figures 6.2 - 6.24 show the estimation root-mean-square error (RMSE) of $\hat{\theta}$ and $\hat{\phi}$, versus the SNR. Each icon in Figures 6.2 to 6.24 represents 100 independent Monte Carlo trials. These figures verify the usefulness of the proposed phenomenological models — that these models offer estimation precisions almost as good as if the exact impedance were known, whereas ignoring mutual coupling causes a degradation that can be several orders of magnitude.

The root-mean-square error values are all expressed in degrees. From all the plots presented here, the average root-mean-square error values at SNR = 10 dB for $\hat{\theta}$ equals 0.057°. At SNR = 10 dB, the minimum and maximum values for all $\hat{\theta}$'s are 0.044° and 0.097°, respectively. At SNR = 30 dB, the average of all the root-mean-square errors for all $\hat{\theta}$'s equals 0.006°. The minimum and maximum values for all $\hat{\theta}$'s are 0.004° and 0.010°, respectively.

The average root-mean-square values of $\hat{\phi}$'s at SNR = 10 dB and SNR = 30 dB are 0.098° and 0.010°, respectively. At SNR = 10 dB, the minimum and maximum values for all $\hat{\phi}$'s are 0.044° and 0.270°, respectively. While at SNR = 30 dB, the minimum and maximum values for all $\hat{\theta}$'s are 0.025° and 0.005°, respectively.

The performance of the MUSIC algorithm is generally better in estimating the zenith angle, θ than the azimuthal angle, ϕ. Nonetheless, examining the recorded RMSE values for the direction-of-arrival estimation, the obtained results are overall significant.

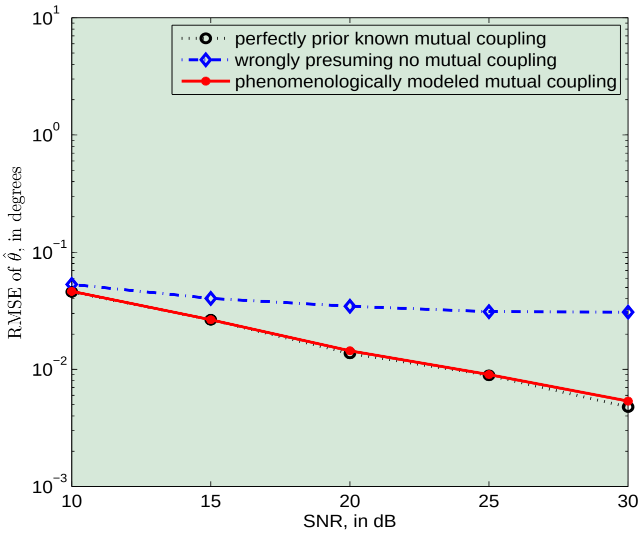

(a)

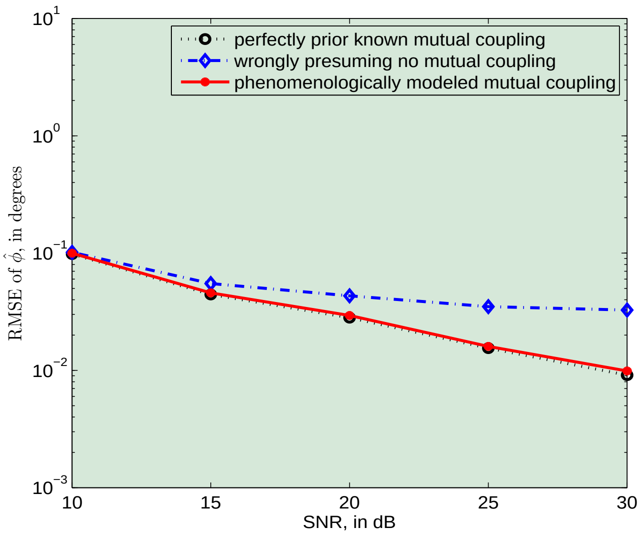

(b)

Figure 6.2: How the RMSE of (a) $\hat{\theta}$ and (b) $\hat{\phi}$ varies with the SNR. Here, $\frac{L}{\lambda} = 0.45$, $\varphi = 45^\circ$, $\frac{\Delta}{\lambda} = 0.04$, $\theta = 26^\circ$, $\phi = 12^\circ$, $\gamma = 44^\circ$, $\eta = -20^\circ$.

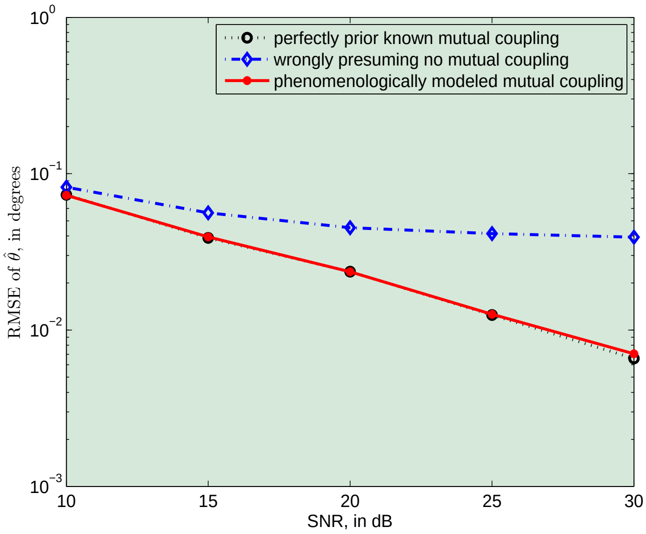

(a)

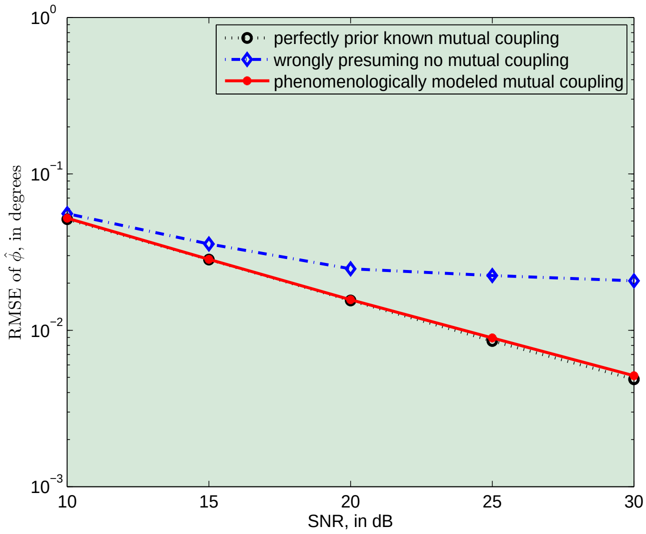

(b)

Figure 6.3: How the RMSE of (a) $\hat{\theta}$ and (b) $\hat{\phi}$ varies with the SNR. Here, $\frac{L}{\lambda} = 0.45$, $\varphi = 45°$, $\frac{\Delta}{\lambda} = 0.04$, $\theta = 55°$, $\phi = 53°$, $\gamma = 19°$, $\eta = 32°$.

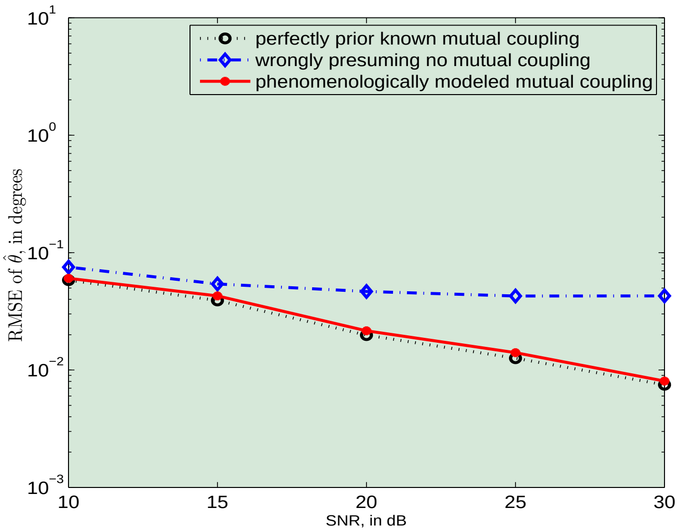

(a)

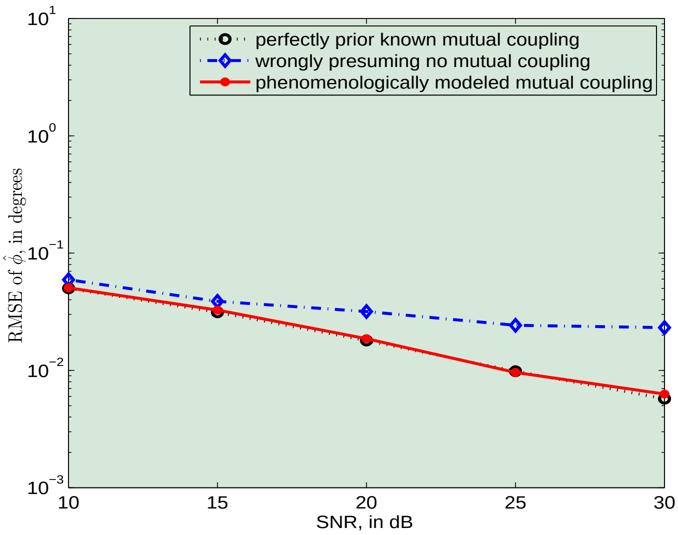

(b)

Figure 6.4: How the RMSE of (a) $\hat{\theta}$ and (b) $\hat{\phi}$ varies with the SNR. Here, $\frac{L}{\lambda} = 0.50$, $\varphi = 45°$, $\frac{\Delta}{\lambda} = 0.01$, $\theta = 50°$, $\phi = 36°$, $\gamma = 15°$, $\eta = 40°$.

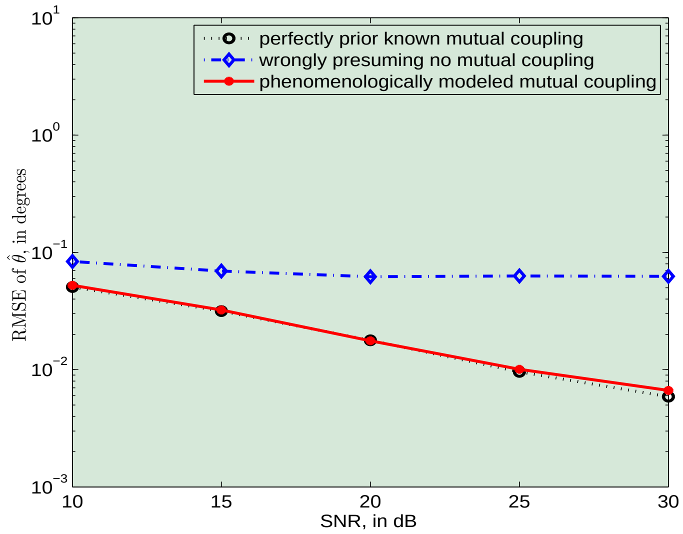

(a)

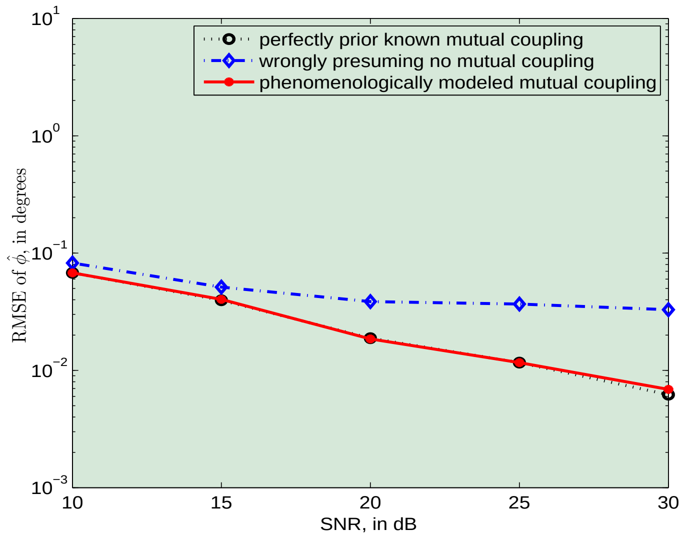

(b)

Figure 6.5: How the RMSE of (a) $\hat{\theta}$ and (b) $\hat{\phi}$ varies with the SNR. Here, $\frac{L}{\lambda} = 0.50$, $\varphi = 45°$, $\frac{\Delta}{\lambda} = 0.01$, $\theta = 40°$, $\phi = 65°$, $\gamma = 33°$, $\eta = -23°$.

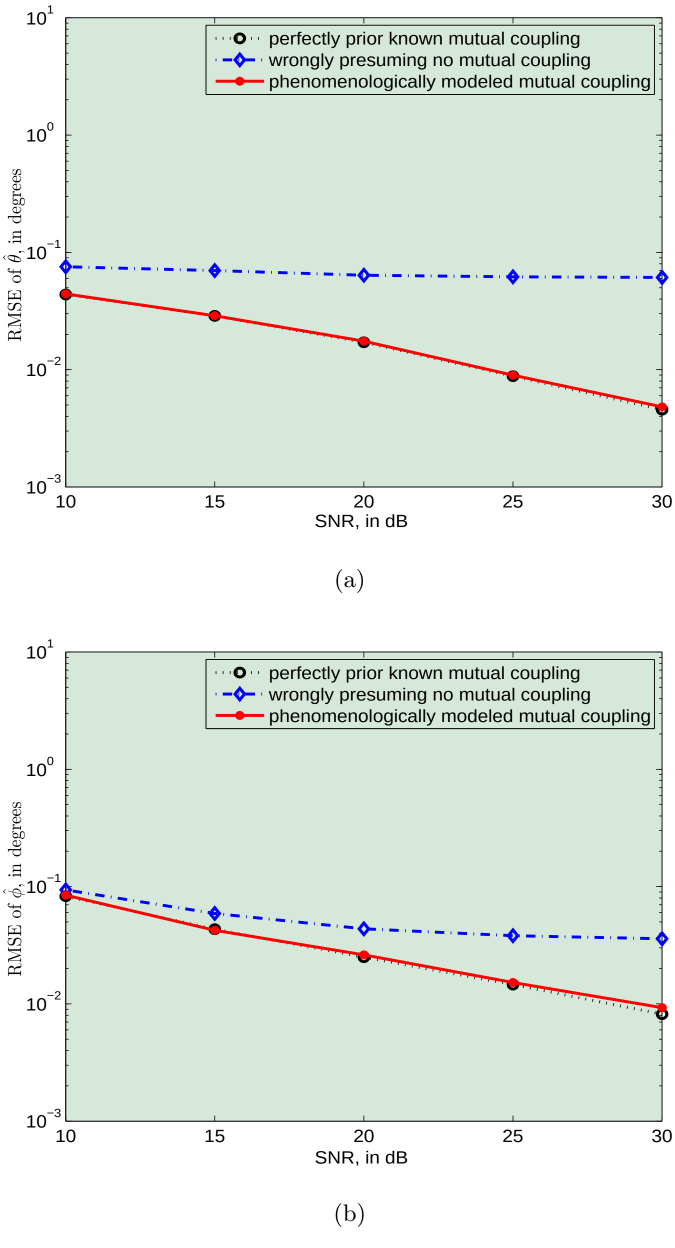

(a)

(b)

Figure 6.6: How the RMSE of (a) $\hat{\theta}$ and (b) $\hat{\phi}$ varies with the SNR. Here, $\frac{L}{\lambda} = 0.50$, $\varphi = 45°$, $\frac{\Delta}{\lambda} = 0.01$, $\theta = 32°$, $\phi = 28°$, $\gamma = 52°$, $\eta = -28°$.

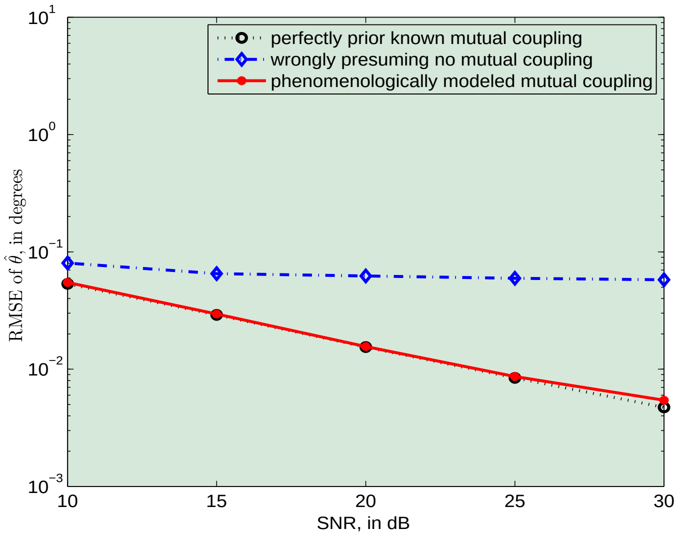

(a)

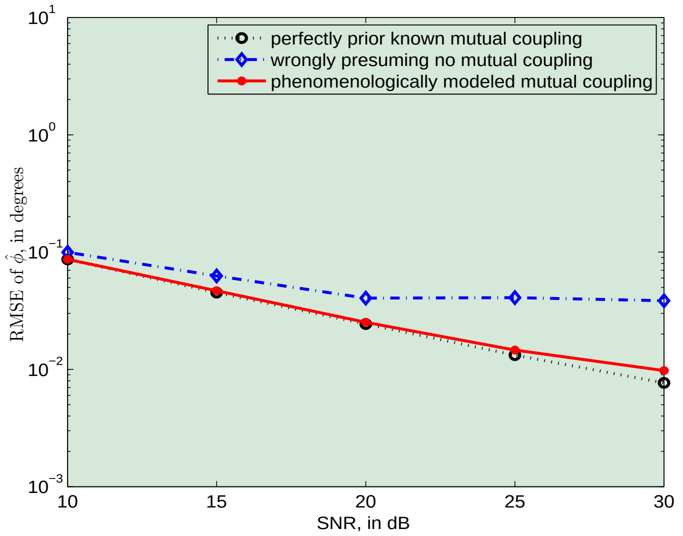

(b)

Figure 6.7: How the RMSE of (a) $\hat{\theta}$ and (b) $\hat{\phi}$ varies with the SNR. Here, $\frac{L}{\lambda} = 0.50$, $\varphi = 45^\circ$, $\frac{\Delta}{\lambda} = 0.01$, $\theta = 32^\circ$, $\phi = 28^\circ$, $\gamma = 50^\circ$, $\eta = -32^\circ$.

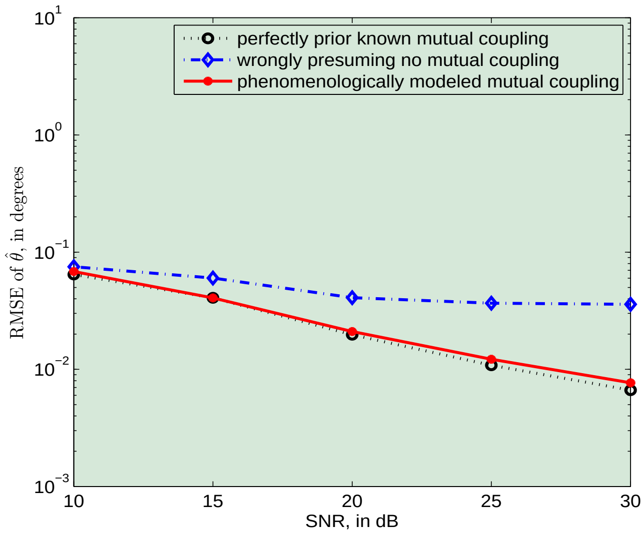

(a)

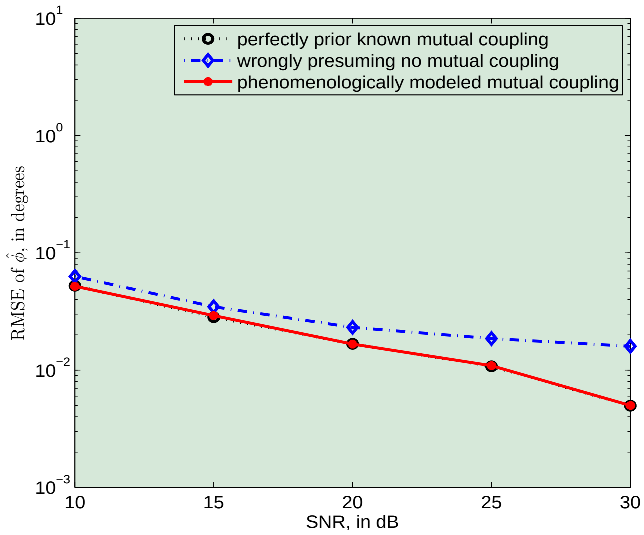

(b)

Figure 6.8: How the RMSE of (a) $\hat{\theta}$ and (b) $\hat{\phi}$ varies with the SNR. Here, $\frac{L}{\lambda} = 0.50$, $\varphi = 45^\circ$, $\frac{\Delta}{\lambda} = 0.02$, $\theta = 53^\circ$, $\phi = 30^\circ$, $\gamma = 15^\circ$, $\eta = 45^\circ$.

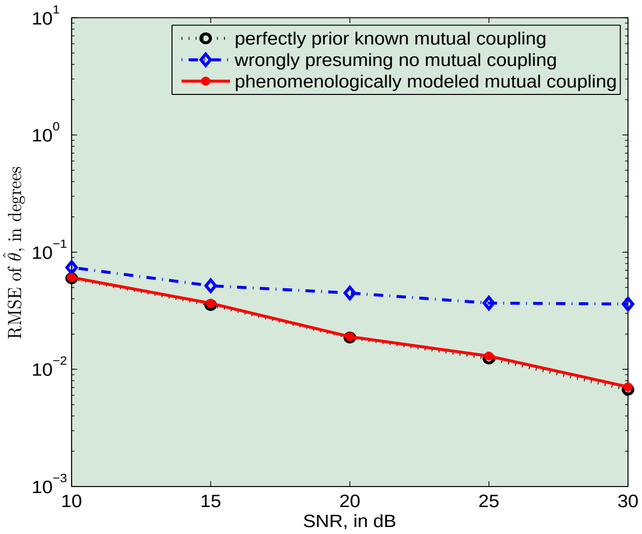

(a)

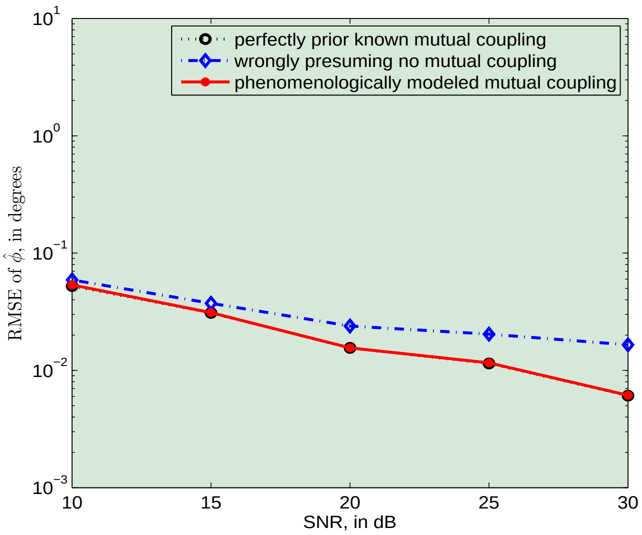

(b)

Figure 6.9: How the RMSE of (a) $\hat{\theta}$ and (b) $\hat{\phi}$ varies with the SNR. Here, $\frac{L}{\lambda} = 0.50$, $\varphi = 45°$, $\frac{\Delta}{\lambda} = 0.02$, $\theta = 48°$, $\phi = 28°$, $\gamma = 16°$, $\eta = 40°$.

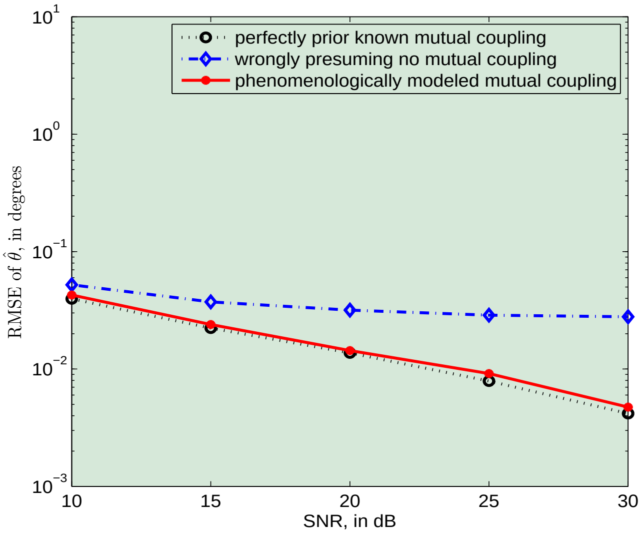

(a)

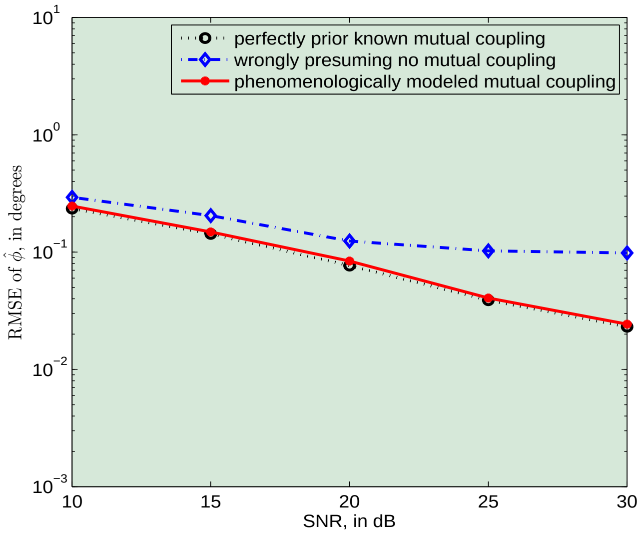

(b)

Figure 6.10: How the RMSE of (a) $\hat{\theta}$ and (b) $\hat{\phi}$ varies with the SNR. Here, $\frac{L}{\lambda} = 0.50$, $\varphi = 45^\circ$, $\frac{\Delta}{\lambda} = 0.02$, $\theta = 10^\circ$, $\phi = 36^\circ$, $\gamma = 20^\circ$, $\eta = 54^\circ$.

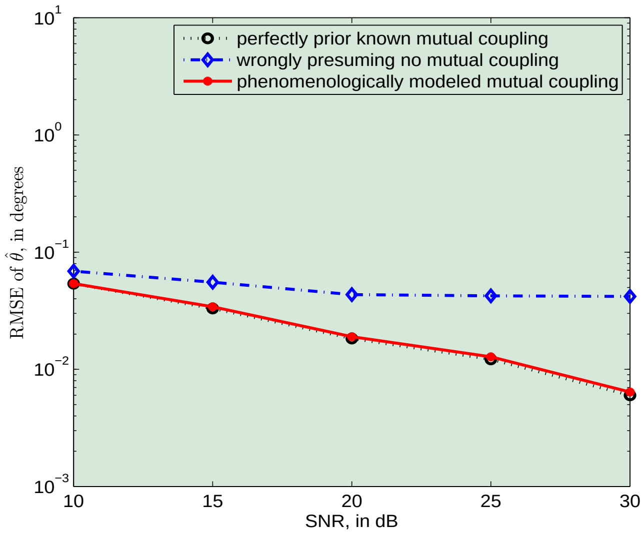

(a)

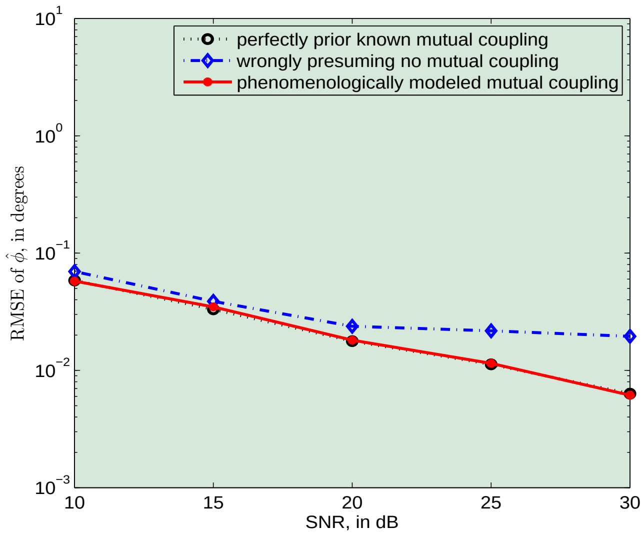

(b)

Figure 6.11: How the RMSE of (a) $\hat{\theta}$ and (b) $\hat{\phi}$ varies with the SNR. Here, $\frac{L}{\lambda} = 0.50$, $\varphi = 45°$, $\frac{\Delta}{\lambda} = 0.02$, $\theta = 48°$, $\phi = 34°$, $\gamma = 14°$, $\eta = 22°$.

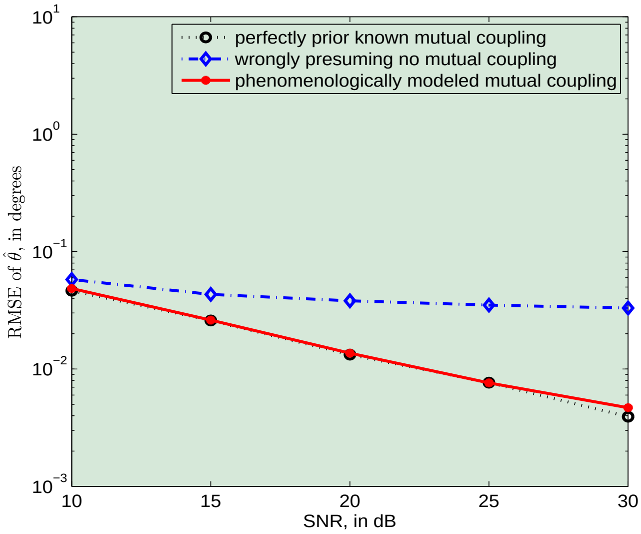

(a)

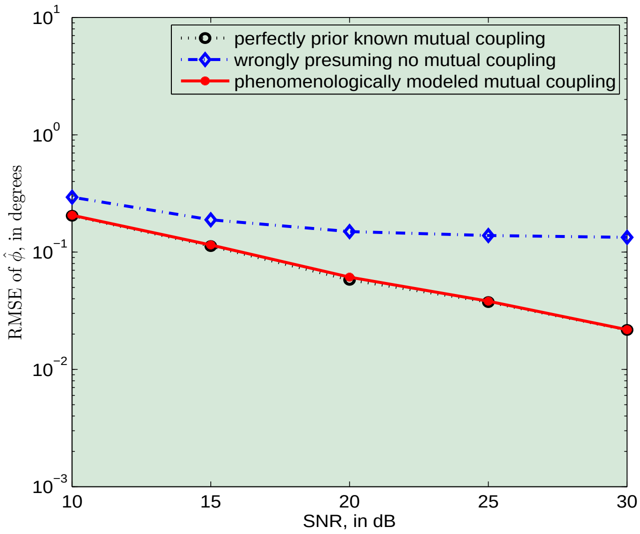

(b)

Figure 6.12: How the RMSE of (a) $\hat{\theta}$ and (b) $\hat{\phi}$ varies with the SNR. Here, $\frac{L}{\lambda} = 0.50$, $\varphi = 45°$, $\frac{\Delta}{\lambda} = 0.02$, $\theta = 12°$, $\phi = 48°$, $\gamma = 16°$, $\eta = 52°$.

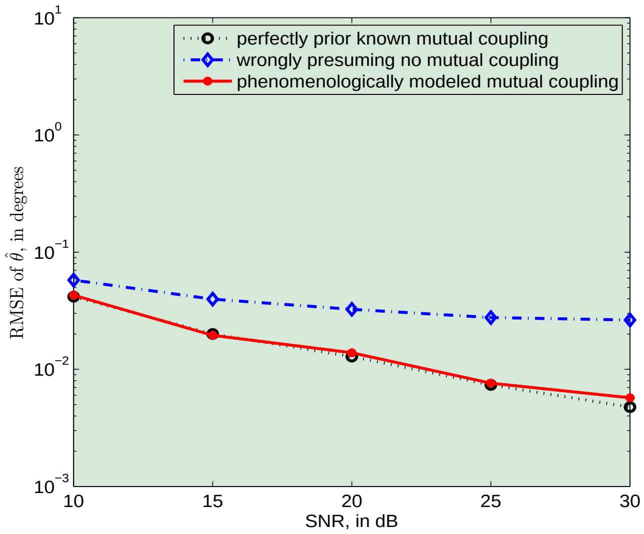

(a)

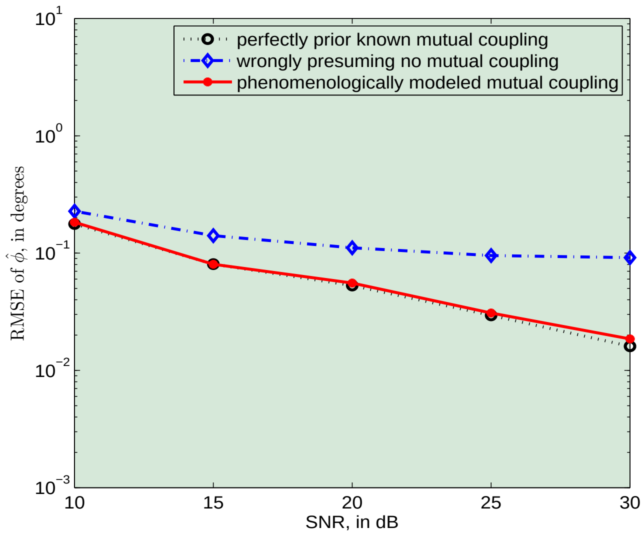

(b)

Figure 6.13: How the RMSE of (a) $\hat{\theta}$ and (b) $\hat{\phi}$ varies with the SNR. Here, $\frac{L}{\lambda} = 0.50$, $\varphi = 45°$, $\frac{\Delta}{\lambda} = 0.02$, $\theta = 14°$, $\phi = 44°$, $\gamma = 14°$, $\eta = 56°$.

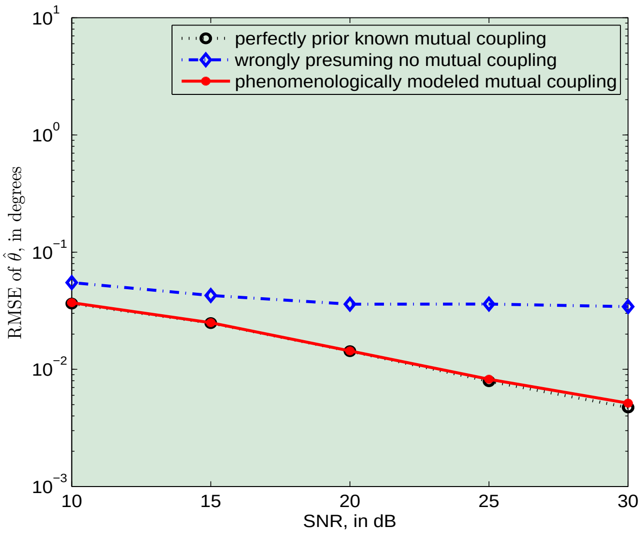

(a)

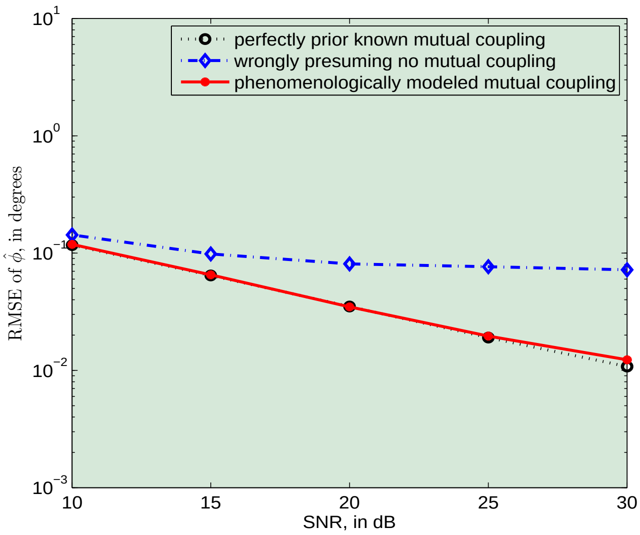

(b)

Figure 6.14: How the RMSE of (a) $\hat{\theta}$ and (b) $\hat{\phi}$ varies with the SNR. Here, $\frac{L}{\lambda} = 0.50$, $\varphi = 45°$, $\frac{\Delta}{\lambda} = 0.04$, $\theta = 22°$, $\phi = 42°$, $\gamma = 28°$, $\eta = 60°$.

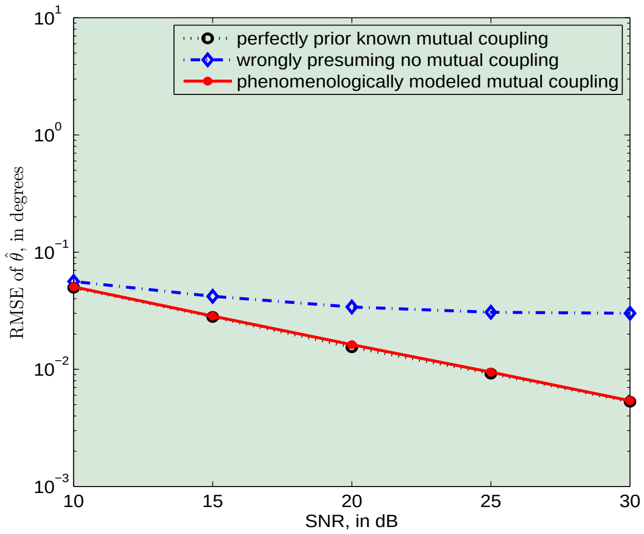

(a)

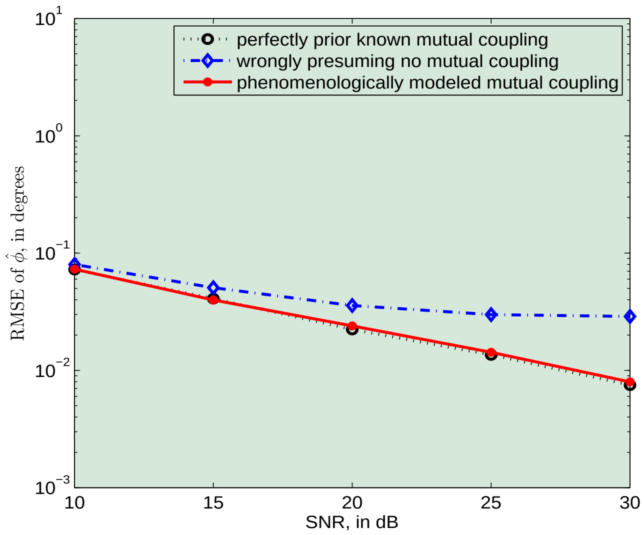

(b)

Figure 6.15: How the RMSE of (a) $\hat{\theta}$ and (b) $\hat{\phi}$ varies with the SNR. Here, $\frac{L}{\lambda} = 0.55$, $\varphi = 45°$, $\frac{\Delta}{\lambda} = 0.02$, $\theta = 34°$, $\phi = 46°$, $\gamma = 16°$, $\eta = -8°$.

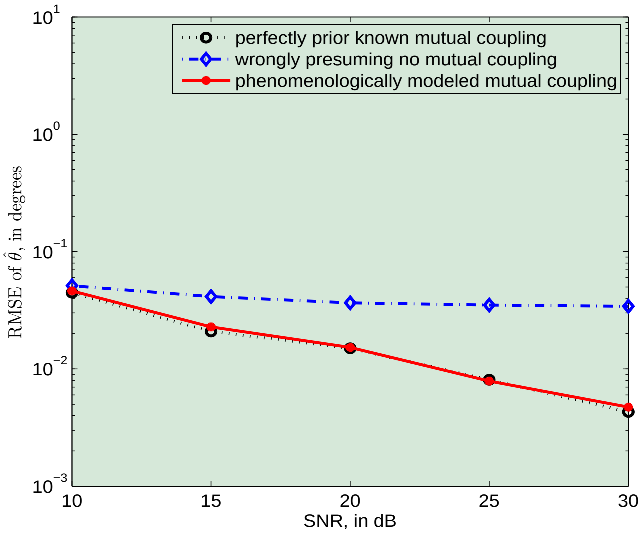

(a)

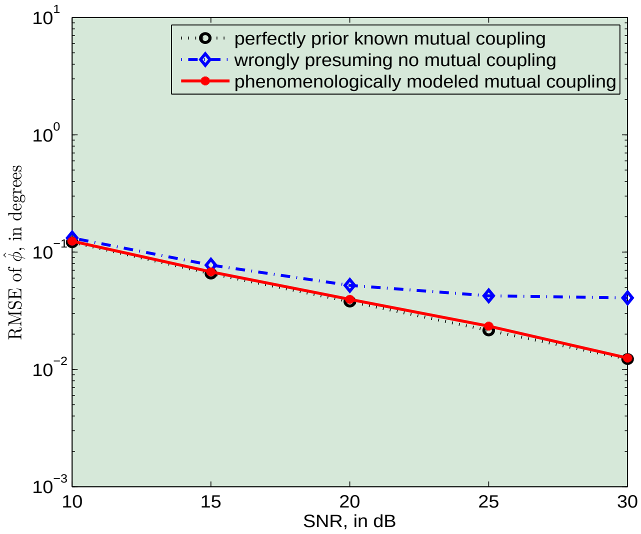

(b)

Figure 6.16: How the RMSE of (a) $\hat{\theta}$ and (b) $\hat{\phi}$ varies with the SNR. Here, $\frac{L}{\lambda} = 0.55$, $\varphi = 45^\circ$, $\frac{\Delta}{\lambda} = 0.02$, $\theta = 21^\circ$, $\phi = 46^\circ$, $\gamma = 27^\circ$, $\eta = -14^\circ$.

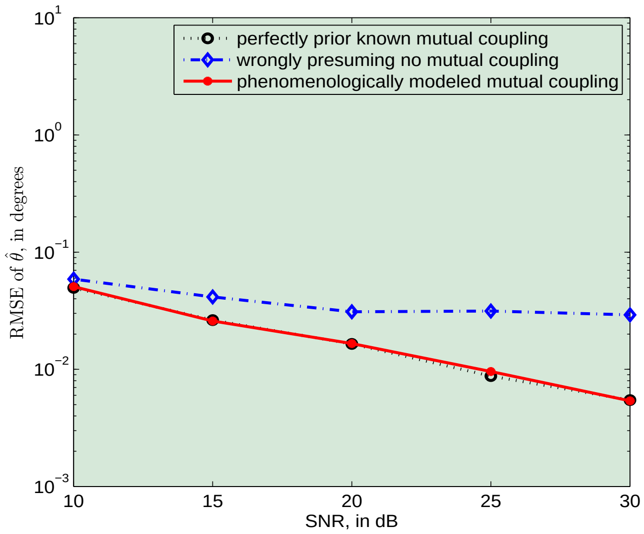

(a)

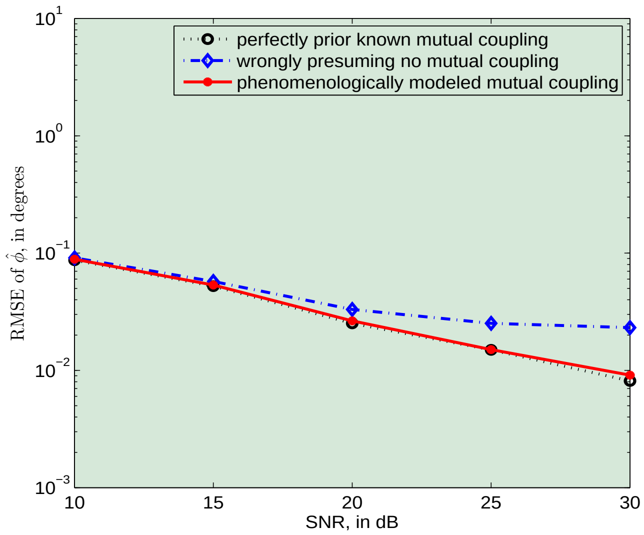

(b)

Figure 6.17: How the RMSE of (a) $\hat{\theta}$ and (b) $\hat{\phi}$ varies with the SNR. Here, $\frac{L}{\lambda} = 0.60$, $\varphi = 45°$, $\frac{\Delta}{\lambda} = 0.01$, $\theta = 30°$, $\phi = 45°$, $\gamma = 24°$, $\eta = -8°$.

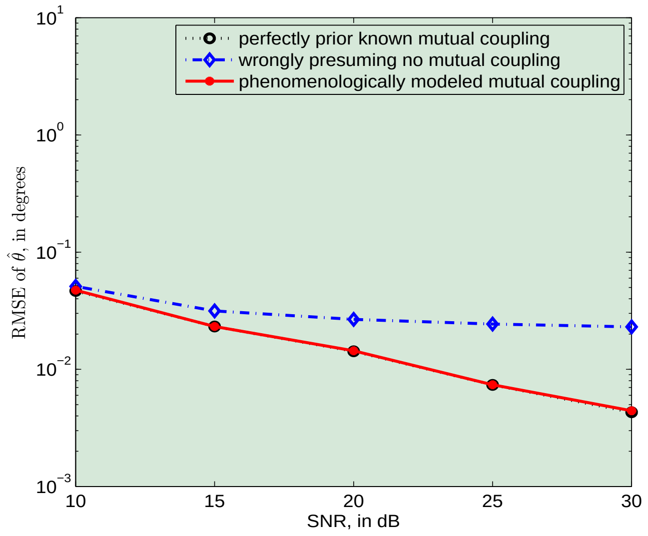

(a)

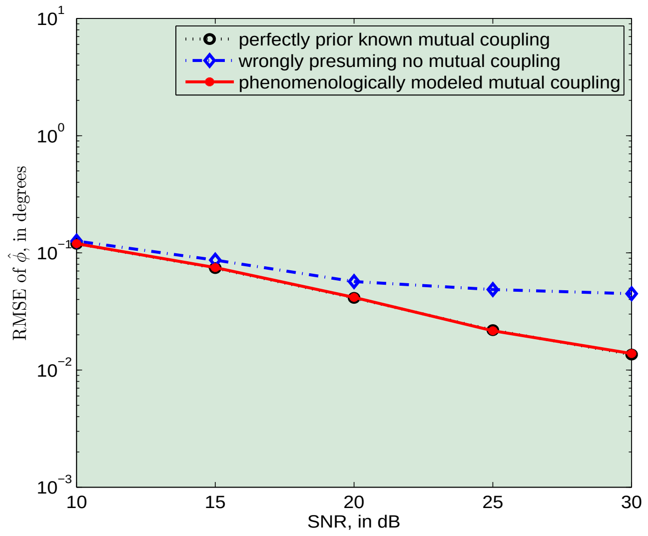

(b)

Figure 6.18: How the RMSE of (a) $\hat{\theta}$ and (b) $\hat{\phi}$ varies with the SNR. Here, $\frac{L}{\lambda} = 0.60$, $\varphi = 45°$, $\frac{\Delta}{\lambda} = 0.02$, $\theta = 19°$, $\phi = 84°$, $\gamma = 56°$, $\eta = 41°$.

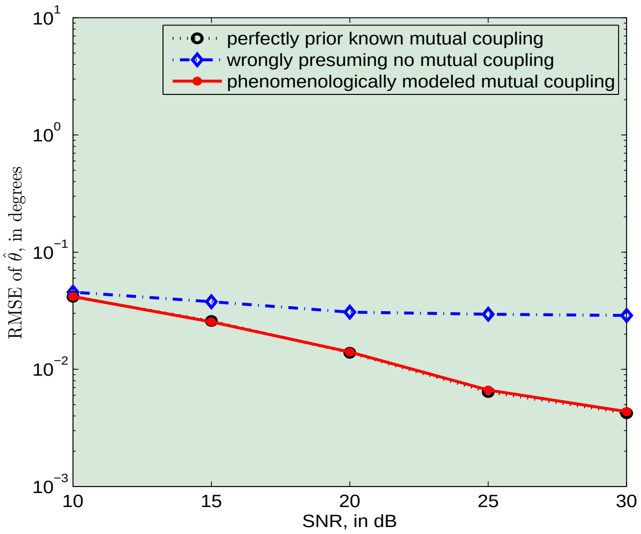

(a)

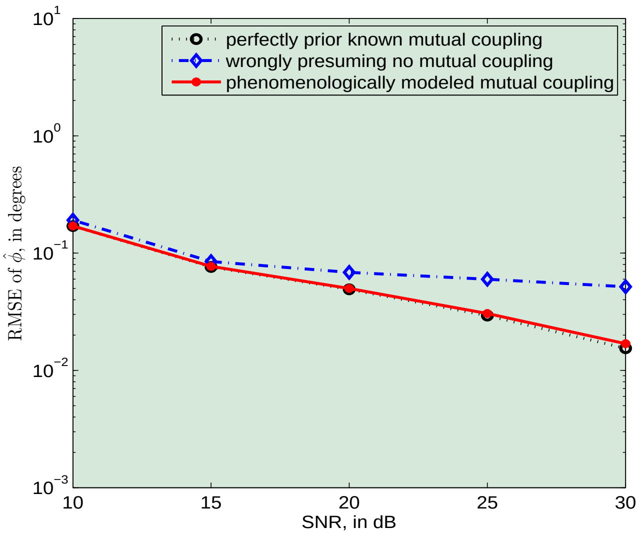

(b)

Figure 6.19: How the RMSE of (a) $\hat{\theta}$ and (b) $\hat{\phi}$ varies with the SNR. Here, $\frac{L}{\lambda} = 0.60$, $\varphi = 45°$, $\frac{\Delta}{\lambda} = 0.02$, $\theta = 15°$, $\phi = 53°$, $\gamma = 83°$, $\eta = 45°$.

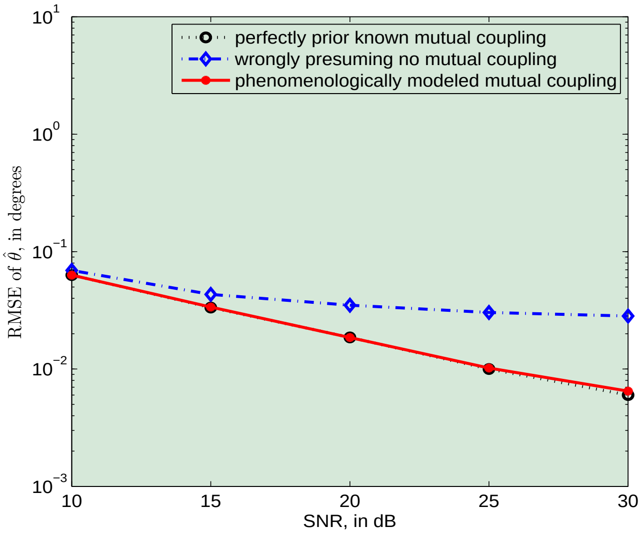

(a)

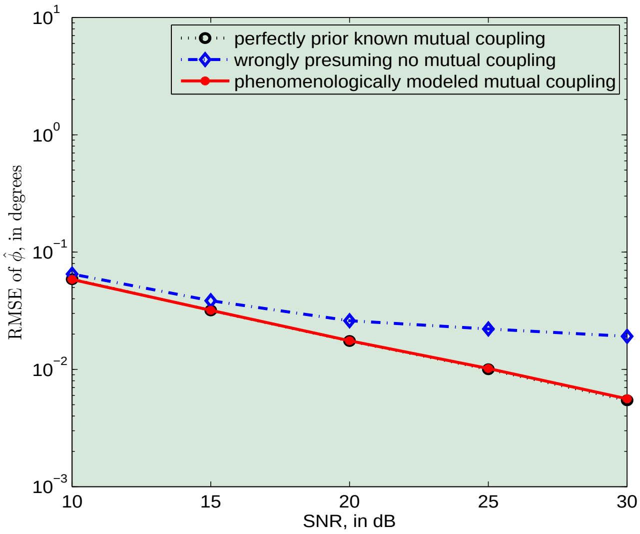

(b)

Figure 6.20: How the RMSE of (a) $\hat{\theta}$ and (b) $\hat{\phi}$ varies with the SNR. Here, $\frac{L}{\lambda} = 0.75$, $\varphi = 45°$, $\frac{\Delta}{\lambda} = 0.04$, $\theta = 48°$, $\phi = 56°$, $\gamma = 14°$, $\eta = -14°$.

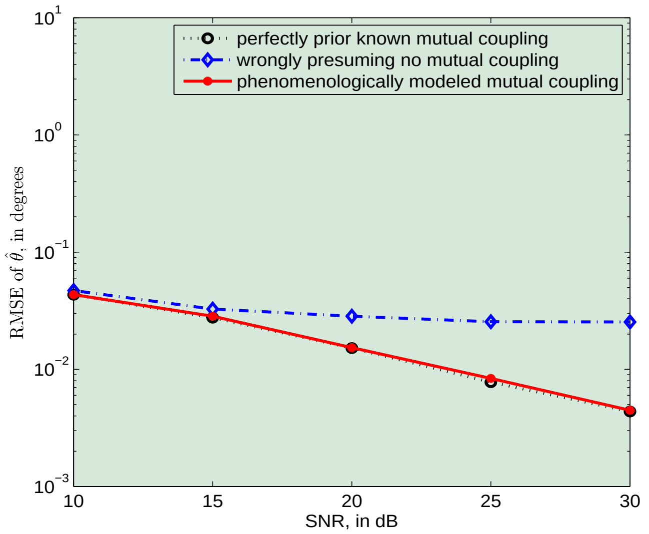

(a)

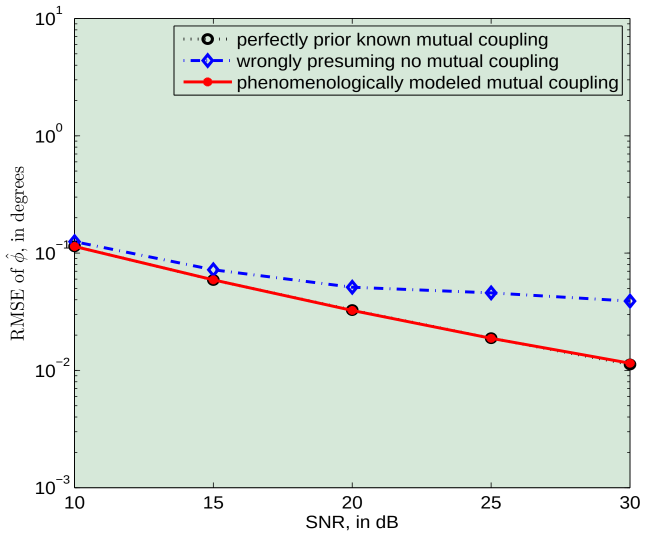

(b)

Figure 6.21: How the RMSE of (a) $\hat{\theta}$ and (b) $\hat{\phi}$ varies with the SNR. Here, $\frac{L}{\lambda} = 0.75$, $\varphi = 45°$, $\frac{\Delta}{\lambda} = 0.04$, $\theta = 22°$, $\phi = 40°$, $\gamma = 24°$, $\eta = -58°$.

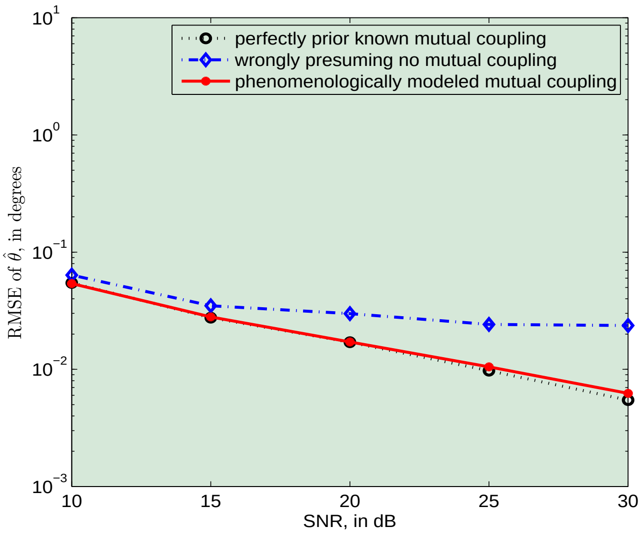

(a)

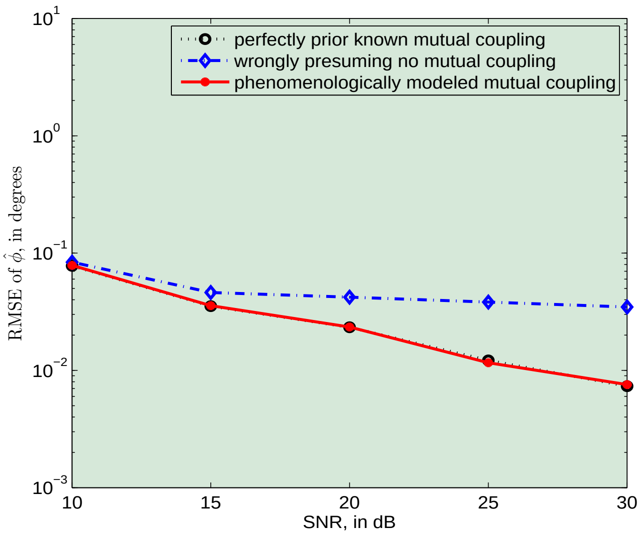

(b)

Figure 6.22: How the RMSE of (a) $\hat{\theta}$ and (b) $\hat{\phi}$ varies with the SNR. Here, $\frac{L}{\lambda} = 0.75$, $\varphi = 45^\circ$, $\frac{\Delta}{\lambda} = 0.04$, $\theta = 36^\circ$, $\phi = 48^\circ$, $\gamma = 14^\circ$, $\eta = -68^\circ$.

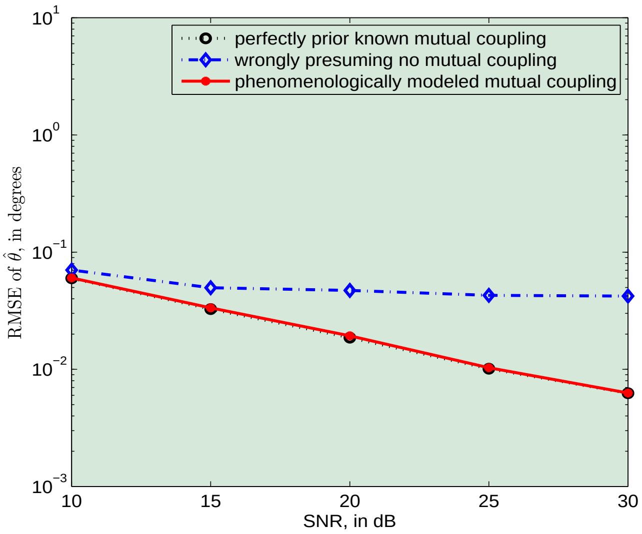

(a)

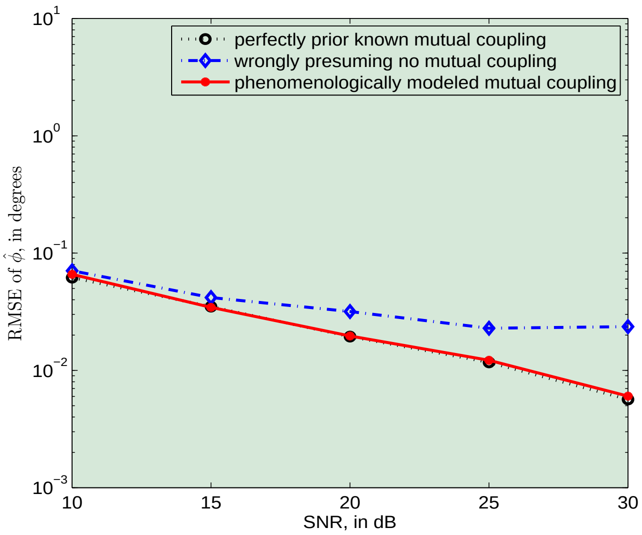

(b)

Figure 6.23: How the RMSE of (a) $\hat{\theta}$ and (b) $\hat{\phi}$ varies with the SNR. Here, $\frac{L}{\lambda} = 0.85$, $\varphi = 45°$, $\frac{\Delta}{\lambda} = 0.01$, $\theta = 46°$, $\phi = 36°$, $\gamma = 18°$, $\eta = -24°$.

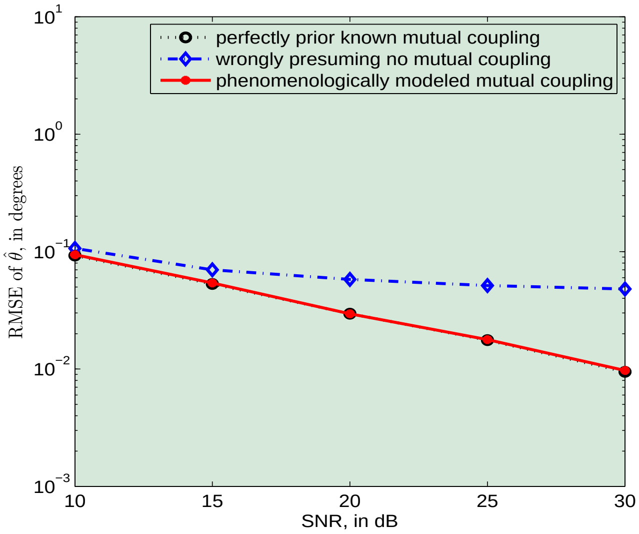

(a)

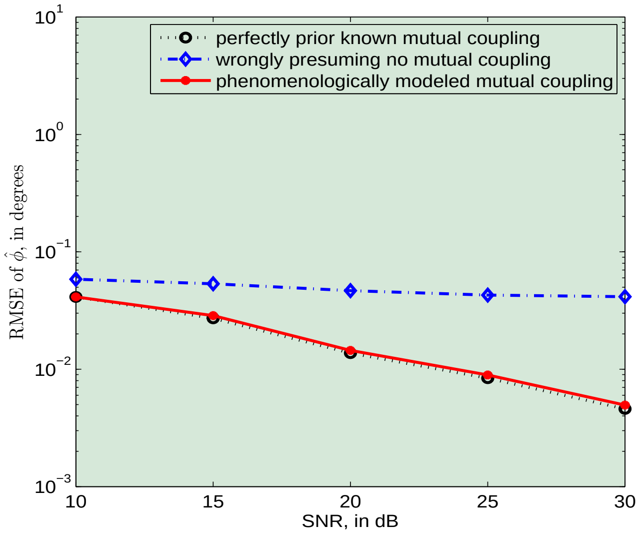

(b)

Figure 6.24: How the RMSE of (a) $\hat{\theta}$ and (b) $\hat{\phi}$ varies with the SNR. Here, $\frac{L}{\lambda} = 1.00$, $\varphi = 45°$, $\frac{\Delta}{\lambda} = 0.01$, $\theta = 65°$, $\phi = 38°$, $\gamma = 13°$, $\eta = -10°$.

Summary

The 23 pairs of $\hat{\theta}$ and $\hat{\phi}$ graphs shown here are just some of the many good graphs that were produced for the different settings of $\frac{L}{\lambda}$, φ and $\frac{\Delta}{\lambda}$. These graphs clearly show that the phenomenological models obtained can be used to estimate an incident source's direction-of-arrival, hence, attesting to the success of the phenomenological modeling.

Chapter 7

Conclusions and Future Work

The open literature's earlier analysis of dipole electromagnetics has produced equations of such intractable complexity, that little intuitive rule-of-thumb qualitative insights are obtained on how the mutual impedance magnitude of a pair of skewed co-centered cross-dipoles of equal length would vary with the dipoles' skew angle, the dipoles' common length, and the dipoles' separation. This work takes a "phenomenological" or "behavioral" approach of modeling, to least-squares-fit mutual impedance values to low-dimensional models. These new models are found useful in direction finding, despite these models' few degrees of freedom.

This dissertation was not only successful in obtaining the low-dimensional phenomenological models described above but having to demonstrate the usefulness of these models in estimating the source's direction-of-arrival is quite an accomplishment. The contribution of this research in pioneering phenomenological modeling approach in antenna array signal processing will be helpful in carrying out researches for other antenna array configurations in the future. This dissertation serves as an important reference for similar studies in modeling the mutual coupling or any other phenomena in antenna arrays.

For future work, the investigation on one dipole and one loop, collocated but perpendicular, labeled as "Cocentered Orthogonal Loop and Dipole" (COLD) array will be done. The "perpendicularity" here is between the dipole axis and the loop plane, *not* between the dipole axis and the loop axis. Hence, the electric dipole moment and the magnetic loop moment are aligned; and the COLD antenna pair retains omni-directionality on any plane perpendicular to the dipole axis.

Consider a co-centered pair of wire antennas, consisting of (i) an infinitesimally thin circular loop of radius R lying on the x-y Cartesian plane and a very thin, and (ii) a center-fed dipole of length L, skewed from the z-axis by a polar angle (a.k.a. zenith angle) of φ denotes the skew angle, and at an azimuth angle of β from the loop's feeding gap. Please refer to Figure 7.1.

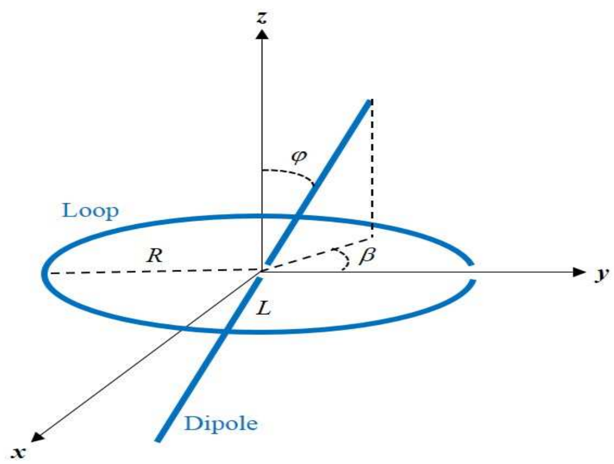

Figure 7.1: The spatial geometry of cocentered non-orthogonal loop and dipole.

The COLD antenna pair has been to estimate the arrival-angles and/or the polarization in [31, 56, 70, 80]. One reason for the COLD antenna pair's popularity is the absence of any mutual coupling between the dipole and the loop, *if* perpendicularity is maintained. Also, electrically small dipoles and magnetically small loops can be useful where the platform allows limited space, e.g. on a missile. In transmission the COLD array's overall polarization may be easily switched between circular polarization and linear polarization by adjusting the two feeding currents.

This work will characterize the mutual coupling resulting from a skewness away from perpendicularity between the dipole axis and the loop plane — how the 2×2 mutual impedance matrix's entries would vary with the dipole's length ($\frac{L}{\lambda}$), the loop's circumference ($\frac{C}{\lambda}$), the skew angle, etc.

Bibliography

[1] F. H. Murray, "Two Skew Antenna Wires, *Proceedings of the Institute of Radio Engineers*, vol. 21, no. 1, pp. 154-158, January 1933.

[2] G. Brown, "The turnstile, *Electron.*, vol. 9, pp. 1417, April 1936.

[3] H. W. Andrews, *The Collinear Antenna Array: Theory and Measurements*, Defense Technical Information Center, 1953.

[4] J. Czyz, "Impedancje wzajemne w plaskich ukladach antenowych," *Rozprawy Elektrotecltniczne*, vol. 3, no. 1, pp. 139-166, 1957.

[5] H. C. Baker and A. H. LaGrone, "Digital computation of the mutual impedance between thin dipoles," *IRE Transactions on Antennas and Propagation*, vol. 10, no. 2, pp. 172-178, March 1962.

[6] R. F. Harrington *Field Computation by Method of Moments*, Macmillan, 1968.

[7] J. H. Richmond and N. H. Geary, "Mutual impedance between coplanar-skew dipoles," *IEEE Transactions on Antennas and Propagation*, vol. 18, no. 3, pp. 414416, May 1970.

[8] J. H. Richmond, "Coupled linear antennas with skew orientation," *IEEE Transactions on Antennas and Propagation*, vol. 18, no. 5, pp. 694696, September 1970.

[9] R. Kalafus, "Broad-band dipole design using the method of moments," *IEEE Transactions on Antennas and Propagation*, vol. 19, no. 6, pp. 771-773, November 1971.

[10] M. C. Elias & C. T. Carson, "Direct analysis of folded dipole by method of moments," *Electronics Letters*, vol. 9, no. 22, pp. 520-521, November 1973.

[11] J. B. Andersen, H. A. Lessow, and H. Schjaer-Jacobsen "Coupling between minimum scattering antennas," *IEEE Transactions on Antennas and Propagation*, vol. 22, no. 6, pp. 832835, November 1974.

[12] J. H. Richmond and N. H. Geary, "Mutual impedance of nonplanar-skew sinusoidal dipoles," *IEEE Transactions on Antennas and Propagation*, vol. 23, no. 3, pp. 412414, May 1975.

[13] O. R. Schmidt, "A signal subspace approach to multiple emitter location and spectral estimation, Stanford Univ., Stanford, CA, 1981.

[14] I. Gupta & A. Ksienski, "Effect of mutual coupling on the performance of adaptive arrays," *IEEE Transactions on Antennas and Propagation*, vol. 31, no. 5, pp. 785-791, September 1983.

[15] A. E. Gera, "A simplified computational procedure for the analysis of planar arrays," *IEEE Transactions on Antennas and Propagation*, vol. 32, no. 6, pp. 647-651, June 1984.

[16] R. O. Schmidt, "Multiple emitter location and signal parameter estimation," *IEEE Transactions on Antennas and Propagation*, vol. 34, no. 3, pp. 276-280, March 1986.

[17] R. Roy & T. Kailath, "ESPRIT-Estimation of Signal Parameters Via Rotational Invariance Techniques," *IEEE Transactions on Acoustics, Speech, and Signal Processing*, vol. 37, no. 7, pp. 984-995, July 1989.

[18] B. Himed & D. D. Weiner, "Compensation of mutual coupling effects for the ESPRIT algorithm," *IEEE Antennas and Propagation Society International Symposium*, vol. 2, pp. 966-969, 1989.

[19] E. E. Altshuler, "Self- and mutual impedances of traveling-wave linear antennas," *IEEE Transactions on Antennas and Propagation*, vol. 37, no. 10, pp. 1312-1316, October 1989.

[20] B. Himed & D. D. Weiner, "A generalized treatment of mutual coupling compensation for ESPRIT," *IEEE International Symposium on Circuits and Systems*, vol. 1, pp. 296-299, 1989.

[21] R. Roy & T. Kailath, "ESPRIT - estimation of signal parameters Via rotational invariance techniques," *IEEE Transactions on Acoustics, Speech, and Signal Processing*, vol. 37, no. 7, pp. 984-995, July 1989.

[22] B. Himed & D. D. Weiner, "Compensation for mutual coupling effects in direction finding," *IEEE International Conference on Acoustics, Speech, and Signal Processing*, vol. 5, pp. 2631-2634, 1990.

[23] B. Friedlander & A. J. Weiss, "Direction finding in the presence of mutual coupling," *IEEE Transactions on Antennas and Propagation*, vol. 39, no. 3, pp. 273-284, March 1991.

[24] *IEEE Standard Definitions of Terms for Antennas*, IEEE Standard 145, 1993.

[25] H. Yavuz & O. M. Buyukdura, "Rigorous analysis of finite rectangular arrays with simultaneous integral equations," *IEEE Antennas and Propagation Society International Symposium*, vol. 3, pp. 1262-1265, 1993.

[26] C. Yang & Y. Z. Ruan, "Eigenvalues of covariance matrix of adaptive array with mutual coupling and two correlated sources present," *IEEE Antennas and Propagation Society International Symposium*, vol. 2, pp.706-709, 1993.

[27] P. Petre & T. K. Sarkar, "Planar near-field to far-field transformation using an array of dipole probes," *IEEE Transactions on Antennas and Propagation*, vol. 42, no. 4, pp. 534-537, April 1994.

[28] Jian Li, "On polarization estimation using a crossed-dipole array," *IEEE Transactions on Signal Processing*, vol. 42, no. 4, pp. 977-980, Apr 1994.

[29] H. Yavuz & O. M. Buyukdura, "Mutual coupling effects of finite rectangular phased arrays," *Mediterranean Electrotechnical Conference*, vol. 2, pp. 418-421 , 1994.

[30] T. K. Sarkar & O. Pereira, "Using the matrix pencil method to estimate the parameters of a sum of complex exponentials, *IEEE Antennas and Propagation Magazine*, vol. 37, no. 1, pp. 48-55, February, 1995.

[31] J. Li, P. Stoica & D. Zheng, "Efficient direction and polarization estimation with a COLD array," *IEEE Transactions on Antennas and Propagation*, vol. 44, no. 4, pp. 539-547 April 1996. 33

[32] K. E. Schmidt, "Simplified mutual impedance of nonplanar skew dipoles," *IEEE Transactions on Antennas and Propagation*, vol. 44, no. 9, pp. 12981299, September 1996.

[33] S. Lundgren, "A study of mutual coupling effects on the direction finding performance of ESPRIT with a linear microstrip patch array using the method of moments," *Antennas and Propagation Society International Symposium*, vol. 2, pp. 1372-1375, 1996.

[34] C. A. Balanis, *Antenna Theory: Analysis and Design*, Hoboken, New Jersey, USA: Wiley, 1997.

[35] A. R. Adams, R. D. Pollard & C. M. Snowden, "A method-of-moments study of strip dipole antennas in rectangular waveguide," *IEEE Transactions on Microwave Theory and Techniques*, vol. 45, no. 10, pp. 1756-1766, October 1997.

[36] S. K. Shin, H. Kim, C. R. Giles, M. Zirngibl & Y. C. Chung, "Phenomenological model of the integrated multifrequency laser", Proceedings of Optical Fiber Communication Conference, pp. 215-216, 1997.

[37] J. E. F. del Rio, O. M. Conde-Portilla & M. F. Catedra, "Estimating azimuth and elevation angles when mutual coupling is significant," *Antennas and Propagation Society International Symposium*, vol. 1, pp. 215-218, 1998.

[38] T. Svantesson, "The effects of mutual coupling using a linear array of thin dipoles of finite length," *IEEE Signal Processing Workshop on Statistical Signal and Array Processing*, pp. 232-235, 1998.

[39] M. A. Holdaway & T. T. Helfer, "Interferometry Array Design," *Synthesis Imaging in Radio Astronomy II*, vol. 180, pp. 537-563, 1999.

[40] D. H. Werner & R. J. Allard, "Accurate modelling of anti-resonant dipole antennas using the method of moments," *Electronics Letters*, vol. 35, no. 1, pp. 1-2, 7 January 1999.

[41] T. Svantesson, "Modeling and estimation of mutual coupling in a uniform linear array of dipoles," *IEEE International Conference on Acoustics, Speech, and Signal Processing*, vol. 5, pp. 2961-2964, 1999.

[42] Le-Wei Li, Chan-Ping Lim & Mook-Seng Leong, "Method of moments analysis of electrically large circular-loop antennas: non-uniform currents," *IEEE Antennas and Propagation Society International Symposium*, vol.4, pp. 2542-2545, 1999.

[43] T. Svantesson, "Mutual coupling compensation using subspace fitting," *IEEE Sensor Array and Multichannel Signal Processing Workshop*, pp. 494-498, 2000.

[44] J. Cortes & J. P. Martinaud, "Matrix times vector multiplication based on Floquet-Bloch decomposition in the context of large antenna arrays. Application to finite-element partitionings," *IEEE Antennas and Propagation Society International Symposium*, vol. 2, pp. 193-196, 2003.

[45] R. W. Kindt & J. L. Volakis, "The array decomposition-fast multipole method," *IEEE Antennas and Propagation Society International Symposium*, vol. 4, pp. 3-6, 2003.

[46] B. Wang, Y. Wang & H. Chen, "A robust DOA estimation algorithm for uniform linear array in the presence of mutual coupling." *IEEE International Conference on Antenna Theory and Techniques*, vol. 1, pp. 924-927, 2003.

[47] M. Amin and R. Cahill, "Mutual coupling effects between coplanar crossed skew dipoles," *High Frequency Postgraduate Student Colloquium*, pp. 107-110, 2003.

[48] F. I. Tseng & J. Venkataraman, "Optimization for adaptive antenna arrays with mutually coupled elements via spatially smoothed ESPRIT," IEEE Topical Conference on Wireless Communication Technology, pp. 376-377, 2003.

[49] B.-h. Wang, Y.-l. Wang, W.-H. & H. Chen, "A robust DOA estimation algorithm for uniform linear array in the presence of mutual coupling," *IEEE Antennas and Propagation Society International Symposium*, vol. 3, pp. 924-927, 2003.

[50] Le-Wei Li, Mui-Seng Yeo & Mook-Seng Leong, "Method of moments analysis of EM fields in a multilayered spheroid radiated by a thin circular loop antenna," *IEEE Transactions on Antennas and Propagation*, vol. 52, no. 9, pp. 2391-2402, September 2004.

[51] M. Amin and R. Cahill, "Mutual impedance between two dipole antennas fed by single source," *Microwave and Optical Technology Letters*, vol. 42, no. 3, pp. 187-189, August 2004.

[52] T. T. Zhang & H. T. Hui, "Direction of arrival estimation using ESPRIT with mutual coupling compensation," *IEE Proceedings: Science, Measurement and Technology*, vol. 151, no. 6, pp. 476-478, November 2004.

[53] T. T. Zhang, H. T. Hui & Y. L. Lu, "Compensation for the mutual coupling effect in the ESPRIT direction finding algorithm by using a more effective method," *IEEE Transactions on Antennas and Propagation*, vol. 53, no. 4, pp. 1552-1555, April 2005.

[54] S. Wei, D. Goeckel & R. Janaswamy, "On the asymptotic capacity of MIMO systems with antenna arrays of fixed length," *IEEE Transactions on Wireless Communications*, vol. 4, no. 4, pp. 1608-1621, July 2005.

[55] S. K. Khamas, G. G. Cook & S. M. Lani, "Efficient method of moments analysis of a printed wire loop antenna with dielectric superstrate cover," *IEE Proceedings - Microwaves, Antennas and Propagation*, vol. 152, no. 5, pp. 337-339, October 2005.

[56] J.-C. Huang, Y.-W. Shi & J.-W. Tao, "Closed-form estimation of DOA and polarization for multisource with a uniform circular array," *International Conference on Machine Learning and Cybernetics*, vol. 7, pp. 4469-4474, 2005.

[57] C. Qi, Y. Wang, Y. Zhang & H. Chen, "A decoupling DOA estimation and self-calibration algorithm for circular antenna array," *IEEE Antennas and Propagation Society International Symposium*, vol. 2B, pp. 366-369, 2005.

[58] Z. Huang, C. A. Balanis & C. R. Birtcher, "Mutual Coupling Compensation in UCAs: Simulations and Experiment," *IEEE Transactions on Antennas and Propagation*, vol. 54, no. 11, pp. 3082-3086, November 2006.

[59] A. Al-Kabi, M. E. Bialkowski & J. Homer, "Performance comparison between uniformly and nonuniformly spaced adaptive antennas with respect to tolerance to pointing errors," *Microwave and Optical Technology Letters*, vol. 48, no. 11, pp. 2233-2237, November 2006.

[60] H. Boche, A. Bourdoux, J. V. Fonollosa, T. Kaiser, A. Molisch & W. Utschick, "Smart Antennas:State of the Art", *IEEE Vehicular Technology Magazine*, pp.8-17, March 2006.

[61] S. Hwang, S. Burintramart, T. K. Sarkar & S. R. Best, "Direction of arrival (DOA) estimation using electrically small tuned dipole antennas," *IEEE Transactions on Antennas and Propagation*, vol. 54, no. 11, pp. 3292-3301, November 2006.

[62] X. Xu, Z. Ye, Y. Zhang &C. Chang, "A Deflation Approach to Direction of Arrival Estimation for Symmetric Uniform Linear Array," *IEEE Antennas and Wireless Propagation Letters*, vol. 1, no. 1, pp. 486-489, 2006.

[63] X. Guo, Q. Wan & W. Yang, "Parameters estimation of coherently distributed sources in the presence of mutual coupling," *International Conference on Signal Processing*, vol. 1, 2006.

[64] F. Sellone & A. Serra, "An iterative algorithm for the compensation of Toeplitz mutual coupling in uniform and linear arrays," *Digital Signal Processing Workshop*, pp. 438-443, 2006.

[65] Y. Inoue & H. Arai, "Effect of mutual coupling and manufacturing error of array for DOA estimation of ESPRIT algorithm," *Electronics and Communications in Japan*, part 1, vol. 89, no. 9, pp. 68-76, 2006.

[66] Z. Huang, C. A. Balanis & C. R. Birtcher, "Mutual Coupling in Beamforming with Circular Array," *IEEE Antennas and Propagation Society International Symposium*, pp. 4785-4788, 2006.

[67] G. Shuyan, C. Hui, W. Yongliang & M. Cangzhen, "A Novel Algorithm for Estimating DOA of Coherent Signals on Uniform Circular Array," *International Conference on Radar*, pp. 1-4, 2006.

[68] F. Sellone & A. Serra, "A novel online mutual coupling compensation algorithm for uniform and linear arrays," *IEEE Transactions on Signal Processing*, vol. 55, no. 2, pp. 560-573, February 2007.

[69] L. Xiaohua, Z. Jianjiang, L. Hailin & C. Wenqi, "Compensation for the mutual coupling effect for the ESPRIT algorithm in single-snapshot array processing," *Journal of Electronics (China)*, vol. 24, no. 5, pp. 662-667, September 2007.

[70] C.-H. Lin, W.-H. Fang, W.-S. Yang & J.-D. Lin, "SPS-ESPRIT for joint DOA and polarization estimation with a COLD array," *IEEE Antennas and Propagation Society International Symposium*, pp. 1136-1139, 2007.

[71] K. A. Griffith & I. J. Gupta, "Reduced order antenna array calibration," *IEEE Antennas and Propagation Society International Symposium*, pp. 1100-1103, 2007.

[72] Y. Zhang, Q. Wan, A. Huang & W.-L. Yang, "Observation data based DOA estimation with uncalibrated antenna array in perspective of sparse solution finding," *IEEE Region 10 Conference*, 2007.

[73] K. A. Bakshi, A. V. Bakshi & U. A. Bakshi, *Antennas and Wave Propagation*, Shanewar Peth, Pune, India: Technical Publications Pune, 2008.

[74] Y. Huang & K. Boyle, *Antennas: From Theory to Practice*, West Sussex, United Kingdom: John Wiley & Sons Ltd, 2008.

[75] J. Foutz, A. Spanias & M. Banavar, *Narrowband Direction of Arrival Estimation for Antenna Arrays* , Morgan & Claypool Publishers, 2008.

[76] H. Shin, M. Z. Win & M. Chiani, "Asymptotic statistics of mutual information for doubly correlated MIMO channels," *IEEE Transactions on Wireless Communications*, vol. 7, no. 2, pp. 562-573, February 2008.

[77] Z. Ye & C. Liu, "2-D DOA estimation in the presence of mutual coupling," *IEEE Transactions on Antennas and Propagation*, vol. 56, no. 10, pp. 3150-3158, October 2008.

[78] S. Shastri, K. Shah & R. Shekhar, "Modified circular polarized loop antenna," *IEEE International Conference on Recent Advances in Microwave Theory & Applications*, pp. 934-936, 2008.

[79] Y. Wu & H. C. So, "Simple and Accurate Two-Dimensional Angle Estimation for a Single Source With Uniform Circular Array," *IEEE Antennas and Wireless Propagation Letters*, vol. 7, pp. 78-80, 2008.

[80] J. Tao, H. Xu & J.-W. Tao, "Closed-form direction finding for multiple sources based on uniform circular arrays with trimmed vector sensor," *World Congress on Intelligent Control and Automation*, pp. 2392-2395, 2008.

[81] M. I. Ahmad, Zhiwen Liu & Yougen Xu, "Minimum variance beamforming using polarization sensitive array," *IEEE Singapore International Conference on Communication Systems*, 2008, pp. 489-492.

[82] K. Velten, *Mathematical Modeling and Simulation: Introduction for Scientists and Engineers* , Weinheim, Germany: WILEY-VCH Verlag GmbH & Co. KGaA, 2009

[83] Z. Ye, J. Dai, X. Xu & X. Wu, "DOA estimation for uniform linear array with mutual coupling," *IEEE Transactions on Aerospace and Electronic Systems*, vol. 45, no. 1, pp. 280-288, January 2009.

[84] Z. Ye, Y. Zhang, X. Xu & C. Liu, "Direction of arrival estimation for uncorrelated and coherent signals with uniform linear array, *IET Radar, Sonar & Navigation*, vol. 3, no. 2, pp. 144-154, February 2009.

[85] B. Q. Wu & K. M. Luk, "A Broadband Dual-Polarized Magneto-Electric Dipole Antenna With Simple Feeds," *IEEE Antennas and Wireless Propagation Letters*, vol. 8, pp. 60-63, 2009.

[86] C. H. Lin, W. H. Fang and Y. T. Chen, "Efficient joint two-dimensional angle and polarization estimation with crossed dipoles," *International Conference on Information, Communications and Signal Processing*, 2009, pp. 1-5.

[87] H. Yordanov, M. T. Ivrlac, P. Russer & J. A. Nossek, "Arrays of isotropic radiators - a field-theoretic justification, *International ITG Workshop on Smart Antennas*, pp. 32-35, 2009.

[88] V. V. Zaharov, A. L. Lobaina, J. L. Rodriguez, & R. A. Soto, "Fast mutual coupling compensation algorithm for large adaptive antenna array, *IEEE International Midwest Symposium on Circuits and Systems*, pp. 586-589, 2009.

[89] I. Radnovi, A. Nei & B. Milovanovi, "A New Type of Turnstile Antenna," *IEEE Antennas and Propagation Magazine*, vol. 52, no. 5, pp. 168-171, October 2010.

[90] Y. H. Ko, C. H. Park, W. Y. Yang & Y. S. Cho, "Cell searching and DoA estimation methods for OFDM-based mobile relay stations with a ULA," *IEEE GLOBECOM Workshops*, pp. 64-68, 2010.

[91] H. Kawakami, "A Review of and New Results for Broadband Antennas for Digital Terrestrial Broadcasting: The Modified Batwing Antenna," *IEEE Antennas and Propagation Magazine*, vol. 52, no. 6, pp. 78-88, December 2010.

[92] R. C. Hansen, *Small Antenna Handbook*, Hoboken, New Jersey, USA: John Wiley & Sons, 2011.

[93] W. L. Stutzman & G. A. Thiele, *Antenna Theory and Design*, Hoboken, New Jersey, USA: Wiley, 2011.

[94] B. Liao & S.C. Chan, "DOA estimation of coherent signals for uniform linear arrays with mutual coupling," *IEEE International Symposium on Circuits and Systems*, pp. 377-380, 2011.

[95] S. R. Best, "Mutual coupling between orthogonal electrically small dipole antennas," *European Conference on Antennas and Propagation*, pp. 1663-1666, 2011.

[96] X. Hu, Y. Wang & H. Chen, "2-dimensional arrival angle estimation and self-calibration algorithm for L-shaped array in the presence of mutual coupling," *International Conference on Intelligent Computation Technology and Automation*, vol. 2, pp. 319-322, 2011.

[97] A. Azarbar, G. R. Dadashzadeh & H. R. Bakhshi, "Non-sensitive matrix pencil method against mutual coupling, *IEICE Electronics Express*, vol. 8, no. 6, pp. 318-324, May 2011.

[98] Y. Wu, H. Chen & Y. Chen, "A method of 2-D DOA estimation of coherent signals based on uniform circular array via spatial smoothing," *International Conference on Radar*, pp. 312-314, 2011.

[99] X. Gou, Y. Xu, Z. Liu & X. Gong, "Quaternion-Capon beamformer using crossed-dipole arrays," *IEEE International Symposium on Microwave, Antenna, Propagation and EMC Technologies for Wireless Communications*, 2011, pp. 34-37.

[100] B. Liao, Z.-G. Zhang & S.-C. Chan, "DOA estimation and tracking of ULAs with mutual coupling," *IEEE Transactions on Aerospace and Electronic Systems*, vol. 48, no. 1, pp. 891-905, January 2012.

[101] M. Costa, A. Richter & V. Koivunen, "DoA and Polarization Estimation for Arbitrary Array Configurations," *IEEE Transactions on Signal Processing*, vol. 60, no. 5, pp. 2330-2343, May 2012.

[102] P. Yang, F. Yang, Z. P. Nie, H. J. Zhou, B. Li & X. F. Tang, "Fast 2-D DOA and polarization estimation using arbitrary conformal antenna array,", *Progress in Electromagnetics Research C*, vol. 25, pp.119-132, 2012.

[103] X. Yuan, K. T. Wong, and K. Agrawal, "Polarization estimation With a dipole-dipole pair, a dipole-loop pair, or a loop-loop pair of various orientations," *IEEE Transactions on Antennas and Propagation*, vol. 60, no. 5, pp. 2442-2452, May 2012.

[104] J. H. Han and N. H. Myung, "Exact and simple calculation of mutual impedance for coplanar-skew dipoles," *Electronics Letters*, vol. 48, no. 8, April 12, pp. 423-425, 2012.

[105] J. H. Han, W. Y. Song, K. S. Oh, and N. H. Myung, "Simple formula and its exact analytic solution of mutual impedance for nonplanar-skew dipoles," *Progress in Electromagnetics Research*, vol. 132, pp. 551-570, 2012.

[106] B. Liao & S.C. Chan, "Adaptive beamforming for uniform linear arrays with unknown mutual coupling," *IEEE Antennas and Wireless Propagation Letters*, vol. 11, pp. 464-467, 2012.

[107] K. Ichige H. Li, & H. Arai, "SURE: SimUltaneous Root Extraction method for DOA estimation of coherent sources by ULA," *IEEE Sensor Array and Multichannel Signal Processing Workshop*, pp. 293-296, 2012.

[108] H.-b. Li, Y.-d. Guo, J. Gong & J. Jiang, "Mutual coupling self-calibration algorithm for uniform linear array based on ESPRIT, *International Conference on Consumer Electronics, Communications and Networks*. pp. 3323-3326, 2012.

[109] R. J. Weber & Y. Huang, "Performance analysis of direction of arrival estimation with a uniform circular array," *IEEE Aerospace Conference*, pp. 1-7, 2012.

[110] S. Chandran(Ed.), *Adaptive Antenna Arrays: Trends and Applications*, Springer, 2013.

[111] H. Singh, H. L. Sneha & R. M. Jha, "Mutual Coupling in Phased Arrays : A Review," *International Journal on Antennas and Propagation*, vol. 2013, no. 5, April 2013.

[112] J.-G. Hong, W.-H. Ahn & B.-S. Seo, "Compensation of mutual coupling in an antenna array for direction of arrival estimation," *International Conference on Advanced Communication Technology*, pp. 599-603, 2013.

[113] J.-H. Han, W.-Y. Song, K.-S. Oh, and N.-H. Myung, "Analytical derivation of mutual impedance between two arbitrarily located and slanted dipoles using effective length vector," *Asia-Pacific Microwave Conference*, pp. 401-403, 2013.

[114] H. Li & P. Wei, "DOA estimation in an antenna array with mutual coupling based on ESPRIT," *International Workshop on Microwave and Millimeter Wave Circuits and System Technology*, pp. 86-89, 2013.

[115] Y. Li, J. Q. Zhang, B. Hu, H. Zhou & X. Y. Zeng, "A novel 2-D quaternion ESPRIT for joint DOA and polarization estimation with crossed-dipole arrays," *IEEE International Conference on Industrial Technology*, pp. 1038-1043, 2013.

[116] S. Akkar, F. Harabi & A. Garsallah, "Directions of arrival estimation with planar antenna arrays in the presence of mutual coupling," *International Journal of Electronics*, vo. 100, no. 6, pp. 818-836, 2013.

[117] I. J. Yoon & H. Ling, "Design of an electrically small circularly polarised turnstile antenna and its application to near-field wireless power transfer," *IET Microwaves, Antennas & Propagation*, vol. 8, no. 5, pp. 308-314, April 2014.

[118] C. H. Lin & W. H. Fang, "Efficient estimation of signal parameters via rotational invariance technique-based algorithm with automatic pairing for two-dimensional angle and polarisation estimation using crossed dipoles," *IET Signal Processing*, vol. 8, no. 4, pp. 309-319, June 2014.

[119] B. Liao & S.C. Chan, "A cumulant-based method for direction finding in uniform linear arrays with mutual coupling," *IEEE Antennas and Wireless Propagation Letters*, vol. 13, pp. 1717-1720, 2014.

[120] W. Si, D. Wu, L. Liu & X. Qu, "Direction finding with gain/phase errors and mutual coupling errors in the presence of auxiliary sensors," *Mathematical Problems in Engineering*, vol. 2014, pp. 1-12, 2014.

[121] H. Li, Q. Wei, J. Jiang & H. Tian, "Angle estimation and self-calibration for bistatic MIMO radar with mutual coupling of transmitting and receiving arrays," *IEEE Workshop on Electronics, Computer and Applications*, pp. 354-357, 2014.

[122] Y. Iwabuchi, H. Li & K. Ichige, "Direction-of-arrival estimation of coherent sources for ULA based on the relation between array covariance matrix elements," *6th International Symposium on Communications, Control and Signal Processing*, pp. 648-651, 2014.

[123] F. Liu, H. Li, W. Xia & Y. Wang, "A DOA and polarization estimation method using a spatially non-collocated vector sensor array," *IEEE China Summit & International Conference on Signal and Information Processing*, pp. 763-767, 2014.

[124] I. Park, S. X. Ta, J. J. Han & R. W. Ziolkowski, "Applications of circularly polarized crossed dipole antennas," *International Workshop on Antenna Technology: Small Antennas, Novel EM Structures and Materials, and Applications*, pp. 2-4, 2014.

[125] F. B. Gross, *Smart Antennas with MATLAB*, New York, USA: McGraw-Hill Education, 2015.

[126] Y. Tian, X. Sun & S. Zhao, "Sparse-reconstruction-based direction of arrival, polarisation and power estimation using a cross-dipole array," *IET Radar, Sonar & Navigation*, vol. 9, no. 6, pp. 727-731, July 2015.

[127] S. X. Ta, I. Park & R. W. Ziolkowski, "Crossed Dipole Antennas: A review," *IEEE Antennas and Propagation Magazine*, vol. 57, no. 5, pp. 107-122, October 2015.

[128] K. Saurav, D. Sarkar, A. Singh & K. V. Srivastava, "Multiband Circularly Polarized Cavity-Backed Crossed Dipole Antenna," *IEEE Transactions on Antennas and Propagation*, vol. 63, no. 10, pp. 4286-4296, October 2015.

[129] A. A. Kumar, S. G. Razul & C. M. S. See, "Spectrum blind reconstruction and direction-of-arrival estimation at sub-Nyquist sampling rates with uniform linear array," *IEEE International Conference on Digital Signal Processing*, pp. 670-674, 2015.

[130] Y. Liu & R. D. Gitlin, "A phenomenological path loss model of the in vivo wireless channel," *IEEE Wireless and Microwave Technology Conference*, pp. 1-3, 2015.

[131] Y. I. Wu, G. P. Arada, K. T. Wong & W.-Y. Tam, "Electromagnetic coupling matrix modeling and *ESPRIT*-based direction finding – A case study using a uniform linear array of identical dipoles," *IET International Conference on Intelligent Signal Processing*, pp. 1-5, 2015.

[132] C. I. Paez Rueda & R. Bustamante Miller, "A New Approximate Closed Solution for Small Dipole Antenna with Method of Moments," *IEEE Latin America Transactions*, vol. 14, no. 4, pp. 1562-1569, April 2016.

[133] F. Yan, Y. Shen, M. Jin & X. Qiao, "Computationally efficient direction finding using polynomial rooting with reduced-order and real-valued computations,"

Journal of Systems Engineering and Electronics, vol. 27, no. 4, pp. 739-745, August 2016.

[134] K. Wang, L. Wang, J. R. Shang & X. X. Qu, "Mixed Near-Field and Far-Field Source Localization Based on Uniform Linear Array Partition," *IEEE Sensors Journal*, vol. 16, no. 22, pp. 8083-8090, November 2016.

[135] S. Li, R. He, B. Lin, & F. Sun, "DOA estimation based on sparse representation of the fractional lower order statistics in impulsive noise," *IEEE/CAA Journal of Automatica Sinica*, vol.PP, no.99, pp.1-9, December 2016.

[136] L. Wan, G. Han, L. Shu, S. Chan & T. Zhu, "The Application of DOA Estimation Approach in Patient Tracking Systems with High Patient Density," *IEEE Transactions on Industrial Informatics*, vol. 12, no. 6, pp. 2353-2364, December 2016.

[137] J. Lin, X. Ma, S. Yan and C. Hao, "Time-Frequency Multi-Invariance ESPRIT for DOA Estimation," *IEEE Antennas and Wireless Propagation Letters*, vol. 15, pp. 770-773, 2016.

[138] H. M. Elkamchouchi, D. A. E. Mohamed, O. G. Mohamed & W. A. E. Ali, "Robust doa estimation and data detection for mobile communication in multipath environment," *4th International Conference on Cloud Computing and Intelligence Systems*, pp. 293-297, 2016.

[139] Chao-Yong Liu & Qing-Xin Chu, "Omnidirectional circularly polarized antenna based on crossed dipoles," *IEEE International Conference on Microwave and Millimeter Wave Technology*, pp. 731-733, 2016.

[140] Y. I. Wu, G. P. Arada, W.-Y. Tam & K. T. Wong , "Mis-modeling & Mis-correction of Mutual Coupling in an Antenna Array – A Case Study in the Context of Direction Finding Using a Linear Array of Identical Dipoles," *IEEE International Conference on Signal and Image Processing*,pp. 447-451, 2016.

[141] K. T. Wong, Y. Song, C. J. Fulton, S. Khan, and W.-Y. Tam, " 'Long' dipoles in a collocated/orthogonal triad – for direction finding or polarization estimation," accepted for publication by the *IEEE Transactions on Antennas and Propagation.*

Appendix A

Candidate Models for $|Z_{1,2}| = |Z_{2,1}|$

A.1 Model 1

$$
\begin{aligned}
|Z_{1,2}| &= |Z_{2,1}| \\
&\approx \left(a_1 + a_2 e^{\left(-\frac{\Delta}{\lambda} + a_3 \frac{L}{\lambda}\right)}\right) |\varphi|,
\end{aligned} \tag{A.1}
$$

where

$$
\begin{aligned}
a_1 &:= 31.9218 \\
a_2 &:= 0.0789 \\
a_3 &:= 10.9603.
\end{aligned}
$$

$|Z_{1,2}| = |Z_{2,1}|$ has values over several orders of magnitude. Hence, the latter would overweight those support regions of $\left\{\varphi, \frac{L}{\lambda}, \frac{\Delta}{\lambda}\right\}$ where $|Z_{1,2}| = |Z_{2,1}|$ is very large, thereby poorly fitting other regions of $\left\{\varphi, \frac{L}{\lambda}, \frac{\Delta}{\lambda}\right\}$ where $|Z_{1,2}| = |Z_{2,1}|$ is small. Specifically, the would-be-underweighted support region is where $\frac{L}{\lambda}$ increases toward unity and where $\frac{\Delta}{\lambda}$ decreases toward zero. Also, $|Z_{1,2}| = a_1 \neq 0$ even when $\frac{\Delta}{\lambda} \to \infty$. Hence, this model is unacceptable.

A.2 Model 2

$$
\begin{aligned}
|Z_{1,2}| &= |Z_{2,1}| \\
&\approx \left(a_1 + a_2 e^{-\frac{\Delta}{\lambda}} \left(\frac{L}{\lambda} \right)^{a_3} \right) |\sin\varphi|,
\end{aligned}
\tag{A.2}
$$

where

$$
\begin{aligned}
a1 &:= 42.1133 \\
a_2 &:= 4870.5 \\
a_3 &:= 10.0884.
\end{aligned}
$$

This model was not chosen due to the same reasons as in the candidate model (A.1).

A.3 Model 3

$$
\begin{aligned}
|Z_{1,2}| &= |Z_{2,1}| \\
&\approx \left(a_1 + a_2 e^{-\frac{\Delta}{\lambda}} \left(\frac{L}{\lambda} \right)^{a_3} \right) |\varphi|,
\end{aligned}
\tag{A.3}
$$

$$
\begin{aligned}
a_1 &:= 39.0876 \\
a_2 &:= 4527.5 \\
a_3 &:= 10.0887.
\end{aligned}
$$

This model was not chosen due to the same reasons as in the candidate model (A.1).

A.4 Model 4

$$\begin{aligned} |Z_{1,2}| &= |Z_{2,1}| \\ &\approx a_1 \; e^{-a_2 \frac{\Delta}{\lambda}} \left(\frac{L}{\lambda}\right)^{a_3} \; |\sin\varphi|, \end{aligned} \tag{A.4}$$

where

$$\begin{aligned} a_1 &:= 4824.8035, \\ a_2 &:= 0.8941, \\ a_3 &:= 9.6869. \end{aligned}$$

$|Z_{1,2}| = |Z_{2,1}|$ has values over several orders of magnitude. Hence, the latter would overweight those support regions of $\left\{\varphi, \frac{L}{\lambda}, \frac{\Delta}{\lambda}\right\}$ where $|Z_{1,2}| = |Z_{2,1}|$ is very large, thereby poorly fitting other regions of $\left\{\varphi, \frac{L}{\lambda}, \frac{\Delta}{\lambda}\right\}$ where $|Z_{1,2}| = |Z_{2,1}|$ is small. Specifically, the would-be-underweighted support region is where $\frac{L}{\lambda}$ increases toward unity and where $\frac{\Delta}{\lambda}$ decreases toward zero. Hence, this model was not chosen.

A.5 Model 5

$$\begin{aligned} |Z_{1,2}| &= |Z_{2,1}| \\ &\approx \left(a_1 + a_2 e^{-\frac{\Delta}{\lambda}} \left(\frac{L}{\lambda}\right)^{a_3}\right) \; |\sin\varphi|, \end{aligned} \tag{A.5}$$

where

$$\begin{aligned} a_1 &:= 42.1133 \\ a_2 &:= 4870.5 \\ a_3 &:= 10.0884. \end{aligned}$$

This model was not chosen due to the same reasons as in the candidate model (A.1).

A.6 Model 6

$$
\begin{aligned}
|Z_{1,2}| &= |Z_{2,1}| \\
&\approx \left(a_1 + a_2 e^{\left(-\frac{\Delta}{\lambda} + a_3 \frac{L}{\lambda}\right)}\right) |\sin\varphi|,
\end{aligned} \tag{A.6}
$$

where

$$
\begin{aligned}
a_1 &:= 34.4054 \\
a_2 &:= 0.0848 \\
a_3 &:= 10.9601.
\end{aligned}
$$

This model was not chosen due to the same reasons as in the candidate model (A.1).

A.7 Model 7

$$
\begin{aligned}
|Z_{1,2}| &= |Z_{2,1}| \\
&\approx a_1 \left(\frac{\Delta}{\lambda}\right)^{-a_2} \left(\frac{L}{\lambda}\right)^{a_3} |\sin\varphi|,
\end{aligned} \tag{A.7}
$$

where

$$
\begin{aligned}
a_1 &:= 2225.4020, \\
a_2 &:= 0.2129, \\
a_3 &:= 9.7105.
\end{aligned}
$$

This model was not chosen due to the same reasons as in the candidate model (A.1).

A.8 Model 8

$$\begin{aligned} |Z_{1,2}| &= |Z_{2,1}| \\ &\approx a_1 \, e^{\left(-a_2 \frac{\Delta}{\lambda} + a_3 \frac{L}{\lambda}\right)} \, |\sin\varphi|, \end{aligned} \tag{A.8}$$

where

$$\begin{aligned} a_1 &:= 0.1257, \\ a_2 &:= 0.8946, \\ a_3 &:= 10.5557. \end{aligned}$$

This model was not chosen due to the same reasons as in the candidate model (A.1).

A.9 Model 9

$$\begin{aligned} |Z_{1,2}| &= |Z_{2,1}| \\ &\approx a_1 \left(\frac{\Delta}{\lambda}\right)^{-1} \left(\frac{L}{\lambda}\right)^{a_2} |\sin\varphi|, \end{aligned} \tag{A.9}$$

where

$$\begin{aligned} a_1 &:= 78.1382, \\ a_2 &:= 9.4613. \end{aligned}$$

$|Z_{1,2}| = |Z_{2,1}|$ has values over several orders of magnitude. Hence, the latter would overweight those support regions of $\left\{\varphi, \frac{L}{\lambda}, \frac{\Delta}{\lambda}\right\}$ where $|Z_{1,2}| = |Z_{2,1}|$ is very large, thereby poorly fitting other regions of $\left\{\varphi, \frac{L}{\lambda}, \frac{\Delta}{\lambda}\right\}$ where $|Z_{1,2}| = |Z_{2,1}|$ is small. Specifically, the would-be-underweighted support region is where $\frac{L}{\lambda}$ increases toward unity and where $\frac{\Delta}{\lambda}$ decreases toward zero. Hence, this model was not chosen.

A.10 Model 10

$$
\begin{aligned}
\log|Z_{1,2}| &= \log|Z_{2,1}| \\
&\approx a_1 - \log\left|\frac{\Delta}{\lambda}\right| \\
&\quad + a_2 \ \log\left|\frac{L}{\lambda}\right| + \log|\sin(\varphi)|\,, \qquad \text{(A.10)}
\end{aligned}
$$

where

$$
\begin{aligned}
a_1 &:= 2.0469, \\
a_2 &:= 2.6230.
\end{aligned}
$$

This model was not chosen due to the low R^2 of 0.7723.

A.11 Model 11

$$
\begin{aligned}
\log|Z_{1,2}| &= \log|Z_{2,1}| \\
&\approx a_1 - a_2\log\left|\frac{\Delta}{\lambda}\right| \\
&\quad + a_3 \log\left|\frac{L}{\lambda}\right| + a_4\log|\sin(\varphi)|\,, \qquad \text{(A.11)}
\end{aligned}
$$

where

$$
\begin{aligned}
a_1 &:= 2.3066, \\
a_2 &:= 0.5564, \\
a_3 &:= 2.6230 \\
a_4 &:= 1.0059.
\end{aligned}
$$

This model was not selected because it has 4 degrees-of-freedom while the best fit model in (5.1) has has fewer degrees-of-freedom of 3.

A.12 Model 12

$$\begin{aligned}\log|Z_{1,2}| &= \log|Z_{2,1}| \\ &\approx a_1 + a_2 \log e^{\left(-\frac{\Delta}{\lambda}+a_3\frac{L}{\lambda}\right)} \\ &\quad + \log|\sin(\varphi)|\,, \end{aligned} \tag{A.12}$$

where

$$\begin{aligned} a_1 &:= 0.5060, \\ a_2 &:= 1.3268, \\ a_3 &:= 5.2816 \\ a_4 &:= 1.0059. \end{aligned}$$

This model was not selected because it has 4 degrees-of-freedom while the best fit model in (5.1) has only 3 degrees-of-freedom.

NOTE: For Models 13 to 16, the model fitting was done in two steps:

1. A proposed model, which is a function of the bivariate $\{\frac{\Delta}{\lambda}, \frac{L}{\lambda}\}$, is fitted through the MATLAB built-in function "cftool". Here, the φ is set to a fixed value during fitting.
2. The obtained optimized coefficients (i.e. c_1, c_2 and c_3) for all φ's are then averaged.

Noe that Models 13 to 16 were not chosen due to the incorrect method of generating the optimized coefficients.

A.13 Model 13

$$\begin{aligned} |Z_{1,2}| &= |Z_{2,1}| \\ &\approx \left(c_1 + c_2 e^{\left(-\frac{\Delta}{\lambda} + c_3 \frac{L}{\lambda}\right)}\right) |\varphi|, \end{aligned} \tag{A.13}$$

where

$$\begin{aligned} c_1 &:= [35.92\ 35.92\ 35.91\ 35.84\ 35.54\ 36\ 36\ 36] \\ &\approx 35.8192, \\ c_2 &:= [0.06779\ 0.06787\ 0.0682\ 0.06951\ 0.07433\ ... \\ & \quad 0.07995\ 0.08168\ 0.06941] \\ &\approx 0.0723, \\ c_3 &:= [11.18\ 11.17\ 11.17\ 11.14\ 11.06\ 10.96\ ... \\ & \quad 10.91\ 11.08] \\ &\approx 11.0838. \end{aligned}$$

The values of c_1, c_2, and c_3 are the averages of all c_1's, c_2's and c_3's for all φ's.

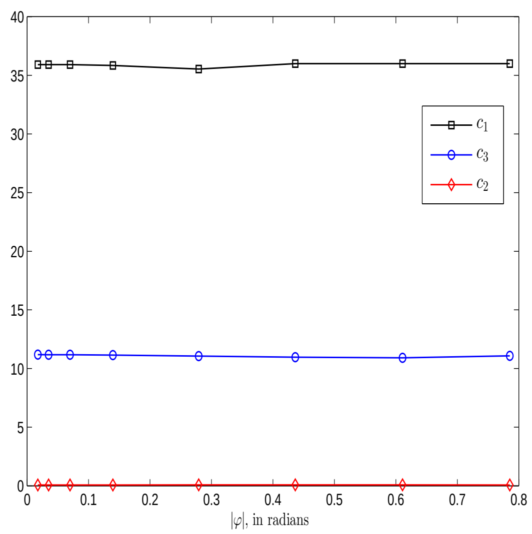

Figure A.1: How φ affects the coefficients of the 3-DoF model in (A.13).

A.14 Model 14

$$
\begin{aligned}
|Z_{1,2}| &= |Z_{2,1}| \\
&\approx \left(c_1 + c_2 e^{-\frac{\Delta}{\lambda}} \left(\frac{L}{\lambda}\right)^{c_3}\right) |\sin\varphi|,
\end{aligned} \tag{A.14}
$$

where

$$
\begin{aligned}
c_1 &:= [43.03\ 43.04\ 43.05\ 43.11\ 43.28\ 43.35\ 42.84\ 40.96] \\
&\approx \ 42.8325 \\
c_2 &:= [4827\ 4826\ 4823\ 4811\ 4772\ 4735\ 4771\ 5002] \\
&\approx \ 4820.9 \\
c_3 &:= [10.29\ 10.29\ 10.28\ 10.26\ 10.18\ 10.07\ 10.00\ 10.13] \\
&\approx \ 10.1875
\end{aligned}
$$

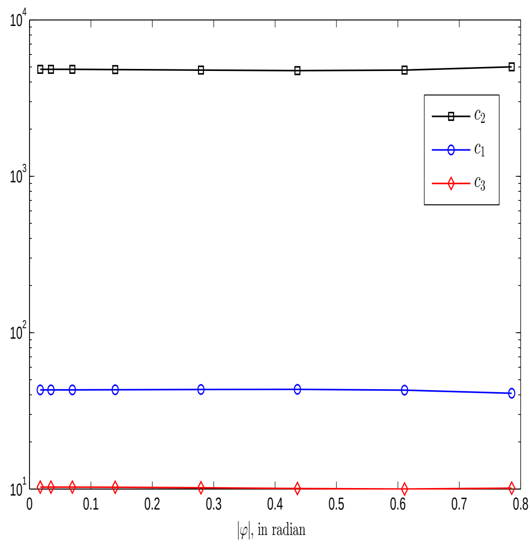

Figure A.2: How φ affects the coefficients of the 3-DoF model in (A.14).

A.15 Model 15

$$
\begin{aligned}
|Z_{1,2}| &= |Z_{2,1}| \\
&\approx \left(c_1 + c_2 e^{\left(-\frac{\Delta}{\lambda} + c_3 \frac{L}{\lambda}\right)}\right) |\sin\varphi|,
\end{aligned} \qquad \text{(A.15)}
$$

where

$$
\begin{aligned}
c_1 &:= [35.93\ 35.93\ 35.94\ 35.96\ 36\ 35.87\ 35.11\ 33.09] \\
&\approx\ 35.4788, \\
c_2 &:= [0.06779\ 0.06788\ 0.06826\ 0.06974\ 0.07531\ ... \\
&\quad\ 0.08394\ 0.09062\ 0.08395] \\
&\approx\ 0.0759, \\
c_3 &:= [11.18\ 11.17\ 11.17\ 11.14\ 11.06\ 10.94\ ... \\
&\quad\ 10.87\ 11] \\
&\approx\ 11.0663.
\end{aligned}
$$

The values of c_1, c_2, and c_3 are the averages of all c_1's, c_2's and c_3's for all φ's.

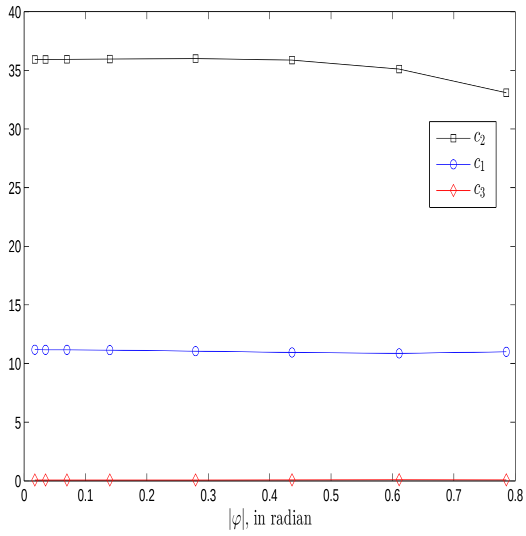

Figure A.3: How φ affects the coefficients of the 3-DoF model in (A.15).

A.16 Model 16

$$
\begin{aligned}
|Z_{1,2}| &= |Z_{2,1}| \\
&\approx \left(c_1 + c_2 e^{-\frac{\Delta}{\lambda}} \left(\frac{L}{\lambda}\right)^{c_3} \right) |\varphi|,
\end{aligned}
\tag{A.16}
$$

where

$$
\begin{aligned}
c_1 &:= [43.03\ 43.03\ 43.02\ 42.97\ 42.72\ 41.99\ 40.23\ 36.88] \\
&\approx \ 41.7338, \\
c_2 &:= [4827\ 4825\ 4819\ 4795\ 4710\ 4586\ 4480\ 4503] \\
&\approx \ 4693.1, \\
c_3 &:= [10.29\ 10.29\ 10.28\ 10.26\ 10.18\ 10.07\ 10\ 10.13] \\
&\approx \ 10.1875.
\end{aligned}
$$

The values of c_1, c_2, and c_3 are the averages of all c_1's, c_2's and c_3's for all φ's.

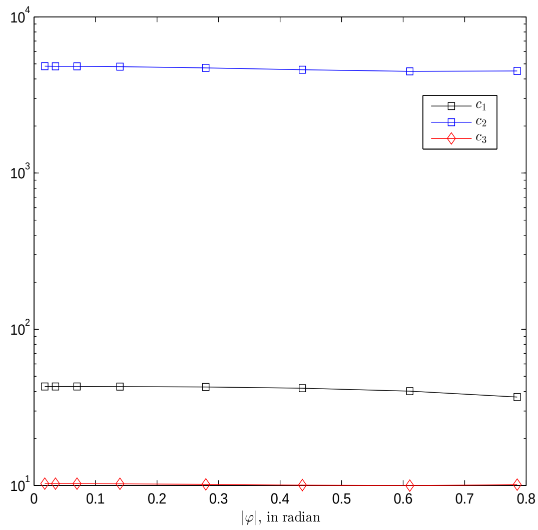

Figure A.4: How φ affects the coefficients of the 3-DoF model in (A.16).

A.17 Model 17

$$
\begin{aligned}
|Z_{1,2}| &= |Z_{2,1}| \\
&\approx c_0 + c_1 e^{(-c_2 \frac{\Delta}{\lambda})} \left(\frac{L}{\lambda}\right)^{c_3}
\end{aligned} \tag{A.17}
$$

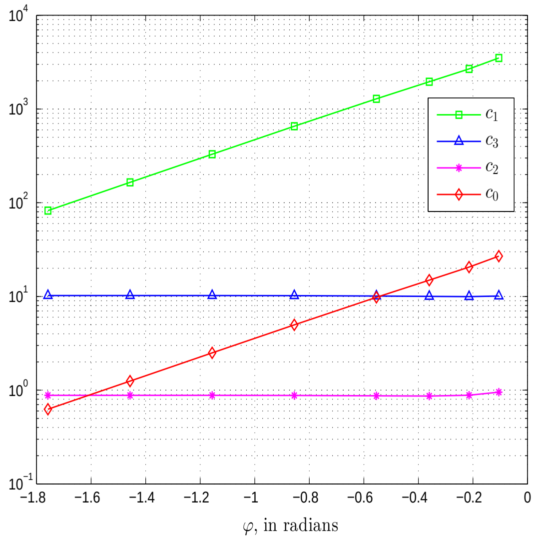

Figure A.5: How φ affects the coefficients of the 4-DoF model in (A.17).

From Figure A.5,

$$
\begin{aligned}
c_0 &\approx 0.7372 \;+\; 0.5954 \log|\varphi| \\
c_1 &\approx 2.855 \;+\; 0.5931 \log|\varphi| \\
c_2 &\approx 0.8866 \\
c_3 &\approx 10.1359
\end{aligned}
$$

A.18 Model 18

$$
\begin{aligned}
|Z_{1,2}| &= |Z_{2,1}| \\
&\approx c_0 + c_1 e^{\left(-\frac{\Delta}{\lambda} + c_2 \frac{L}{\lambda}\right)}
\end{aligned}
\tag{A.18}
$$

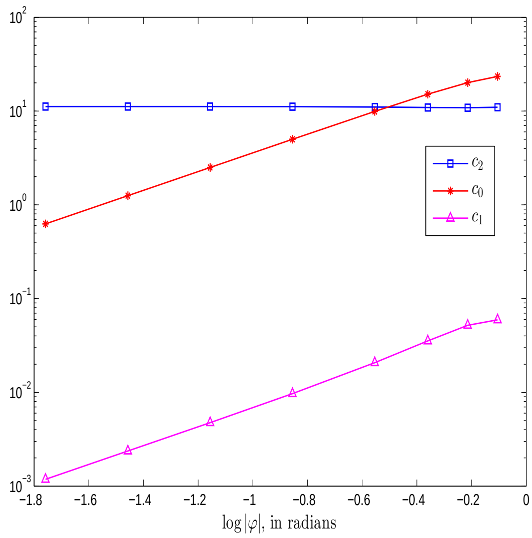

Figure A.6: How φ affects the coefficients of the 3-DoF model in (A.18).

From Figure A.6,

$$
\begin{aligned}
\log c_0 &\approx 1.511 \ + \ 0.9661 \log|\varphi| \\
c_0 &\approx 10^{(1.511 \ + \ 0.9661 \log|\varphi|)} \\
\log c_1 &\approx -1.091 \ + \ 1.053 \log|\varphi| \\
c_1 &\approx 10^{(-1.091 \ + \ 1.053 \log|\varphi|)} \\
c_2 &\approx 11.0663
\end{aligned}
$$

A.19 Model 19

$$\begin{aligned}\log|Z_{1,2}| &= \log|Z_{2,1}| \\ &\approx p_{0,0} + p_{0,1}\log\left(\frac{L}{\lambda}\right) + p_{0,2}\log^2\left(\frac{L}{\lambda}\right) + p_{1,0}\log\left(\frac{\Delta}{\lambda}\right) \\ &\quad + p_{1,2}\log\left(\frac{\Delta}{\lambda}\right)\log^2\left(\frac{L}{\lambda}\right).\end{aligned} \tag{A.19}$$

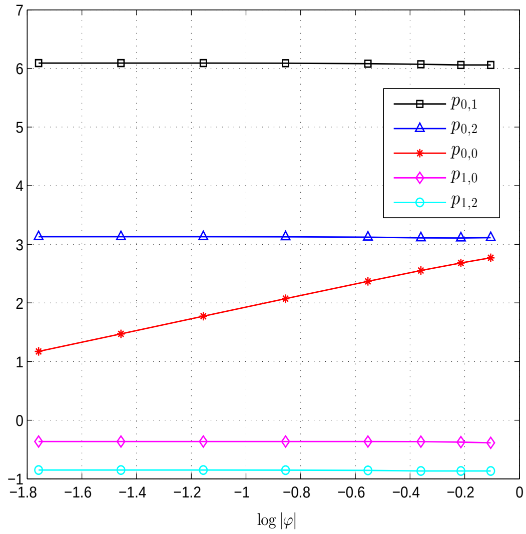

Figure A.7: How φ affects the coefficients of the 5-DoF model in (A.19).

From Figure A.7,

$$\begin{aligned} p_{0,0} &\approx 2.108 + 0.5881\log|\varphi| \\ p_{0,1} &\approx 6.0789 \\ p_{0,2} &\approx 3.1213 \\ p_{1,0} &\approx -0.3685 \\ p_{1,2} &\approx -0.8572 \end{aligned}$$

Models 17 to 19 were not selected due to the two-step process which is the incorrect way of getting the optimized coefficients.

Appendix B

Candidate Models for $\angle Z_{1,2} = \angle Z_{2,1}$

B.1 Model 1

$$\begin{aligned}
\angle Z_{1,2} &= \angle Z_{1,2} \\
&\approx b_1 \frac{\Delta}{\lambda} + b_2
\end{aligned} \tag{B.1}$$

here

$$\begin{aligned}
b_1 &:= -5.5920 \\
b_2 &:= 0.4910
\end{aligned}$$

This model failed to consider the effect of $\frac{L}{\lambda}$. The best fit phenomenological model in (5.3) is only independent of φ not with $\frac{L}{\lambda}$, hence, this model was not selected.

B.2 Model 2

For $\frac{\Delta}{\lambda} \leq 0.40$,

$$\begin{aligned}
\angle Z_{1,2} &= \angle Z_{1,2} \\
&\approx b_1 \frac{L}{\lambda} + b_2 \left(\frac{L}{\lambda}\right)^2 + b_3 \frac{\Delta}{\lambda} \left(\frac{L}{\lambda}\right)^2 + b_4 \left(\frac{L}{\lambda}\right)^3 + b_5 \frac{\Delta}{\lambda} \left(\frac{L}{\lambda}\right)^3 \\
&\quad + \ b_6 \left(\frac{L}{\lambda}\right)^4, \qquad \text{(B.2)}
\end{aligned}$$

where

$$\begin{aligned}
b_1 &:= -23.0477 \\
b_2 &:= 124.3852 \\
b_3 &:= -39.8265 \\
b_4 &:= -199.5342 \\
b_5 &:= 38.2241 \\
b_6 &:= 100.1033
\end{aligned}$$

For $\frac{\Delta}{\lambda} > 0.40$,

$$\begin{aligned}
\angle Z_{1,2} &= \angle Z_{1,2} \\
&\approx \begin{cases} b_7 \left(x + 0.6\right) + b_8 & \text{if } x \in [0, 0.2], \\ \\ b_9 \left(x + 0.6\right) + b_{10} & \text{if } x \in [0.2, 1.0], \end{cases}
\end{aligned} \qquad \text{(B.3)}$$

where

$$x \triangleq \left(\frac{\Delta}{\lambda} + b_{11} e^{\left(b_{12} \frac{L}{\lambda}\right)} - 0.6\right) \bmod 1$$

where

$$
\begin{aligned}
b_7 &:= 19.1744 \\
b_8 &:= -14.0835 \\
b_9 &:= -6.2797 \\
b_{10} &:= 7.6338 \\
b_{11} &:= 8.3065 \times 10^{-6} \\
b_{12} &:= 11.2036.
\end{aligned}
$$

The model was not selected for the reason that it is complicated and fewer degrees-of-freedom is preferred. The chosen phenomenological model for $\angle Z_{1,2}$ has only 3 degrees-of-freedom.

B.3 Model 3

$$
\begin{aligned}
\angle Z_{1,2} &= \angle Z_{1,2} \\
&\approx \left\{ b_1 + b_2 \frac{L}{\lambda} + b_3 \left(\frac{L}{\lambda}\right)^2 + b_4 \left(\frac{L}{\lambda}\right)^3 + b_5 \left(\frac{L}{\lambda}\right)^4 \right\} \\
&\quad \left\{ b_6 \sin\left(b_7 \frac{\Delta}{\lambda} + b_8 \right) + b_9 \sin\left(b_{10} \frac{\Delta}{\lambda} + b_{11} \right) \right\}
\end{aligned} \tag{B.4}
$$

where

$$
\begin{aligned}
b_1 &:= 2.2413 \\
b_2 &:= 1.9464 \\
b_3 &:= -0.0254 \\
b_4 &:= -4.2087 \\
b_5 &:= 2.2045 \\
b_6 &:= 9.5608 \\
b_7 &:= 0.4453 \\
b_8 &:= 2.3251 \\
b_9 &:= 8.9874 \\
b_{10} &:= 0.2373 \\
b_{11} &:= 2.2733
\end{aligned}
$$

The model was not selected for the reason that it is complicated and fewer degrees-of-freedom is preferred. The chosen phenomenological model for $\angle Z_{1,2}$ has only 3 degrees-of-freedom.

B.4 Model 4

This model involves two parts: (1) $\frac{\Delta}{\lambda} \leq 0.40$, and (2) $\frac{\Delta}{\lambda} > 0.40$.

For $\frac{\Delta}{\lambda} \leq 0.40$,

$$\begin{aligned} \angle Z_{1,2} &= \angle Z_{1,2} \\ &\approx c_1 \frac{L}{\lambda} + c_2 \left(\frac{L}{\lambda}\right)^2 + c_3 \frac{\Delta}{\lambda} \left(\frac{L}{\lambda}\right)^2 \\ &+ c_4 \left(\frac{L}{\lambda}\right)^3 + c_5 \frac{\Delta}{\lambda} \left(\frac{L}{\lambda}\right)^3 \\ &+ c_6 \left(\frac{L}{\lambda}\right)^4 . \end{aligned} \tag{B.5}$$

For each φ,

$$\begin{aligned} c_1 &:= [-22.13\ -22.13\ -22.13\ -22.14\ -22.18\ -22.25\ -22.35\ -22.49] \\ &\approx -22.2250 \\ c_2 &:= [120.1\ 120.1\ 120.1\ 120.1\ 119.9\ 119.7\ 119.4\ 118.8] \\ &\approx 119.7750 \\ c_3 &:= [-39.83\ -39.83\ -39.84\ -39.88\ -40.01\ -40.23\ -40.46\ -40.56] \\ &\approx -40.0800 \\ c_4 &:= [-193.4\ -193.4\ -193.3\ -193.2\ -192.6\ -191.5\ -189.7\ -187.4] \\ &\approx -191.8125 \\ c_5 &:= [38.16\ 38.17\ 38.18\ 38.23\ 38.42\ 38.73\ 39.04\ 39.17] \\ &\approx 38.5125 \\ c_6 &:= [97.3\ 97.29\ 97.26\ 97.15\ 96.69\ 95.85\ 94.54\ 92.89] \\ &\approx 96.1212 \end{aligned}$$

The values of $c_1 - c_6$ are the averages of all c_1's to c_6's for all φ's.

For $\frac{\Delta}{\lambda} > 0.40$,

$$\angle Z_{1,2} = \angle Z_{1,2} \approx \begin{cases} c_7\,(x+0.6)+c_8 & \text{if } x \in [0, 0.2], \\ c_9\,(x+0.6)+c_{10} & \text{if } x \in [0.2, 1.0], \end{cases}$$

$$x \triangleq \left(\frac{\Delta}{\lambda} + c_{11} e^{\left(c_{12}\frac{L}{\lambda}\right)} - 0.6\right) \bmod 1$$

For each φ,

$$\begin{aligned}
c_7 &:= [27.8162\ 27.6606\ 27.6593\ 27.6346\ 27.5995\ 27.5493\ 27.4948\ 27.6543] \\
&\approx 27.6336 \\
c_8 &:= [-19.6240\ \ -19.5271\ \ -19.5262\ \ -19.5229\ \ -19.5097\ \ -19.4862\ \ -19.4525\ \ -19.4155] \\
&\approx -19.5080 \\
c_9 &:= [-6.2046\ \ -6.2046\ \ -6.2046\ \ -6.2045\ \ -6.2044\ \ -6.2041\ \ -6.2038\ \ -6.2035] \\
&\approx -6.2043 \\
c_{10} &:= [7.5924\ 7.5925\ 7.5925\ 7.5925\ 7.5928\ 7.5933\ 7.5940\ 7.5949] \\
&\approx 7.5931 \\
c_{11} &:= [0.00006\ 0.00006\ 0.00006\ 0.00006\ 0.00006\ 0.00006\ 0.00006\ 0.00006] \\
&\approx 6 \times 10^{-5} \\
c_{12} &:= [9.20\ 9.20\ 9.20\ 9.20\ 9.20\ 9.20\ 9.20\ 9.20] \\
&\approx 9.2000
\end{aligned}$$

The values of $c_7 - c_{12}$ are the averages of all c_7's to c_{12}'s for all φ's.

Model 4 applied the two-step process, which is an incorrect way of optimizing the unknown coefficients. Hence, it was selected.

Appendix C

Candidate Models for $|Z_{1,1}| = |Z_{2,2}|$

C.1 Model 1

$$\begin{aligned} |Z_{1,1}| &= |Z_{2,2}| \\ &\approx \left\{ p_1 + p_2 \cos\left(p_3 \frac{\Delta}{\lambda} + p_4 \right) \; e^{-p_5 \frac{\Delta}{\lambda}} \; e^{p_6 \varphi} \right\} \\ &\quad \left\{ \left(\frac{L}{\lambda} - p_7 \right)^2 + p_8 \right\}, \end{aligned} \tag{C.1}$$

where

$$\begin{aligned} p_1 &:= 23422.3889, \\ p_2 &:= 53.9352, \\ p_3 &:= 3.9029\pi, \\ p_4 &:= 5.5776\pi, \\ p_5 &:= 0.5118, \\ p_6 &:= 3.8075, \\ p_7 &:= 0.4811, \\ p_8 &:= -0.0018. \end{aligned}$$

This model is not recommended since $|Z_{1,1}| = |Z_{2,2}|$ takes on values over a large range. $|Z_{1,1}| = |Z_{2,2}|$ takes on values over several orders of magnitude. Hence, any R^2 computation based on (C.1) would overweight those support subregions of $\left\{\varphi, \frac{L}{\lambda}, \frac{\Delta}{\lambda}\right\}$ where $|Z_{1,1}| = |Z_{2,2}|$ is very large, thereby poorly fitting other regions of $\left\{\varphi, \frac{L}{\lambda}, \frac{\Delta}{\lambda}\right\}$ where $|Z_{1,1}| = |Z_{2,2}|$ is small. More explicitly, the would-be-overweighted region is where $\frac{L}{\lambda}$ increases toward unity and where $\frac{\Delta}{\lambda}$ decreases toward zero. Another reason why this model was not chosen because at $\frac{L}{\lambda} = p_7$, $|Z_{1,1}| < 0$, which is illogical.

C.2 Model 2

$$\begin{aligned} |Z_{1,1}| &= |Z_{2,2}| \\ &\approx \left\{ p_1 + p_2 \cos \left(p_3 \frac{\Delta}{\lambda} + p_4 \right) \ e^{-p_5 \frac{\Delta}{\lambda}} \ |\varphi| \right\} \\ &\quad \left\{ \left(\frac{L}{\lambda} - p_6 \right)^2 + p_7 \right\}, \end{aligned} \tag{C.2}$$

where

$$\begin{aligned} p_1 &:= 23521.2122, \\ p_2 &:= 63.5567, \\ p_3 &:= -6.6653\pi, \\ p_4 &:= 5.0417\pi, \\ p_5 &:= 73.1540, \\ p_6 &:= 0.4811, \\ p_7 &:= -0.0018. \end{aligned}$$

The reasons for not choosing this model are the same as in (C.1).

C.3 Model 3

$$
\begin{aligned}
|Z_{1,1}| &= |Z_{2,2}| \\
&\approx \left\{ p_1 + p_2 \cos\left(p_3 \frac{\Delta}{\lambda} + p_4 \right) \; e^{-p_5 \frac{\Delta}{\lambda}} \; |\varphi|^{p_6} \right\} \\
&\quad \left\{ \left(\frac{L}{\lambda} - p_7 \right)^2 + p_8 \right\}, \qquad \text{(C.3)}
\end{aligned}
$$

where

$$
\begin{aligned}
p_1 &:= 23520.6470, \\
p_2 &:= 45.6549, \\
p_3 &:= 36.2684\pi, \\
p_4 &:= 6.5309\pi, \\
p_5 &:= 17.7974, \\
p_6 &:= 3.1830, \\
p_7 &:= 0.4811, \\
p_8 &:= -0.0018.
\end{aligned}
$$

The reasons for not choosing this model are the same as in (C.1).

C.4 Model 4

$$
\begin{aligned}
|Z_{1,1}| &= |Z_{2,2}| \\
&\approx \left\{ p_1 + p_2 \cos\left(p_3 \frac{\Delta}{\lambda} + p_4 \right) \; e^{-p_5 \frac{\Delta}{\lambda}} \; |\sin(\varphi)| \right\} \\
&\quad \left\{ \left(\frac{L}{\lambda} - p_6 \right)^2 + p_7 \right\},
\end{aligned}
\tag{C.4}
$$

where

$$
\begin{aligned}
p_1 &:= 23506.3520, \\
p_2 &:= 92.8410, \\
p_3 &:= 1.3200\pi, \\
p_4 &:= 6.0051\pi, \\
p_5 &:= 1.3121, \\
p_6 &:= 0.4811, \\
p_7 &:= -0.0018.
\end{aligned}
$$

The reasons for not choosing this model are the same as in (C.1).

C.5 Model 5

$$
\begin{aligned}
|Z_{1,1}| &= |Z_{2,2}| \\
&\approx \left\{ p_1 + p_2 \overbrace{\cos\left(p_3 \frac{\Delta}{\lambda} + p_4\right) \; e^{-p_5 \frac{\Delta}{\lambda}}}^{P_1\left(\frac{\Delta}{\lambda}\right) :=} \; \sin^2(\varphi) \right\} \\
&\quad \left\{ \left(\frac{L}{\lambda} - p_6\right)^2 + p_7 \right\}, \qquad \text{(C.5)}
\end{aligned}
$$

where

$$
\begin{aligned}
p_1 &:= 23439.3128, \\
p_2 &:= 1914.2833, \\
p_3 &:= -3.8994\pi, \\
p_4 &:= 0.4090\pi, \\
p_5 &:= 0.5087, \\
p_6 &:= 0.4812, \\
p_7 &:= -0.0018.
\end{aligned}
$$

The reasons for not choosing this model are the same as in (C.1).

C.6 Model 6

$$\begin{aligned}
|Z_{1,1}| &= |Z_{2,2}| \\
&\approx \left\{ p_1 + p_2 \cos\left(p_3 \frac{\Delta}{\lambda} + p_4 \right) \; e^{-p_5 \frac{\Delta}{\lambda}} \; |\sin(\varphi)|^{p_6} \right\} \\
&\quad \left\{ \left(\frac{L}{\lambda} - p_7 \right)^2 + p_8 \right\},
\end{aligned} \tag{C.6}$$

where

$$\begin{aligned}
p_1 &:= 23520.4845, \\
p_2 &:= 112.9325, \\
p_3 &:= 2.7775\pi, \\
p_4 &:= 4.9792\pi, \\
p_5 &:= 178.9852, \\
p_6 &:= 5.5039, \\
p_7 &:= 0.4811, \\
p_8 &:= -0.0018.
\end{aligned}$$

The reasons for not choosing this model are the same as in (C.1).

C.7 Model 7

$$
\begin{aligned}
|Z_{1,1}| &= |Z_{2,2}| \\
&\approx \left\{ p_1 + p_2 \cos\left(p_3 \frac{\Delta}{\lambda} + p_4 \right) \ e^{-p_5 \frac{\Delta}{\lambda}} \ \sin^2(\varphi) \right\} \\
&\quad \left\{ \left(\frac{L}{\lambda} - p_6 \right)^2 + p_7 \right\}, \qquad \text{(C.7)}
\end{aligned}
$$

where

$$
\begin{aligned}
p_1 &:= 23138.1624, \\
p_2 &:= 1924.3751, \\
p_3 &:= 3.9229\pi, \\
p_4 &:= 5.5608\pi, \\
p_5 &:= 0.4888, \\
p_6 &:= 0.4804, \\
p_7 &:= 0.00000025733.
\end{aligned}
$$

This model was not selected since $|Z_{1,1}| = |Z_{2,2}|$ takes on values over a large range. $|Z_{1,1}| = |Z_{2,2}|$ takes on values over several orders of magnitude. Hence, any R^2 computation based on (C.1) would overweight those support subregions of $\left\{\varphi, \frac{L}{\lambda}, \frac{\Delta}{\lambda}\right\}$ where $|Z_{1,1}| = |Z_{2,2}|$ is very large, thereby poorly fitting other regions of $\left\{\varphi, \frac{L}{\lambda}, \frac{\Delta}{\lambda}\right\}$ where $|Z_{1,1}| = |Z_{2,2}|$ is small. More explicitly, the would-be-overweighted region is where $\frac{L}{\lambda}$ increases toward unity and where $\frac{\Delta}{\lambda}$ decreases toward zero.

C.8 Model 8

$$
\begin{aligned}
|Z_{1,1}| &= |Z_{2,2}| \\
&\approx \left\{ p_1 + p_2 \cos\left(p_3 \frac{\Delta}{\lambda} + p_4\right)\ e^{-p_5 \frac{\Delta}{\lambda}}\ e^{p_6 \varphi} \right\} \\
&\quad \left\{ p_7 e^{p_8 \frac{L}{\lambda}} + p_9 e^{p_{10} \frac{L}{\lambda}} \right\}, \qquad \text{(C.8)}
\end{aligned}
$$

where

$$
\begin{aligned}
p_1 &:= 4.3710, \\
p_2 &:= -0.0007, \\
p_3 &:= 0.5601, \\
p_4 &:= 3.4014, \\
p_5 &:= 1.6758, \\
p_6 &:= 3.6285, \\
p_7 &:= 0.1622, \\
p_8 &:= 1.6959, \\
p_9 &:= 0.9041, \\
p_{10} &:= -3.2461.
\end{aligned}
$$

This model was not selected due to the large number of degrees-of-freedom.

C.9 Model 9

$$
\begin{aligned}
|Z_{1,1}| &= |Z_{2,2}| \\
&\approx \left\{ p_1 + p_2 \cos\left(p_3 \frac{\Delta}{\lambda} + p_4 \right) \; e^{-p_5 \frac{\Delta}{\lambda}} \; e^{p_6 \varphi} \right\} \\
&\quad \left\{ p_7 e^{-\left(\frac{\frac{L}{\lambda} - p_8}{p_9} \right)^2} + p_{10} e^{-\left(\frac{\frac{L}{\lambda} - p_{11}}{p_{12}} \right)^2} \right\},
\end{aligned} \tag{C.9}
$$

where

$$
\begin{aligned}
p_1 &:= 3.9153, \\
p_2 &:= -0.3183, \\
p_3 &:= 2.1916, \\
p_4 &:= 1.3968, \\
p_5 &:= 4.0320, \\
p_6 &:= -5.0740, \\
p_7 &:= -0.4343, \\
p_8 &:= 0.4983, \\
p_9 &:= 0.2868, \\
p_{10} &:= 1.0087, \\
p_{11} &:= 0.6649, \\
p_{12} &:= 2.5468.
\end{aligned}
$$

This model was not selected due to its complexity and due to the large number of degrees-of-freedom.

C.10 Model 10

$$
\begin{aligned}
|Z_{1,1}| &= |Z_{2,2}| \\
&\approx \left\{ p_1 + p_2 \cos\left(p_3 \frac{\Delta}{\lambda} + p_4 \right) \; e^{-p_5 \frac{\Delta}{\lambda}} \; e^{p_6 \varphi} \right\} \\
& \quad \left\{ p_7 \left(\frac{L}{\lambda} \right)^4 + p_8 \left(\frac{L}{\lambda} \right)^3 + p_9 \left(\frac{L}{\lambda} \right)^2 + p_{10} \left(\frac{L}{\lambda} \right) + p_{11} \right\},
\end{aligned} \tag{C.10}
$$

where

$$
\begin{aligned}
p_1 &:= -0.2816, \\
p_2 &:= 177.4234, \\
p_3 &:= 0.4715, \\
p_4 &:= 1.5658, \\
p_5 &:= 146.3067, \\
p_6 &:= -127.0248, \\
p_7 &:= 59.9839, \\
p_8 &:= -107.6804, \\
p_9 &:= 32.4132, \\
p_{10} &:= 16.6568, \\
p_{11} &:= -15.0194,
\end{aligned}
$$

This model was not selected due to its complexity and due to the large number of degrees-of-freedom.

C.11 Model 11

$$\begin{aligned} |Z_{1,1}| &= |Z_{2,2}| \\ &\approx \left\{p_1 + p_2 \cos\left(p_3 \frac{\Delta}{\lambda} + p_4\right)\ e^{-p_5 \frac{\Delta}{\lambda}}\ |\varphi|^{p_6}\right\} \\ &\quad \left\{p_7 e^{p_8 \frac{L}{\lambda}} + p_9 e^{p_{10} \frac{L}{\lambda}}\right\}, \end{aligned} \tag{C.11}$$

where

$$\begin{aligned} p_1 &:= 0.3916, \\ p_2 &:= -0.0671, \\ p_3 &:= 13.8602, \\ p_4 &:= 7.4596, \\ p_5 &:= 9.1662, \\ p_6 &:= 13.8754, \\ p_7 &:= 1.8111, \\ p_8 &:= 1.6958, \\ p_9 &:= 10.0953, \\ p_{10} &:= -3.2461. \end{aligned}$$

This model was not selected due to the large number of degrees-of-freedom.

C.12 Model 12

$$
\begin{aligned}
|Z_{1,1}| &= |Z_{2,2}| \\
&\approx \left\{ p_1 + p_2 \cos\left(p_3 \frac{\Delta}{\lambda} + p_4 \right) \; e^{-p_5 \frac{\Delta}{\lambda}} \; |\sin(\varphi)|^{p_6} \right\} \\
&\quad \left\{ p_7 e^{p_8 \frac{L}{\lambda}} + p_9 e^{p_{10} \frac{L}{\lambda}} \right\}, \qquad \text{(C.12)}
\end{aligned}
$$

where

$$
\begin{aligned}
p_1 &:= 0.6306, \\
p_2 &:= 0.3413, \\
p_3 &:= 8.4951, \\
p_4 &:= 11.7166, \\
p_5 &:= 7.8617, \\
p_6 &:= 13.9790, \\
p_7 &:= 1.1244, \\
p_8 &:= 1.6958, \\
p_9 &:= 6.2680, \\
p_{10} &:= -3.2461.
\end{aligned}
$$

This model was not selected due to the large number of degrees-of-freedom.

C.13 Model 13

$$
\begin{aligned}
|Z_{1,1}| &= |Z_{2,2}| \\
&\approx \left\{ p_1 + p_2 \cos\left(p_3 \frac{\Delta}{\lambda} + p_4 \right) \; e^{-p_5 \frac{\Delta}{\lambda}} \; |\varphi|^{p_6} \right\} \\
&\quad \left\{ p_7 e^{-\left(\frac{\frac{L}{\lambda} - p_8}{p_9} \right)^2} + p_{10} e^{-\left(\frac{\frac{L}{\lambda} - p_{11}}{p_{12}} \right)^2} \right\},
\end{aligned}
\tag{C.13}
$$

where

$$
\begin{aligned}
p_1 &:= 4.2666, \\
p_2 &:= 10.1235, \\
p_3 &:= 1.3079, \\
p_4 &:= -0.1623, \\
p_5 &:= 12.9825, \\
p_6 &:= 25.3620, \\
p_7 &:= -0.3792, \\
p_8 &:= 0.4863, \\
p_9 &:= 0.2910, \\
p_{10} &:= 0.9046, \\
p_{11} &:= -0.0311, \\
p_{12} &:= 26.6629.
\end{aligned}
$$

This model was not selected due to its complexity and due to the large number of degrees-of-freedom.

C.14 Model 14

$$
\begin{aligned}
|Z_{1,1}| &= |Z_{2,2}| \\
&\approx \left\{ p_1 + p_2 \cos\left(p_3 \frac{\Delta}{\lambda} + p_4 \right) \; e^{-p_5 \frac{\Delta}{\lambda}} \; |\sin(\varphi)|^{p_6} \right\} \\
&\quad \left\{ p_7 e^{-\left(\frac{\frac{L}{\lambda} - p_8}{p_9} \right)^2} + p_{10} e^{-\left(\frac{\frac{L}{\lambda} - p_{11}}{p_{12}} \right)^2} \right\},
\end{aligned} \tag{C.14}
$$

where

$$
\begin{aligned}
p_1 &:= 10.5046, \\
p_2 &:= 3.5518, \\
p_3 &:= -0.7215, \\
p_4 &:= 2.6124, \\
p_5 &:= 19.6664, \\
p_6 &:= 16.8376, \\
p_7 &:= -0.1532, \\
p_8 &:= 0.4872, \\
p_9 &:= 0.2893, \\
p_{10} &:= 0.3669, \\
p_{11} &:= 1.2465, \\
p_{12} &:= 22.4539.
\end{aligned}
$$

This model was not selected due to its complexity and due to the large number of degrees-of-freedom.

C.15 Model 15

$$
\begin{aligned}
|Z_{1,1}| &= |Z_{2,2}| \\
&\approx \left\{ p_1 + p_2 \cos\left(p_3 \frac{\Delta}{\lambda} + p_4 \right) \; e^{-p_5 \frac{\Delta}{\lambda}} \; |\varphi|^{p_6} \right\} \\
&\quad \left\{ p_7 \left(\frac{L}{\lambda} \right)^4 + p_8 \left(\frac{L}{\lambda} \right)^3 + p_9 \left(\frac{L}{\lambda} \right)^2 + p_{10} \left(\frac{L}{\lambda} \right) + p_{11} \right\}, \qquad \text{(C.15)}
\end{aligned}
$$

where

$$
\begin{aligned}
p_1 &:= 4.6067, \\
p_2 &:= -8.4630, \\
p_3 &:= -0.0007, \\
p_4 &:= 1.5720, \\
p_5 &:= -0.7125, \\
p_6 &:= 4.3720, \\
p_7 &:= -5.0905, \\
p_8 &:= 9.9604, \\
p_9 &:= -4.6921, \\
p_{10} &:= -0.1901, \\
p_{11} &:= 0.8449,
\end{aligned}
$$

This model was not selected due to its complexity and due to the large number of degrees-of-freedom.

C.16 Model 16

$$\begin{aligned}
|Z_{1,1}| &= |Z_{2,2}| \\
&\approx \left\{ p_1 + p_2 \cos\left(p_3 \frac{\Delta}{\lambda} + p_4 \right) \; e^{-p_5 \frac{\Delta}{\lambda}} \; |\sin\varphi|^{p_6} \right\} \\
& \quad \left\{ p_7 \left(\frac{L}{\lambda} \right)^4 + p_8 \left(\frac{L}{\lambda} \right)^3 + p_9 \left(\frac{L}{\lambda} \right)^2 + p_{10} \left(\frac{L}{\lambda} \right) + p_{11} \right\}, \qquad \text{(C.16)}
\end{aligned}$$

where

$$\begin{aligned}
p_1 &:= 2.8236, \\
p_2 &:= 0.5890, \\
p_3 &:= -4.1481, \\
p_4 &:= 1.5905, \\
p_5 &:= 5.2617, \\
p_6 &:= 4.5600, \\
p_7 &:= -12.0029, \\
p_8 &:= 24.4661, \\
p_9 &:= -13.7944, \\
p_{10} &:= 1.4457, \\
p_{11} &:= 1.2264,
\end{aligned}$$

This model was not selected due to its complexity and due to the large number of degrees-of-freedom.

NOTE: The model fitting from Models 17-20 is done in two steps:

1. The VLab data for $|Z_{1,1}| = |Z_{2,2}|$ will be fitted to equation (C.17) per $\frac{L}{\lambda}$ value in the MATLAB built-in function, “cftool”.

2. The obtained optimized coefficients per $\frac{L}{\lambda}$ in (1) will then again be fitted to another function, which is again done in “cftool”.

C.17 Model 17

The proposed model is,

$$
\begin{aligned}
|Z_{1,1}| &= |Z_{2,2}| \\
&\approx \left\{ c_1 + c_2 \cos\left(c_3 \frac{\Delta}{\lambda} + c_4 \right) e^{-c_5 \frac{\Delta}{\lambda}} |\varphi|^{c_6} \right\} \\
&\quad \left\{ \left(\frac{L}{\lambda} - c_7 \right)^2 + c_8 \right\}
\end{aligned}
\tag{C.17}
$$

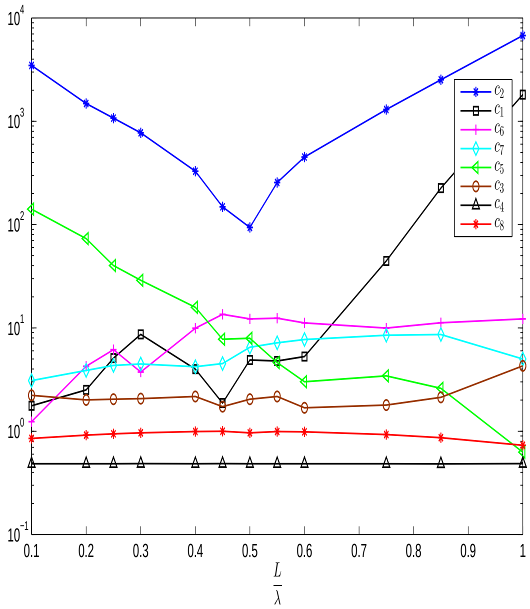

Figure C.1: How $\frac{L}{\lambda}$ affects the coefficients of the 8-DoF model in (C.17).

From Fig. C.1,

$$
\begin{aligned}
c_1 &\approx 2474 + 2991\cos\left(5.677\,\frac{L}{\lambda}\right) - 995.7\sin\left(5.677\,\frac{L}{\lambda}\right) \\
&\quad + 1099\cos\left(11.354\,\frac{L}{\lambda}\right) - 671.1\sin\left(11.354\,\frac{L}{\lambda}\right) \\
&\quad + 503.3\cos\left(17.031\,\frac{L}{\lambda}\right) - 429.8\sin\left(17.031\,\frac{L}{\lambda}\right) \\
&\quad + 212.7\cos\left(22.708\,\frac{L}{\lambda}\right) - 199.1\sin\left(22.708\,\frac{L}{\lambda}\right) \\
&\quad + 25.54\cos\left(28.385\,\frac{L}{\lambda}\right) - 120\sin\left(28.385\,\frac{L}{\lambda}\right) \\
c_2 &\approx 0.001378\,e^{14.09\frac{L}{\lambda}} + 2.194 \\
c_3 &\approx \frac{9.177\left(\frac{L}{\lambda}\right)^3 - 6.949\left(\frac{L}{\lambda}\right)^2 + 0.7756\frac{L}{\lambda} + 0.2854}{\left(\frac{L}{\lambda}\right)^2 - 0.8883\frac{L}{\lambda} + 0.2063} \\
c_4 &\approx 19.89\sin\left(3.71\,\frac{L}{\lambda} - 0.1706\right) \\
&\quad + 14.53\sin\left(4.653\,\frac{L}{\lambda} + 2.715\right) \\
&\quad + 0.5484\sin\left(18.28\,\frac{L}{\lambda} - 2.858\right) \\
&\quad + 0.3028\sin\left(32.39\,\frac{L}{\lambda} - 2.655\right) \\
c_5 &\approx 304\,e^{-7.607\frac{L}{\lambda}} \\
c_6 &\approx 2.1968 \\
c_7 &\approx 0.4850 \\
c_8 &\approx -0.9698\left(\frac{L}{\lambda} - 0.4814\right)^2 + 0.994
\end{aligned}
$$

This model fits the data using the Fourier series at the $\frac{L}{\lambda}$ values where VLab simulations are done, hence the many cosine functions. However, the coefficient values depend on the Fourier series grid, so this model is not chosen.

C.18 Model 18

$$
\begin{aligned}
|Z_{1,1}| &= |Z_{2,2}| \\
&\approx \left\{ c_1 + c_2 \cos\left(c_3 \frac{\Delta}{\lambda} + c_4 \right) e^{\left(-c_5 \frac{\Delta}{\lambda} + c_6 \varphi\right)} \right\} \left\{ \left(\frac{L}{\lambda} - c_7 \right)^2 + c_8 \right\} \quad \text{(C.18)}
\end{aligned}
$$

From Fig. C.2,

$$
\begin{aligned}
c_1 &\approx 137200\ e^{-\left(\frac{\frac{L}{\lambda}-0.4483}{0.04192}\right)^2} + 33430 \\
c_2 &\approx 99.5\ e^{-\left(\frac{\frac{L}{\lambda}-0.4771}{0.05298}\right)^2} + 17.87 \\
c_3 &\approx 1477000\ e^{-101.2\frac{L}{\lambda}} + 9.58 \\
c_4 &\approx -23.49\ e^{-2.606\frac{L}{\lambda}} + 18.6 \\
c_5 &\approx 417.4\ e^{-8.613\frac{L}{\lambda}} \\
c_6 &\approx 3.9800 \\
c_7 &\approx 0.4786 \\
c_8 &\approx -0.0045
\end{aligned}
$$

The functions c_1, c_2, c_3, c_4 and c_5 are derived from the 2D curve fitting in Matlab's "cftool". While the values of c_6, c_7 and c_8 are averages for all $\frac{L}{\lambda}$'s.

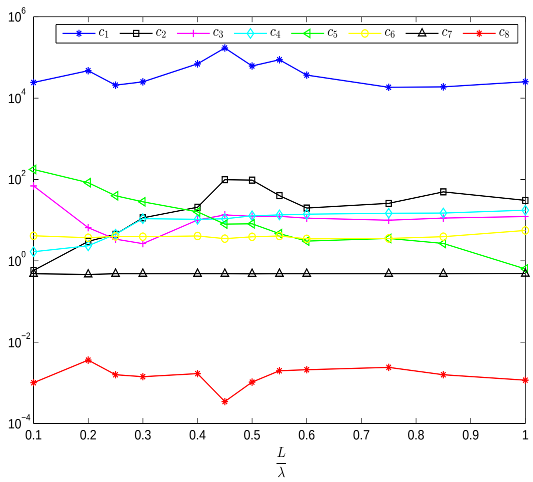

Figure C.2: How $\frac{L}{\lambda}$ affects the coefficients of the 8-DoF model in (C.18).

C.19 Model 19

$$\begin{aligned} |Z_{1,1}| &= |Z_{2,2}| \\ &\approx \left\{ c_1 + c_2 \cos\left(c_3 \frac{\Delta}{\lambda} + c_4\right) e^{\left(-c_5 \frac{\Delta}{\lambda}\right)} \left(\left(\frac{L}{\lambda} - c_7\right)^2 + c_8\right) \right\} e^{(c_6 \varphi)} \end{aligned} \tag{C.19}$$

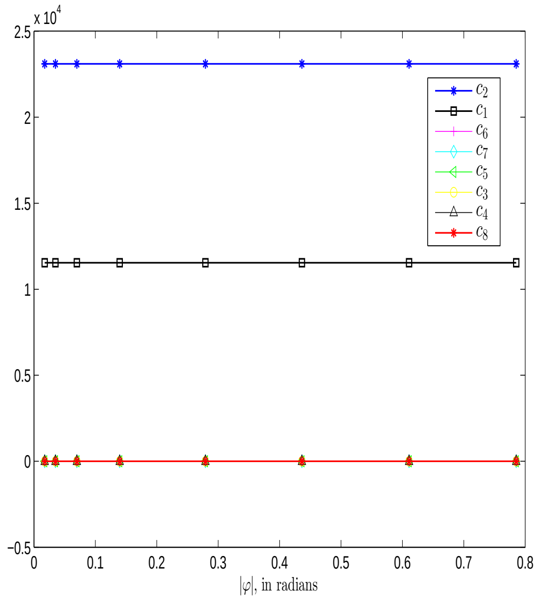

Figure C.3: How φ affects the coefficients of the 8-DoF model in (C.19).

From Fig. C.3,

$$\begin{aligned} c_1 &\approx 11540 \\ c_2 &\approx 23100 \\ c_3 &\approx 2.7608 \times 10^{-5} \\ c_4 &\approx 1.787 \times 10^{-4} \\ c_5 &\approx 1.2792 \times 10^{-4} \\ c_6 &\approx 0.2507 \\ c_7 &\approx 0.4811 \\ c_8 &\approx -0.5014 \end{aligned}$$

C.20 Model 20

$$
\begin{aligned}
|Z_{1,1}| &= |Z_{2,2}| \\
&\approx \left\{ c_1 + c_2 \cos\left(c_3 \frac{\Delta}{\lambda} + c_4 \right) e^{-c_5 \frac{\Delta}{\lambda}} |\varphi|^{c_6} \right\} \\
&\quad \left\{ \left(\frac{L}{\lambda} - c_7 \right)^2 + c_8 \right\}
\end{aligned} \tag{C.20}
$$

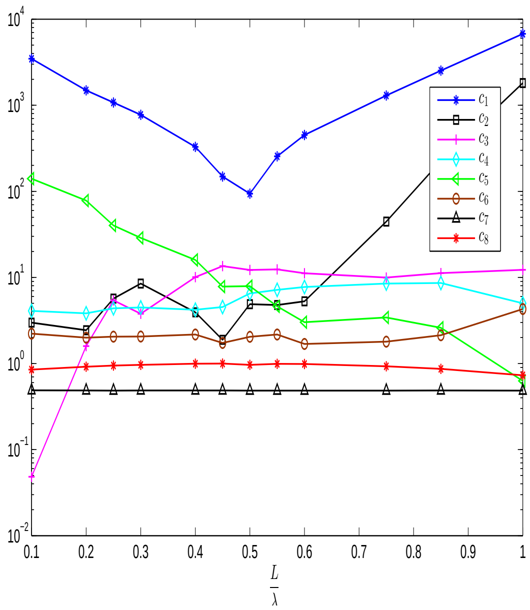

Figure C.4: How $\frac{L}{\lambda}$ affects the coefficients of the 8-DoF model in (C.20).

$$
\begin{aligned}
c_1 &\approx 2.324 \times 10^4 \left(\frac{L}{\lambda} \;-\; 0.4803\right)^2 \\
c_2 &\approx 0.001366\; e^{14.1\frac{L}{\lambda}} \;+\; 2.361 \\
c_3 &\approx \frac{2814\left(\frac{L}{\lambda}\right)^4 \;-\; 147.6\left(\frac{L}{\lambda}\right)^3 \;+\; 704.7\left(\frac{L}{\lambda}\right)^2 \;+\; 13.84\frac{L}{\lambda} \;+\; 190.6}{\left(\frac{L}{\lambda}\right)^4 \;-\; 924.6\left(\frac{L}{\lambda}\right)^3 \;+\; 2472\left(\frac{L}{\lambda}\right)^2 \;-\; 1600\frac{L}{\lambda} \;+\; 338.7} \\
c_4 &\approx \frac{-4.299\left(\frac{L}{\lambda}\right)^3 \;+\; 8.567\left(\frac{L}{\lambda}\right)^2 \;-\; 5.125\frac{L}{\lambda} \;+\; 0.9699}{\left(\frac{L}{\lambda}\right)^4 \;-\; 3.083\left(\frac{L}{\lambda}\right)^3 \;+\; 3.448\left(\frac{L}{\lambda}\right)^2 \;-\; 1.61\frac{L}{\lambda} \;+\; 0.2679} \\
c_5 &\approx 299.8\; e^{-7.444\frac{L}{\lambda}} \\
c_6 &\approx 2.1951 \\
c_7 &\approx 0.4853 \\
c_8 &\approx 0.9281
\end{aligned}
$$

C.21 Model 21

$$
\begin{aligned}
|Z_{1,1}| &= |Z_{2,2}| \\
&\approx c_0 + c_1 e^{\left(c_2 \frac{L}{\lambda}\right)} + c_3 e^{\left(-c_4 \frac{L}{\lambda}\right)}
\end{aligned} \tag{C.21}
$$

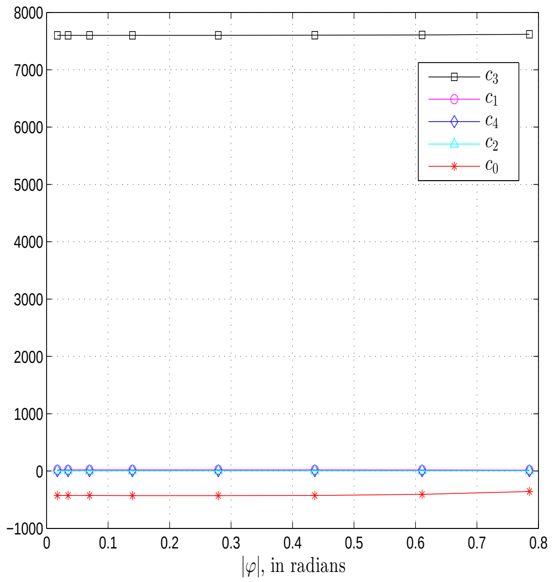

Figure C.5: How φ affects the coefficients of the 5-DoF model in (C.21).

From Fig. C.5,

$$
\begin{aligned}
c_0 &\approx -416.2750 \\
c_1 &\approx 19.20 \\
c_2 &\approx 5.9253 \\
c_3 &\approx 7604.9 \\
c_4 &\approx 6.8407
\end{aligned}
$$

C.22 Model 22

$$
\begin{aligned}
\log|Z_{1,1}| &= \log|Z_{2,2}| \\
&\approx p_{0,0} + p_{0,2}\ \log^2\left(\frac{L}{\lambda}\right) + p_{0,3}\ \log^3\left(\frac{L}{\lambda}\right) \\
&\quad + p_{0,4}\ \log^4\left(\frac{L}{\lambda}\right) + p_{0,5}\ \log^5\left(\frac{L}{\lambda}\right) \qquad \text{(C.22)}
\end{aligned}
$$

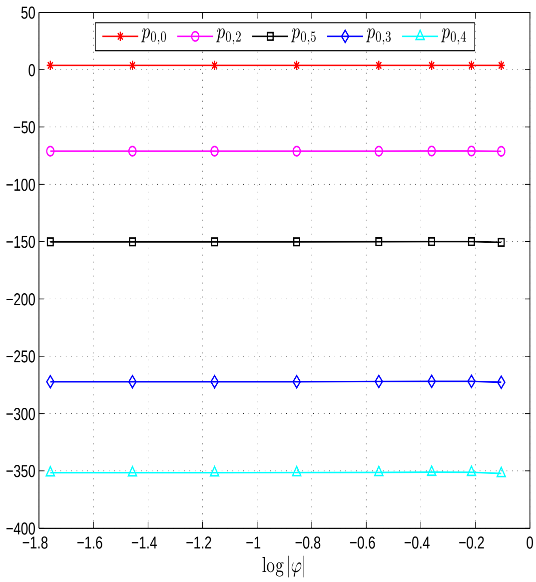

Figure C.6: How φ affects the coefficients of the 5-DoF model in (C.22).

From Fig. C.6,

$$
\begin{aligned}
p_{0,0} &\approx 3.7734 \\
p_{0,2} &\approx -71.0738 \\
p_{0,3} &\approx -272.20 \\
p_{0,4} &\approx -351.5250 \\
p_{0,5} &\approx -150.1875
\end{aligned}
$$

Appendix D

Candidate Models for $\angle Z_{1,1} = \angle Z_{2,2}$

D.1 Model 1

$$\begin{aligned}\angle Z_{1,1} &= \angle Z_{2,2} \\ &\approx \left\{q_1 + q_2 \cos\left(q_3 \frac{\Delta}{\lambda} + q_4\right) e^{\left(-q_5 \frac{\Delta}{\lambda}\right.}\right\} \left\{\cos\left(q_7 \frac{L}{\lambda} + q_8\right)\right\}\end{aligned} \tag{D.1}$$

where

$$\begin{aligned} q_1 &:= 1.7649 \\ q_2 &:= 6.6980 \\ q_3 &:= 0.0096 \\ q_4 &:= 4.7128 \\ q_5 &:= 9.3626 \\ q_6 &:= 6.5207 \\ q_7 &:= -4.7122 \end{aligned}$$

This model was not chosen due to the number of degrees-of-freedom of 7. The best fit model in (5.11) has only 5 degrees-of-freedom.

D.2 Model 2

$$\begin{aligned}
\angle Z_{1,1} &= \angle Z_{1,1} \\
&\approx \left\{ q_1 + q_2 \cos\left(q_3 \frac{\Delta}{\lambda} + q_4 \right) e^{\left(-q_5 \frac{\Delta}{\lambda}\right.} \right\} f(\frac{L}{\lambda})
\end{aligned} \tag{D.2}$$

where

$$f(\frac{L}{\lambda}) = \begin{cases} q_6, & \text{if} \quad \mod\left(\frac{L}{\lambda}, 1\right) < q_9 \\ \cos\left(q_7 \quad \mod\left(\frac{L}{\lambda}, 1\right) + q_8\right) & \text{if} \quad \mod\left(\frac{L}{\lambda}, 1\right) > q_9 \end{cases}$$

$$\begin{aligned}
q_1 &:= 1.4580 \\
q_2 &:= 2.2817 \\
q_3 &:= 5.8308 \\
q_4 &:= -1.6890 \\
q_5 &:= 25.4661 \\
q_6 &:= -0.8891 \\
q_7 &:= 5.5635 \\
q_8 &:= 8.6596 \\
q_9 &:= 0.4996
\end{aligned}$$

This model was not chosen due to the number of degrees-of-freedom of 9 and due to its complex form. The chosen model in (5.11) has only 5 degrees-of-freedom.

D.3 Model 3

$$\begin{aligned}\angle Z_{1,1} &= \angle Z_{2,2} \\ &\approx \left\{ q_1 + \overbrace{q_2 \sin\left(q_3 \frac{\Delta}{\lambda}\right) e^{-q_4 \frac{\Delta}{\lambda}}}^{Q\left(\frac{\Delta}{\lambda}\right) :=} |\sin(\varphi)| \right\} \\ &\quad \sin\left(q_5 \frac{L}{\lambda}\right), \end{aligned} \tag{D.3}$$

where

$$\begin{aligned} q_1 &:= 1.7648, \\ q_2 &:= 0.0971, \\ q_3 &:= 1.5977\pi, \\ q_4 &:= 10.5309, \\ q_5 &:= -2.0758\pi. \end{aligned}$$

This model was not chosen due to the little dependence of φ in the $\angle Z_{1,1}$ and $\angle Z_{2,2}$.

D.4 Model 4

$$
\begin{aligned}
\angle Z_{1,1} &= \angle Z_{2,2} \\
&\approx \left\{ q_1 + q_2 \sin\left(q_3 \frac{\Delta}{\lambda} \right) \ e^{-q_4 \frac{\Delta}{\lambda}} \ |\sin(\varphi)|^2 \right\} \\
&\quad \sin\left(q_5 \frac{L}{\lambda} \right),
\end{aligned}
\tag{D.4}
$$

where

$$
\begin{aligned}
q_1 &:= 1.7659, \\
q_2 &:= 0.0994, \\
q_3 &:= 1.6161\pi, \\
q_4 &:= 16.0681, \\
q_5 &:= -2.0758\pi.
\end{aligned}
$$

This model was not chosen due to the little dependence of φ in the $\angle Z_{1,1}$ and $\angle Z_{2,2}$.

D.5 Model 5

$$\begin{aligned}\angle Z_{1,1} &= \angle Z_{2,2} \\ &\approx \left\{ q_1 + q_2 \sin\left(q_3 \frac{\Delta}{\lambda} \right) \; e^{-q_4 \frac{\Delta}{\lambda}} \; |\sin(\varphi)|^{q_5} \right\} \\ &\quad \sin\left(q_6 \frac{L}{\lambda} \right), \end{aligned} \tag{D.5}$$

where

$$\begin{aligned} q_1 &:= 1.7664, \\ q_2 &:= 0.0098, \\ q_3 &:= 2.1483\pi, \\ q_4 &:= 6.8185, \\ q_5 &:= 3.1243, \\ q_6 &:= -2.0758\pi. \end{aligned}$$

This model was not chosen due to the little dependence of φ in the $\angle Z_{1,1}$ and $\angle Z_{2,2}$.

D.6 Model 6

$$
\begin{aligned}
\angle Z_{1,1} &= \angle Z_{2,2} \\
&\approx \left\{ q_1 + q_2 \sin\left(q_3 \frac{\Delta}{\lambda} \right) \; e^{-q_4 \frac{\Delta}{\lambda}} \; |\varphi| \right\} \\
&\quad \sin\left(q_5 \frac{L}{\lambda} \right),
\end{aligned} \tag{D.6}
$$

where

$$
\begin{aligned}
q_1 &:= 1.7649, \\
q_2 &:= 0.4952, \\
q_3 &:= 0.3245\pi, \\
q_4 &:= 12.7485, \\
q_5 &:= -2.0758\pi.
\end{aligned}
$$

This model was not chosen due to the little dependence of φ in the $\angle Z_{1,1}$ and $\angle Z_{2,2}$.

D.7 Model 7

$$
\begin{aligned}
\angle Z_{1,1} &= \angle Z_{2,2} \\
&\approx \left\{ q_1 + q_2 \sin\left(q_3 \frac{\Delta}{\lambda} \right) \; e^{-q_4 \frac{\Delta}{\lambda}} |\varphi|^{q_5} \right\} \\
&\quad \sin\left(q_6 \frac{L}{\lambda} \right), \qquad \text{(D.7)}
\end{aligned}
$$

where

$$
\begin{aligned}
q_1 &:= 1.7650, \\
q_2 &:= 0.0943, \\
q_3 &:= 1.1830\pi, \\
q_4 &:= 8.4140, \\
q_5 &:= 1.0945, \\
q_6 &:= -2.0758\pi.
\end{aligned}
$$

This model was not chosen due to the little dependence of φ in the $\angle Z_{1,1}$ and $\angle Z_{2,2}$.

D.8 Model 8

$$\begin{aligned}\angle Z_{1,1} &= \angle Z_{2,2} \\ &\approx \left\{q_1 + q_2 \cos\left(q_3 \frac{\Delta}{\lambda} + q_4\right)\ e^{-q_5 \frac{\Delta}{\lambda}}\right\} \\ &\quad \left\{\frac{q_6 \frac{L}{\lambda}^2 + q_7 \frac{L}{\lambda} + q_8}{\frac{L}{\lambda}^2 + q_9 \frac{L}{\lambda} + q_{10}}\right\},\end{aligned} \tag{D.8}$$

where

$$\begin{aligned} q_1 &:= 0.7811, \\ q_2 &:= 0.0007, \\ q_3 &:= 7.4286\pi, \\ q_4 &:= 8.5522, \\ q_5 &:= 0.7675, \\ q_6 &:= -0.9786, \\ q_7 &:= 1.5903, \\ q_8 &:= -0.5463, \\ q_9 &:= -1.0524, \\ q_{10} &:= 0.2992. \end{aligned}$$

The $\frac{\Delta}{\lambda}$ term inside the first curly bracket was first fitted in "cftool", a built-in function in MATLAB. The "rational" function involving $\frac{L}{\lambda}$ inside the second curly bracket was fitted separately in "cftool". After getting good fitting for both terms in "cftool", it was then fitted altogether in 4D using the code written in MATLAB. Aside from the complex nature of the above expression, this model was not chosen due to the large number of degrees-of-freedom.

D.9 Model 9

$$
\begin{aligned}
\angle Z_{1,1} &= \angle Z_{2,2} \\
&\approx \left\{ q_1 + q_2 \cos\left(q_3 \frac{\Delta}{\lambda} + q_4 \right) \; e^{-q_5 \frac{\Delta}{\lambda}} \right\} \\
&\quad \left\{ q_6 e^{-\left(\frac{\frac{L}{\lambda} - q_7}{q_8} \right)^2} + q_9 e^{-\left(\frac{\frac{L}{\lambda} - q_{10}}{q_{11}} \right)^2} \right\},
\end{aligned}
\tag{D.9}
$$

where

$$
\begin{aligned}
q_1 &:= 1.3726, \\
q_2 &:= 0.0039, \\
q_3 &:= 1.2443, \\
q_4 &:= 1.5995, \\
q_5 &:= 1.3905, \\
q_6 &:= 2.7508, \\
q_7 &:= 0.6657, \\
q_8 &:= 0.2374, \\
q_9 &:= -1.6424, \\
q_{10} &:= 0.4658, \\
q_{11} &:= 0.5343.
\end{aligned}
$$

Like the candidate model in (D.8), the same procedure was carried out. The term involving $\frac{L}{\lambda}$ is now a "Gaussian" function. Again, it's complex and difficult to explain in terms of electromagnetics. Also, this model was not chosen due to the large number of degrees-of-freedom.

D.10 Model 10

$$\begin{aligned}\angle Z_{1,1} &= \angle Z_{2,2} \\ &\approx \left\{ q_1 + q_2 \cos\left(q_3 \frac{\Delta}{\lambda} + q_4 \right) \; e^{-q_5 \frac{\Delta}{\lambda}} \right\} \\ &\quad \left\{ q_6 \left(\frac{L}{\lambda}\right)^5 + q_7 \left(\frac{L}{\lambda}\right)^4 + q_8 \left(\frac{L}{\lambda}\right)^3 + q_9 \left(\frac{L}{\lambda}\right)^2 + q_{10} \frac{L}{\lambda} + q_{11} \right\} \qquad (D.10)\end{aligned}$$

where

$$\begin{aligned} q_1 &:= 0.9909, \\ q_2 &:= 0.0039, \\ q_3 &:= 0.8370, \\ q_4 &:= 1.1806, \\ q_5 &:= 1.3791, \\ q_6 &:= 346.1105, \\ q_7 &:= -912.0844, \\ q_8 &:= 832.9370, \\ q_9 &:= -311.1516, \\ q_{10} &:= 47.7609, \\ q_{11} &:= -3.9708. \end{aligned}$$

Like the candidate model in (D.8), the same procedure was implemented. The term involving $\frac{L}{\lambda}$ is now a "polynomial" function. Again, it's complex and difficult to explain in terms of electromagnetics. Besides, this model was not chosen due to the large number of degrees-of-freedom.

D.11 Model 11

$$
\begin{aligned}
\angle Z_{1,1} &= \angle Z_{2,2} \\
&\approx \left\{ q_1 + q_2 \cos\left(q_3 \frac{\Delta}{\lambda} + q_4 \right) \; e^{-q_5 \frac{\Delta}{\lambda}} \right\} \\
&\quad \left\{ q_6 \sin\left(q_7 \frac{L}{\lambda} + q_8 \right) + q_9 \sin\left(c_{10} \frac{L}{\lambda} + q_{11} \right) \right\}, \qquad \text{(D.11)}
\end{aligned}
$$

where

$$
\begin{aligned}
q_1 &:= 1.5891, \\
q_2 &:= 0.9794, \\
q_3 &:= 0.0061, \\
q_4 &:= 1.5684, \\
q_5 &:= 1.3266, \\
q_6 &:= 1.1532, \\
q_7 &:= 6.6205, \\
q_8 &:= 3.0688, \\
q_9 &:= 0.2671, \\
q_{10} &:= 18.5921, \\
q_{11} &:= 3.2727.
\end{aligned}
$$

Like the candidate model in (D.8), the same procedure was employed. The term involving $\frac{L}{\lambda}$ is now a “sum of sine” function. The complexity of the expression and the large number of degrees-of-freedom were the reasons for not choosing this model.

D.12 Model 12

$$\begin{aligned} \angle Z_{1,1} &= \angle Z_{2,2} \\ &\approx \left\{ c_1 + c_2 \cos\left(c_3 \frac{\Delta}{\lambda} + c_4\right) e^{\left(-c_5 \frac{\Delta}{\lambda}\right)} \cos\left(c_7 \frac{L}{\lambda} + c_8\right) \right\} e^{(c_6 \varphi)} \end{aligned} \tag{D.12}$$

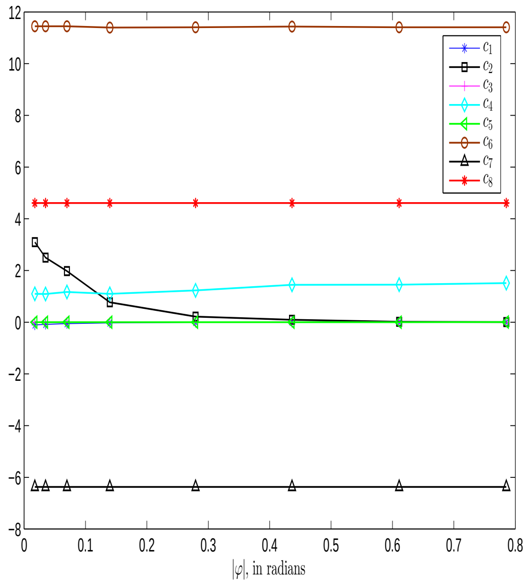

Figure D.1: How φ affects the coefficients of the 8-DoF model in (D.12).

From Fig. D.1,

$$\begin{aligned} c_1 &\approx -0.1282\ e^{-11.40|\varphi|} \\ c_2 &\approx 3.694\ e^{-10.21|\varphi|} \\ c_3 &\approx 5.9724 \times 10^{-6} \\ c_4 &\approx 1.2619 \\ c_5 &\approx 0.0010 \\ c_6 &\approx 11.4275 \\ c_7 &\approx -6.373 \\ c_8 &\approx 4.609 \end{aligned}$$

This model is not chosen because the fitting error is artificially low because of dominance by the VLab data at $\frac{L}{\lambda} \approx 1.0$.

D.13 Model 13

$$
\begin{aligned}
\angle Z_{1,1} &= \angle Z_{2,2} \\
&\approx \left\{ c_1 + c_2 \cos\left(c_3 \frac{\Delta}{\lambda} + c_4\right) e^{\left(-c_5 \frac{\Delta}{\lambda} + c_6 \varphi\right)} \right\} \\
&\quad \left\{ \cos\left(c_7 \frac{L}{\lambda} + c_8\right) \right\}
\end{aligned}
\tag{D.13}
$$

From Fig. D.2,

$$
\begin{aligned}
c_1 &\approx 5.082\ e^{-\left(\frac{\frac{L}{\lambda} - 0.4542}{0.04627}\right)^2}\ +\ 1.813 \\
c_2 &\approx 8.546 \times 10^{-9}\ e^{16.63 \frac{L}{\lambda}} \\
c_3 &\approx 1258\ e^{-18.64 \frac{L}{\lambda}}\ +\ 9.929 \\
c_4 &\approx 4.8472 \\
c_5 &\approx \frac{-0.06303\ \frac{L}{\lambda}\ +\ 0.7038}{(\frac{L}{\lambda})^2\ -\ 0.4114\ \frac{L}{\lambda}\ +\ 0.06139} \\
c_6 &\approx 3.6788 \\
c_7 &\approx -6.3728 \\
c_8 &\approx 4.6093
\end{aligned}
$$

The functions c_1, c_2, c_3 and c_5 are derived from the 2D curve fitting in Matlab's "cftool". While the values of c_4, c_6, c_7 and c_8 are their averages for all $\frac{L}{\lambda}$'s.

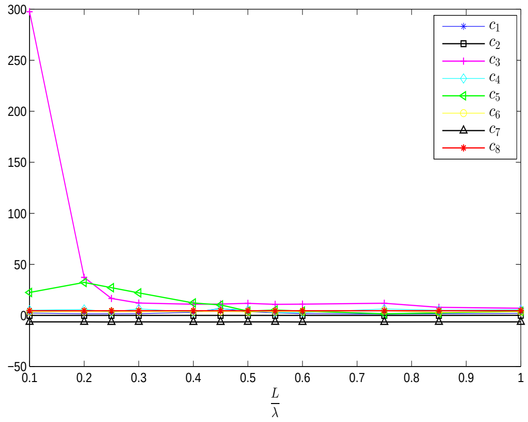

Figure D.2: How $\frac{L}{\lambda}$ affects the coefficients of the 8-DoF model in (D.13).

D.14 Model 14

$$
\begin{aligned}
\angle Z_{1,1} &= \angle Z_{2,2} \\
&\approx \left\{c_1 + c_2 \cos\left(c_3 \frac{\Delta}{\lambda} + c_4\right) e^{\left(-c_5 \frac{\Delta}{\lambda}\right)} |\varphi|^{c_6}\right\} \\
&\quad \left\{\cos\left(c_7 \frac{L}{\lambda} + c_8\right)\right\}
\end{aligned}
\tag{D.14}
$$

From Fig. D.3,

$$
\begin{aligned}
c_1 &\approx 5.061\ e^{-\left(\frac{\frac{L}{\lambda} - 0.4542}{0.04625}\right)^2} + 1.816 \\
c_2 &\approx 4.322 \times 10^{-10}\ e^{22.78 \frac{L}{\lambda}} \\
c_3 &\approx 2813\ e^{-22.97 \frac{L}{\lambda}} + 10.16 \\
c_4 &\approx 4.8490 \\
c_5 &\approx \frac{-0.3016\ \frac{L}{\lambda} + 0.7147}{(\frac{L}{\lambda})^2 - 0.4675\ \frac{L}{\lambda} + 0.07276} \\
c_6 &\approx 1.9116 \\
c_7 &\approx -6.3727 \\
c_8 &\approx 4.6093
\end{aligned}
$$

The functions c_1, c_2, c_3 and c_5 are derived from the 2D curve fitting in Matlab's "cftool". While the values of c_4, c_6, c_7 and c_8 are their averages for all $\frac{L}{\lambda}$'s.

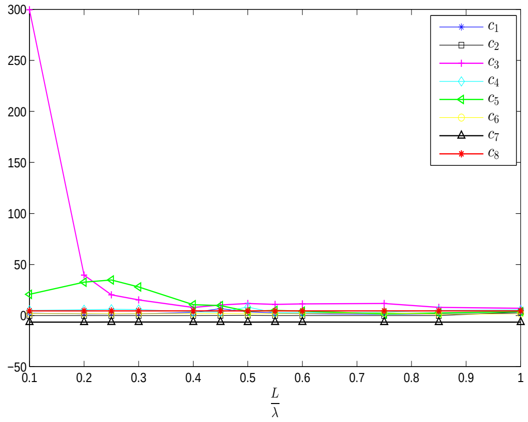

Figure D.3: How $\frac{L}{\lambda}$ affects the coefficients of the 8-DoF model in (D.14).

D.15 Model 15

$$
\begin{aligned}
\angle Z_{1,1} &= \angle Z_{2,2} \\
&\approx \left\{ c_1 + c_2 \cos\left(c_3 \frac{\Delta}{\lambda} + c_4 \right) e^{\left(-c_5 \frac{\Delta}{\lambda} + c_6 \varphi\right)} \right\} \\
&\quad \left(e^{-\left(\frac{\frac{L}{\lambda} - c_7}{c_8}\right)^2} + c_9 \right)
\end{aligned} \tag{D.15}
$$

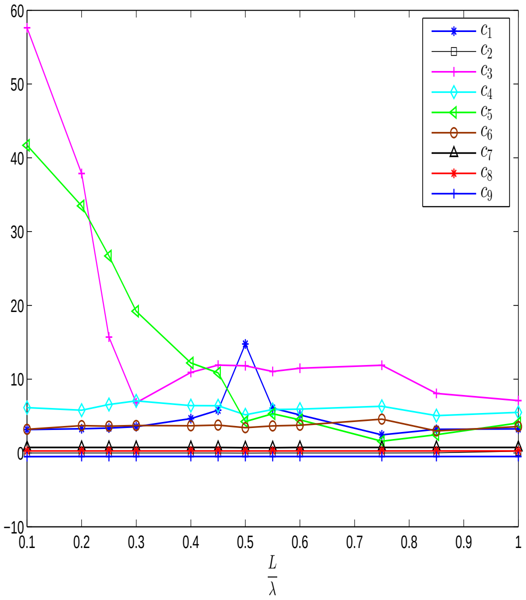

Figure D.4: How $\frac{L}{\lambda}$ affects the coefficients of the 9-DoF model in (D.15).

From Fig. D.4,

$$
\begin{aligned}
c_1 &\approx 11.21\ e^{-\left(\frac{\frac{L}{\lambda}-0.5009}{0.04042}\right)^2} + 3.553 \\
c_2 &\approx 8.785 \times 10^{-9}\ e^{17.07\frac{L}{\lambda}} - 0.004687 \\
c_3 &\approx 135.2\ e^{-9.939\frac{L}{\lambda}} + 9.125 \\
c_4 &\approx 6.0231 \\
c_5 &\approx 67.65\ e^{-4.165\frac{L}{\lambda}} \\
c_6 &\approx 3.6412 \\
c_7 &\approx 0.7354 \\
c_8 &\approx 0.2600 \\
c_9 &\approx -0.4908
\end{aligned}
$$